Faculdade de Engenharia da Universidade do Porto

A Bottom-Up Approach to Model Tumor-Vascular Interactions

Inês Oliveira Pereira Coutinho

Master in Bioengineering

Major Molecular Bioengineering

Supervisor: Sílvia Bidarra (Junior Researcher @ i3S)

Co-supervisor: Cristina Barrias (Group Leader @ i3S)

29 de junho de 2022

“A vida tem me ensinado que nenhuma coisa é simples, que só às vezes o parece, e que é justamente quando mais o parecer que mais nos convirá duvidar.”

- José Saramago

This page was intentionally left in blank.

Acknowledgements

Já dizia José Saramago que a vida nos vai ensinando que nada é simples. Agora que chego ao fim destes 5 anos, não podia concordar mais. Foi indubitavelmente uma viagem cheia de curvas e contracurvas, mas também cheia de momentos onde é preciso parar o carro para interiorizar a beleza da paisagem. Estes anos ajudaram-me a perceber que irão sempre haver obstáculos que parecem impossíveis de ultrapassar, mas que são justamente esses obstáculos que no fundo me surpreendem com a capacidade de adaptação e perseverança que me esqueço existirem em mim. É muito gratificante perceber que todo o esforço que coloquei ao longo dos anos compensou tremendamente, tornando-me numa pessoa da qual tenho imenso orgulho. E é claro que sendo uma viagem tão longa, não a fiz sozinha. Trouxe sempre comigo as pessoas que são indispensáveis no meu dia-a-dia, e também me fui cruzando com pessoas novas que enriqueceram toda esta experiência.

Quero em primeiro lugar agradecer à minha orientadora, Sílvia Bidarra, pela sua motivação e incrível dedicação a este projeto. Pela sua prontidão e disponibilidade para ajudar a qualquer hora do dia, porque mesmo estando fora do laboratório, a sua ajuda estava sempre à curta distância de uma mensagem no WhatsApp. Por todas as horas que dedicou a ajudar-me no confocal e por partilhar comigo uma imaginação fértil que nunca falhou em transformar os esferóides em fantásticas personagens de animação. Agradeço ainda, por todo o carinho e apoio que sempre demonstrou e que tanto me ajudaram a ultrapassar as fases mais atribuladas. Quero também agradecer à minha co-orientadora, Cristina Barrias, pela oportunidade de fazer parte do BeMic e por, talvez, mesmo sem saber, me fazer chorar a rir pela sua maneira divertida de levar a vida. É um exemplo de como boa disposição e companheirismo contribuem para um ambiente de trabalho mais produtivo. Por fim, agradeço a todo o grupo BeMic por me ter acolhido de braços abertos e pela disponibilidade em esclarecer qualquer questão que fosse surgindo. Obrigada ainda pela companhia nos almoços e pelos belíssimos passeios no parque. São sem dúvida um grupo de pessoas inspiradoras pela paixão que demonstram pelo seu trabalho.

Agora, um enorme obrigada a todos os meus amigos, que me acompanham há anos e sempre aturaram as minhas ânsias e suspiros. Obrigada pela vossa presença

constante, pelas conversas mais profundas, mas também pelas paródias sem sentido. Obrigada por saberem dançar comigo nos concertos e ainda tirar boas sonecas na praia. São um grupo de pessoas lindas, com corações de ouro que certamente levarei comigo até ao fim da vida.

Por fim, tenho de agradecer do fundo do meu coração à minha família, a razão da minha existência. Sem vocês eu nunca conseguiria dar o próximo passo, sair da minha zona de conforto e conquistar os sonhos que tenho desde pequenina. Pai, mãe e mana Sofia, obrigada pelo vosso apoio incondicional. Por me ouvirem mesmo quando não dizia nada de jeito e pela paciência em repetir as palavras que tanto precisava de ouvir, mas que pareciam não entrar. Obrigada por me inspirarem diariamente com a vossa confiança e com a quantidade infinita de amor que sempre têm para dar. Vocês são a minha rocha e a razão de todo o meu sucesso, e por tudo isto, eu estou eternamente grata.

The research described in this thesis was financially supported by:

Portuguese Foundation for Science for EndoSWITCH project (PTDC/BTM-ORG/5154/2020) and research contracts DL 57/2016/CP1360/CT0006 and IF/00296/2015.

Abstract

Despite recent scientific advances, cancer is still a major health related problem worldwide. Amongst the different types, Breast Cancer is one of the most common, and is currently the primary cause of cancer-related deaths in women. Moreover, it is not the primary tumor that is usually the culprit. It is the "untreatable" nature of metastatic breast cancer that is responsible for the majority of deaths related to breast cancer. A key step in tumor progression and metastasis is angiogenesis. The development of vasculature within the breast tumor microenvironment is crucial not only for nutrient attainment, but also for disposing of metabolic waste and carbon dioxide to maintain homeostasis and the erratic proliferation of cells. Overwhelming efforts have been put into designing innovative pre-clinical models that can truthfully replicate the disease *in vitro*. 3D models that can incorporate multiple types of cells and also replicate the vascular compartment, will certainly help to further comprehend the complexity behind tumor vascularization and metastasis. In that sense, this project's main goal was to develop a vascularized 3D *in vitro* platform, that could serve as a research tool to further study the role of angiogenesis in breast cancer. To reach that goal, the thesis was divided in two main branches: the development of tumoroids, coculture spheroids that replicate the breast tumor itself, and the development of vascular units (VUs), that represent the surrounding vascular stroma. Both branches would then converge by incorporating them in a well-defined alginate matrix with tunable biochemical and mechanical properties and integrating them in a single microfluidic device that allows the evaluation of heterotypic cell interactions and the angiogenic potential of the whole system.

To develop tumoroids, MCF-7 cells from breast tumor were combined with fibroblasts (cancer associated - CAF or normal mammary fibroblasts - nFib) in non-adherent agarose molds to generate coculture spheroids, further designated tumoroids. It was verified that by adding the fibroblasts 6 days after the formation of MCF-7 monoculture spheroids (sequential seeding), fibroblasts that aggregated in the spheroid's core, could take up a bigger area of the spheroid without being overgrown by the epithelial cells. This seeding method was able to more truthfully replicate the cellular organization found in *in*

vivo tumors. These tumoroids were subsequently embedded in an ECM-like alginate matrix. This alginate was previously functionalized with RGD and a bifunctional MMP-sensitive peptide (CGPQG↓IWGQC) that was simultaneously the crosslinking agent. Some embedded tumoroids were able to invade the bioresponsive alginate matrix.

For the generation of the VUs, coculture spheroids of outgrowth endothelial cells (OEC) and fibroblasts (CAF/nFib) were also produced using the agarose molds. These spheroids exhibited the formation of vascular-like structures within the spheroid. Furthermore, when embedded in our multi-functional alginate matrix, these structures were able to sprout radially and establish extensive networks in both matrices. It was even observed that these endothelial networks were lumenized, indicating the possibility of shaping into vessels, which were promising results towards achieving a truly vascularized model.

Preliminary work was developed regarding the fabrication of the microfluidic device. The platform contained three parallel channels, connected through microchannels that, in the future, will be filled with spheroids embedded in a bioresponsive alginate hydrogel. The central channel will have the tumor compartment (tumoroids previously optimized) and the two side channels will have the vascular/stromal compartment (VUs embedded in alginate at day 1). Optimization of the device was performed in order to improve resolution that would then enable the injection of the alginate hydrogel.

Altogether, these results reveal that the suggested 3D in vitro platform is a versatile and powerful tool to study the role of angiogenesis during tumor progression. In the future, it can be further optimized to receive patient-derived cells for applications such as drug screening, which paves the way to bringing us closer to a world where personalized medicine is the standard of care.

Table of Contents

List Of Figures

List Of Tables

List of Abbreviations

2D	Two-dimensional
3D	Three-dimensional
α-SMA	Alpha Smooth Muscle Actin
β-cat	Beta-Catenin
BRCA1/2	Breast cancer genes 1/2
CAF	Cancer-Associated Fibroblast
CAM	Cell Adhesion Molecule
CE	Contrast-enhanced
CK5/6	Cytokeratin 5/6
CLSM	Confocal Laser Scanning Microscopy
cPARP	cleaved Poly-ADP-ribose polymerase
CTC	Circulating Tumor Cell
DCIS	Ductal Carcinoma *in situ*
DMTMM	4-(4,6-Dimethoxy1,3,5-triazin-2-yl)-4-methylmorpholinium chloride
EC	Endothelial cell
E-cad	E-cadherin
ECM	Extracellular Matrix
EGF	Epidermal Growth Factor
EGFR	Epidermal Growth Factor Receptor
EMT	Epithelial-Mesenchymal Transition
EPC	Endothelial Progenitor Cell

ER	Estrogen receptor
FAP	Fibroblast Activation Protein
FN	Fibronectin
FSP-1	Fibroblast-Specific Protein 1
HER2	Human Epidermal Growth Factor Receptor 2
hLF	Human Lung Fibroblast
hMF	Human Mammary Fibroblasts
HR	Hormone receptor
HUVEC	Human Umbilical Vein Endothelial Cell
IDC	Infiltrating Ductal Carcinoma
IF	Intermediate Filaments
ILC	Infiltrating Lobular Carcinoma
IPN	Interpenetrating Networks
MaSC	Mammary Stem Cell
MBC	Metastatic Breast Cancer
MCF-7	Michigan Cancer Foundation-7
MCTS	Multicellular Tumor Spheroid
MI	Microwave Imaging
MMP	Metalloproteinases
MRI	Magnetic Resonance Imaging
MSC	Mesenchymal Stem Cell
MT1-MMP	Membrane-Type 1 Matrix Metalloproteinase
nFib	Normal Human Mammary Fibroblasts
NHLF	Normal Human Lung Fibroblasts
ON	Overnight

LCIS	Lobular Carcinoma *in situ*
PDGFR-α	Platelet-Derived Growth Factor-α Receptor
PDGF-β	Platelet Derived Growth Factor-β
PDMS	Polydimethylsiloxane
PEG	Polyethylene glycol
PET	Positron Emission Tomography
PHEMA	Poly(hydroxyethyl methacrylate)
PNIPAM	Poly(N-isopropylacrylamide)
PLA	Polylactic Acid
PR	Progesterone receptor
RT	Room temperature
shRNA	Short hairpin RNA
TME	Tumor Microenvironment
TN	Triple Negative
TP53	Tumor protein 53
TSP	Trimethylsilylpropanoic acid
VEGF	Vascular Endothelial Growth Factor
Vim	Vimentin

Chapter 1 - Introduction

1.1 The Mammary Gland – How does it Work?

1.1.1 Anatomy and Functions

Breasts are present both in male and female anatomy. Understanding their anatomy is a key step to study the disorders that affect them and to be able to develop strategies to better treat breast cancer patients.

Regarding the topographic anatomy, the breast base extends from the 2nd to the 6th rib. The sternum is located medially and the midaxillary line laterally [1]. Muscles lie underneath each breast, covering the ribs. Pectoralis major is present underneath the upper two-thirds of the breast and serratus anterior underlies the lower two-thirds [2]. Other muscle that lies partially underneath the breasts is the external oblique muscle of the abdomen.

Breast tissue is encased by superficial fascia that is present below the dermis, however, a part of it, designated the axillary tail (of Spence) penetrates the deep fascia and sits in the axilla. Breasts are majorly composed of adipose tissue and glandular tissue with ratio varying among individuals. However, after puberty, glandular tissue is more prominent in females than in males in response to estrogen release, hence the mammary gland is usually rudimentary or non-functional in males.

Structurally, the mammary gland has three components: the skin, the parenchyma and the stroma (Figure 1).

Regarding the skin component, it is constituted by the nipple and the areola. The nipple is an important part of breastfeeding and is commonly located at the level of the 4th rib, aligned with the midclavicular line [1]. The areola is a circular pigmented area that circles the nipple. It contains melanocytes and usually, pigmentation reaches its peak after puberty. This area has numerous sebaceous glands (termed tubercles of tubercles of Morgagni, that represent the opening of the Montgomery glands) and the oil they secrete helps lubricate during breastfeeding and keeps germs away from the breasts [3].

The **parenchyma** is composed by glandular tissue that is divided into 15-20 lobes [2], [4]. Lobes are arranged in circular fashion and are composed of smaller structures designated lobules that contain alveoli and form the basic functional unit of the mammary gland. These alveoli are all connected through small ducts that meet to form a bigger duct for each lobe that finally connects to the nipple [5]. Histologically, the epithelial tissue presents an internal layer that connects to the ductal lumen and contains cubic pseudo-striated epithelial cells. Some of these cells namely the ones in the terminal end of the duct have the potential to differentiate into lactocytes, the cells that secrete milk during lactation. In addition, an outer layer is constituted by myoepithelial cells that have similar characteristics to smooth muscle cells. They have the ability to contract, surrounding the luminal layer tightly. This second layer lies basally in the basement membrane [6].

The **stroma** compartment offers support to the breast and is located both in between the lobes (inter-lobular stroma) and surrounding the lobules (intra-lobular stroma). The inter-lobular stroma contains densely arranged fibrous connective tissue (mainly composed of collagen-type IV and laminin) embedding adipose tissue. This part of the stroma is progressively replaced by adipose tissue during menopause which often causes the breasts to increase in volume [7]. Relevant components of the connective tissue are the suspensory ligaments of Cooper responsible for suspending the breasts from the pectoral fascia in the correct position [8]. Encircling the lobules, the intra-lobular stroma contains fibroblasts, some immune cells, such as macrophages and lymphocytes, and blood vessels. This part of the stroma lacks elastic fibers and is greatly responsive to hormonal micro-environmental cues. It is associated with different stages of mammary gland development through cross-talking with the epithelium.

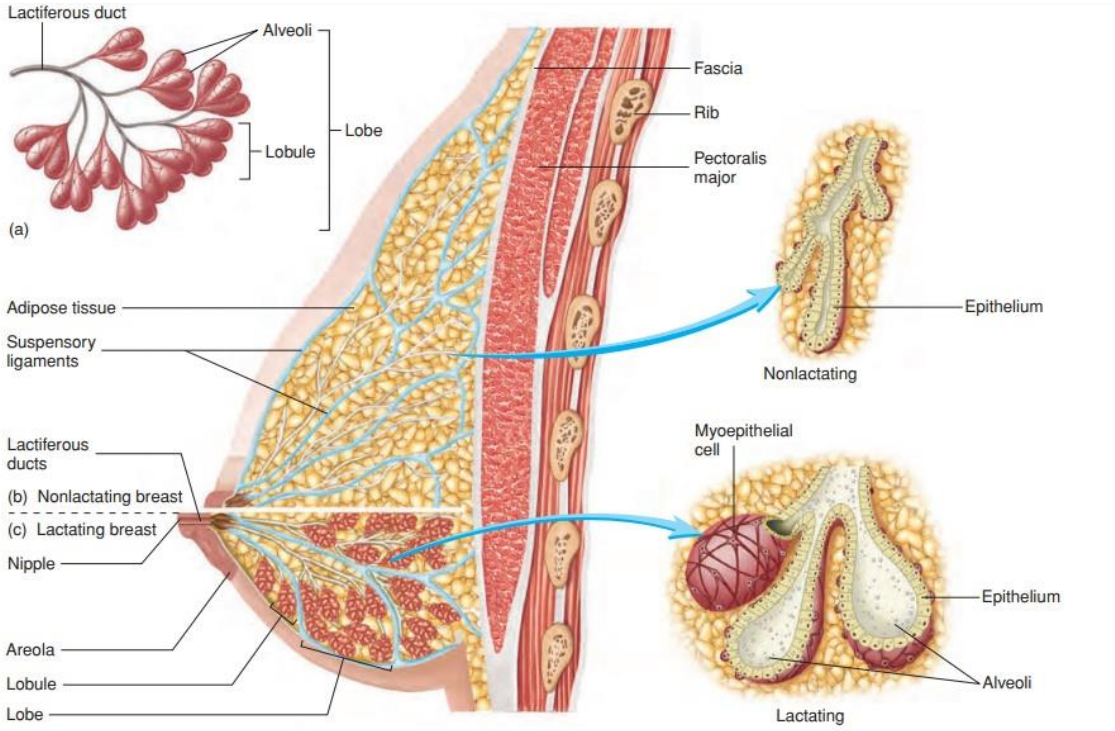

Figure 1 | The structure of the breast. (a) Each lactiferous duct connects to one or more alveoli at the end. A group of alveoli forms a lobule and several lobules form a lobe. b) The nonlactating breast with a duct system that is not extensively developed. c) The lactating breast has a more complex duct system with multiple branches that end in well-developed alveoli. Adipose tissue is abundant in both nonlactating and lactating breast. Adapted from [4].

The primary function of the mammary gland is to produce milk for the nurturement of a neonatal. This function is regulated by different hormones. During pregnancy, estrogen and progesterone enhance the development of the duct system, while prolactin stimulates the production of milk within the glandular tissue. Oxytocin is released when an infant suckles on the breast, stimulating the contraction of the myoepithelial cells in the lobules and ducts which in turn causes the ejection of milk from the glands [8]. Numerous evidence have shown that human milk is a powerful source of bioactive components and nutrients that contribute to the infant's healthy development and growth. Moreover, human milk stem cells have been discovered, and they may play an important role in the establishment of the innate immune system [9].

1.1.2 Blood Supply and Lymphatics

The mammary gland is a highly vascularized organ. Arterial blood is supplied to the skin of the breasts by a network of vessels deriving from the internal mammary artery (principal supply), axillary artery and branches of the posterior intercostal artery (Figure 2A). These vessels and capillaries provide biochemical factors which are vital for the good functioning of the gland and, later on, for the production of milk. However, studies indicate that the amount of blood supplied by each artery varies among individuals, and their organization does not follow the ductal system, so the arterial network is often asymmetric between breasts [6], [10].

Lymphatic vessels are of particular interest, specifically due to the ability of tumors to spread through the lymphatic drainage. Lymph fluid is filtered and carried from the breast lobules through intramammary nodes into a subareolar plexus, named Sappey's plexus [11] (Figure 2B). From there, lymphatic drainage happens mainly into the axillary lymph nodes (that correspond to the dominant pathway receiving more than 75% of the lymph) and the internal mammary (parasternal) nodes (that drains the remaining 25%) [12]. For that reason, these are the main locations for metastasis. Often axillary lymph nodes are surgically removed to treat breast cancer, since they help in cancer staging [13]. Axillary lymph nodes are classically divided into five groups: anterior (pectoral) group that drains the outer quadrants of the breast; posterior (subscapular) group that drains the lower outer quadrant; lateral group located under the axilla that drains only a residual quantity of lymph from the breast; central group that receives lymph from the anterior, posterior, and lateral groups; and the apical group that is located more deeply in the axilla's apex and receives lymph from all the previous groups, as well as drains the upper inner quadrant of the breast .

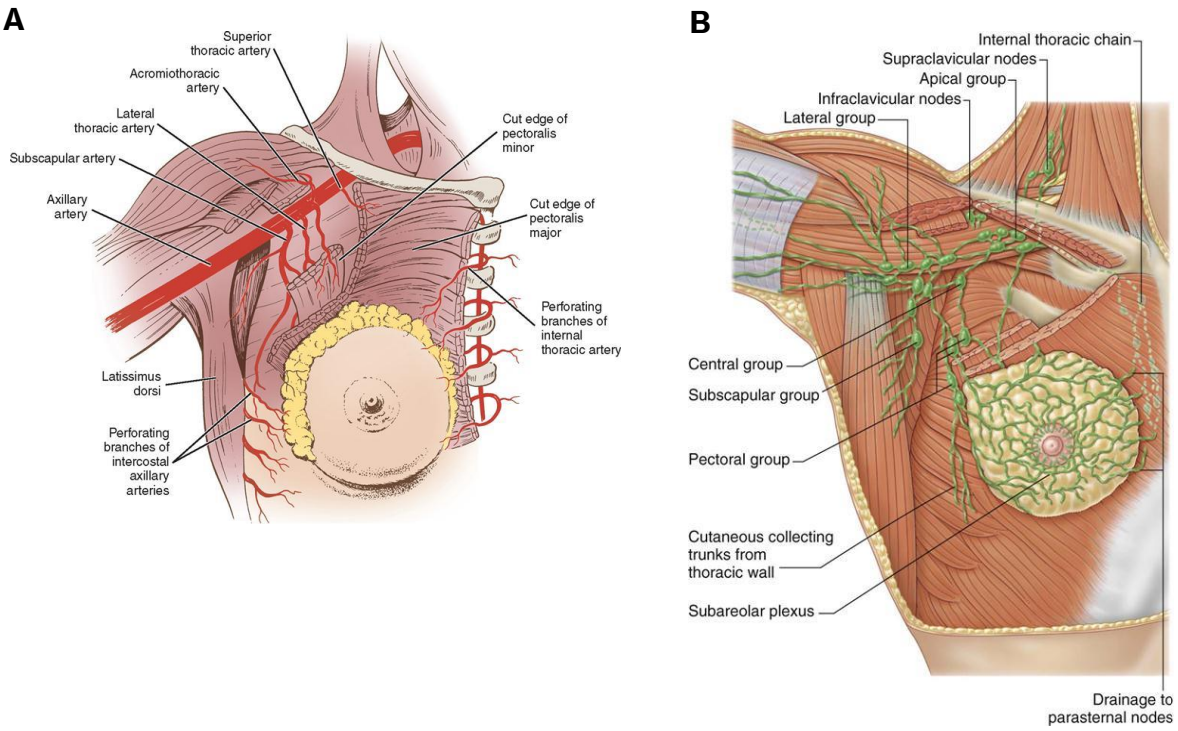

Figure 2 | Blood supply and lymphatics of the breast. A) Normal arterial blood supply of the breast. B) Lymphatic drainage of the breast. Adapted from [10].

1.2 Breast Cancer – A Worldwide Burden

1.2.1 Social Impact and Characterization

Despite recent advances in the development of new pharmaceuticals and surgical interventions, cancer is still a major health related problem worldwide and is currently one of the leading causes of death globally [14]. In the United States, cancer was responsible for more than 600 000 deaths in 2021, representing the second leading cause of death in this country [15]. Amongst the different types, breast cancer is one of the most common, with a total of 2 261 419 new cases reported in 2020 and is currently the primary cause of cancer-related deaths in women (Figure 3) [14].

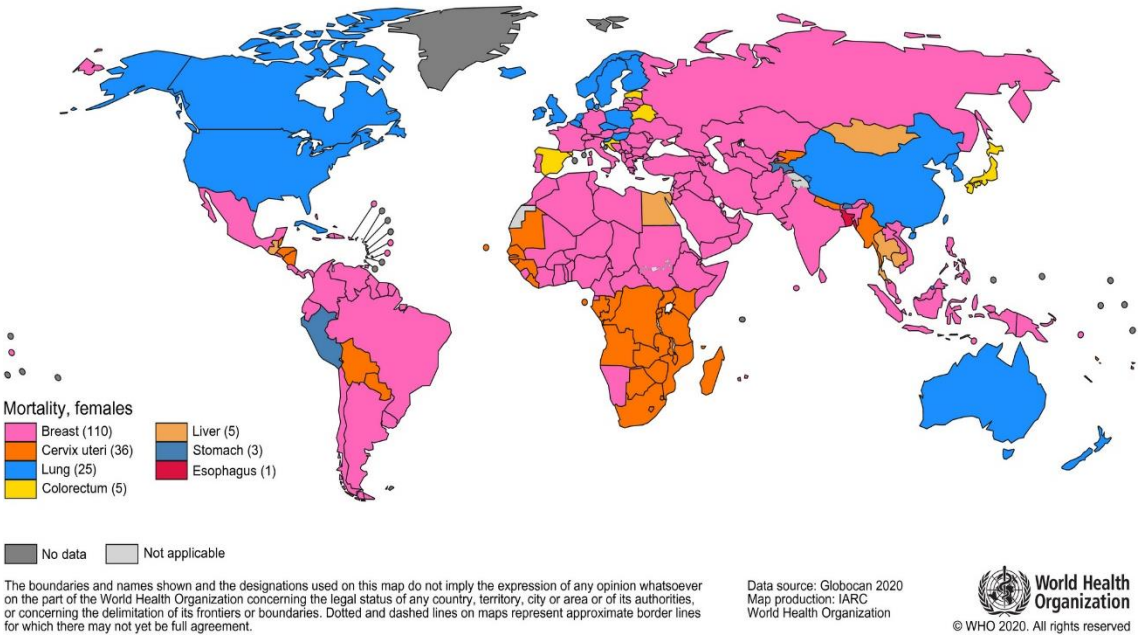

Figure 3 | Most common type of cancer mortality by country in 2020 among women. The numbers of countries represented in each ranking group are included in the legend. Source: GLOBOCAN 2020.

Regarding site, breast cancer can be classified as non-invasive or invasive breast cancer. Non-invasive breast cancer corresponds to tumors which cells manage to stay confined to the ducts and do not invade the neighboring adipose and connective tissue. It comprises Ductal Carcinoma *in situ* (DCIS) (the most frequent form of non-invasive breast cancer) and Lobular Carcinoma *in situ* (LCIS). Invasive breast cancer is characterized by abnormal cells that are capable of escaping from the ducts and invading the surrounding tissues. Some examples of this type of cancer are Infiltrating Lobular Carcinoma (ILC), Infiltrating Ductal Carcinoma (IDC) and Medullary Carcinoma [16], [17].

Additionally, it can be classified into five subtypes according to molecular features based on the assessment of gene expression profiles. Examples of biological markers are hormone receptors (HRs) such as estrogen receptor (ER), progesterone receptor (PR), and human epidermal growth factor receptor 2 (HER2); and others such as Ki67 (marker of cell proliferation), cytokeratin 5/6 (CK5/6), and epidermal growth factor receptor (EGFR). Based on these markers, the breast cancer subtypes are **luminal A** (ER

positive; PR positive/negative; HER2 negative; Ki67 low), **luminal B** (ER positive; PR positive/negative; HER2 positive/negative; Ki67 high), **HER2-enriched** (ER and PR negative and HER2 positive), **basal-like** (ER negative; PR negative; HER2 negative; and EGFR positive or CK5/6 positive), and **triple-negative** phenotype (TN) (ER negative; PR negative; HER2 negative) [18]. The analysis of these genetic profiles helps create a correlation with the patient's prognosis and survival [19]. For example, a study conducted by Sørlie has concluded that luminal A patients had a lower probability of recurrence. On the other hand, basal and HER2+ subtypes presented a shorter period before the appearance of metastasis [20]. These studies help conclude that different subtypes present distinct responses to treatment, which means that identification of these molecular markers is determinant in the efficacy of the applied treatment [21]. However, another aspect to consider is that intratumor heterogeneity is common in breast cancer. This means that subtype identification of one biopsy, does not necessarily represent the entirety of the tumor and so patients with the same subtype may respond differently to the same treatment. Cell populations that are phenotypically different within a tumor lead to a more aggressive cancer and make finding the suitable treatment for the patient a much challenging task [22].

Early-stage detection of breast cancer can have a significant impact on the patient's survival. Diagnosis is usually achieved through screening or symptoms of pain that lead to a more detailed diagnostic exam. Screening provides women a higher chance of detecting smaller tumors, and a lower risk of developing metastasis. This means that they are less likely to require chemotherapy or invasive removal surgeries, contributing to reduced morbidity. Mammography is the universally recommended approach and is the only screening practice that has proven to reduce breast cancer mortality. This technique uses X-ray imaging, and it is sensitive (77%–95%) and specific (94%–97%). However, for women aged under 50 years old, mammography is less sensitive (58%–85%), as well as for smaller tumors (with a diameter of less than 1 mm) [23]. This lower sensitivity is explained by the that fact that younger women (premenopausal years) have a denser breast tissue, which decreases the radiologist's ability to correctly identify the presence of a lesion. Other screening approaches include contrast-enhanced (CE) digital mammography, ultrasound, magnetic resonance imaging (MRI), positron emission tomography (PET) or more recently, microwave imaging (MI) [24].

Upon screening approaches, women that test positive will be advised to undergo a tissue biopsy. It is often a challenge for the pathologist to distinguish between similar diseases, as is the case for *in situ* disease *versus* microinvasion, or ductal cancer *versus* lobular cancer. For that matter, the support of immunohistochemical and molecular tests, will in most cases, help identify if it is either benign or cancerous tissue [25].

Typically, biomarkers are used to distinguish different types of breast cancer and help establish a line of treatment that most suitably fits the patient. Biomarkers initially evaluated are the expression levels of Ki67 and hormone receptors (ER, PR and HER2). However, various other underrepresented biomarkers have proven to be promising tools for prognostic and diagnosis. Four biomarkers are FDA-approved to assess breast cancer using liquid biopsies: two cancer antigens (CA 15-3, and CA 27-29), HER2, and circulating tumor cell (CTC) [26]. Detection and isolation of CTCs is currently performed using the CellSearch® system and represents a predictive biomarker for the risk of relapse or death. Nevertheless, this technique is in its infant stages and still raises some concerns in the scientific community [27].

1.2.2 Mutations and the Risk for Breast Cancer

Breast cancer genes-1/2 (BRCA1/BRCA2) are other known genes implicated in the risk of breast cancer. *BRCA1* gene is located in chr17q and the translated BRCA1 protein is responsible for regulating transcription, proliferation and DNA repair mechanisms. Meanwhile, *BRCA2* is located in chr13q and BRCA2 protein is mainly in charge of controlling DNA repair [28]. Essentially, these two genes produce proteins that suppress cell growth and so they are designated tumor suppressing genes. A commonly observed event is the loss of heterozygosity (LOH), that happens when a person that already possesses one of the alleles mutated/deleted and suffers a mutation in the healthy allele. This leads to unrepaired DNA damage and eventually cancer. Mutations in these genes are frequently observed in hereditary breast cancer (90% of cases) and are also present in the majority of hereditary ovarian cancer [28].

Tumor protein 53 (TP53) is encoded by the *p53* gene which is a commonly mutated gene in many types of cancers. Although TP53 mutations are rare when

compared to BRCA1/2, it still determines a high risk for breast cancer, especially relevant when mutations in the BRCA genes are not causative [29].

Besides biomarkers, other established prognostic markers applied in the clinic are the tumor size (tumors with diameters bigger than 2 cm are more prone to metastasize, hence present a poor prognostic), axillary lymph-node metastasis, and the histological grade [30].

1.2.3 The Metastatic Process

Breast cancer mortality is extremely high, making this an unquestionably daunting disease. However, it is not the primary tumor that is usually the culprit. It is the "untreatable" nature of metastatic breast cancer that is responsible for the majority of deaths related to breast cancer.

Breast cancer has a great metastatic potential specifically towards tissues like lung, bone, liver, and brain. Moreover, it is frequent that patients end up developing metastasis at multiple sites. It is estimated that between 20% to 50% of patients diagnosed with primary breast cancer, will, sooner or later, develop metastatic disease, clinically classified as stage IV metastatic breast cancer (MBC) [31].

The spreading of a tumor is a complex process with various sequential steps (Figure 4). These include invasion of the surrounding tissues, intravasation, migration through the lymphatics or blood vessels, extravasation and colonization of a distant organ. It starts with the acquisition of an aggressive mesenchymal-like phenotype by a group of cells present in the primary tumor. These cells begin to invade the surrounding tissue by decreasing intercellular adhesions and their connection to the ECM [32]. Relevant molecular modifications in this stage include loss of expression of E-cadherin (responsible for cell-cell adhesion) and increase in the expression of N-cadherin [33]. This alteration relates to the epithelial-mesenchymal transition (EMT) that has shown to be determinant in the development of metastasis. Besides depletion of cell-cell adhesion, tumor cells experiencing EMT will start degrading the ECM using proteolytic enzymes named metalloproteinases (MMPs). These proteins act by degrading molecules responsible for

cell-matrix adhesion, such as integrins, which in turn will promote tumor growth and further invasion. Upon this phenotype shift, cancer cells lose their apical-basal polarity, acquiring a front-rear polarity, which implies additional changes in their cytoskeleton [33]. Motility is assured by the myosin/actin engine together with ROCK signaling pathway, and similarly to unicellular organisms, these cells can modulate their shape, stretching and compressing as a way to migrate across the matrix's pores.

Later on, these cells are able to adhere to the endothelium and migrate through it, hence entering the vasculature where they will be disseminated through the bloodstream until they reach other organs. This step can also occur through the lymphatic vessels and is designated intravasion. Tumor cells that undergo this process are commonly named circulating tumor cells (CTCs). During this stage, CTCs must be able to escape recognition by the immune system cells and simultaneously survive the harsh conditions present in the bloodstream. If successful, these cells will begin the process of extravasion [34]. However, another obstacle arises, as these cells must find a way to go through the blood vessel wall of the new organ they intend to colonize. Since in most organs, the endothelial cells form a tight barrier, penetration of the cancer cells becomes arduous. Some studies suggest that circulating lymphocytes and platelets can form complexes with tumor cells using cell adhesion molecules (CAMs), namely P- and L-selectin. These are expressed in the surface of activated endothelial cells and promote the adhesion of platelets, which in turn arrests cancer cells and helps their passage through the vasculature. For this reason, high expression of P-selectin is often observed in many cancer types and is related to metastatic progression and poor prognosis [35].

After extravasion, CTCs encounter another hurdle when trying to adjust to a new environment, frequently very different from the one found in the primary tumor. Now they must achieve new features that will allow the establishment of new cell-cell interactions as well as cell-ECM connections that will contribute to the formation of a new microenvironment. Once that is determined, cells will begin to proliferate, leading to the formation of a secondary tumor [36].

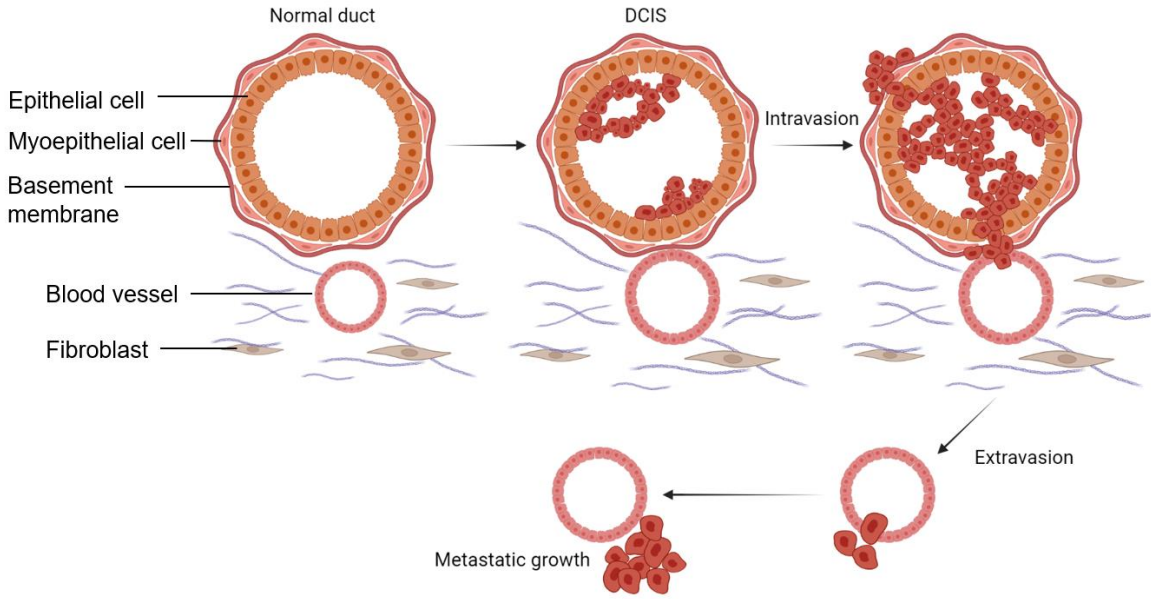

Figure 4 | The breast cancer metastasis cascade. DCIS – Ductal Carcinoma in situ. Adapted from [32].

Two renowned models are currently used to describe how a tumor evolves until eventually culminates in the formation of metastasis. The **linear progression model** explains how the disease progresses linearly, starting with invasion and ending with extravasion and metastasis, that occurs in a later stage in the tumor development. This correlates with minimal genetic differences observed between cells of the primary tumor and cells from its metastasis. On the contrary, the **parallel progression model** postulates that metastatic cells are seeded during early stages in tumor development, resulting in a bigger genetic difference from the primary tumor [37].

Studies have shown that breast cancer cells have a higher tendency to follow the parallel progression model of metastasis. This implicates that cancer cells rapidly spread from the primary tumor, and this often happens independently of its development. Different molecular subtypes of breast cancer have presented distinct organotropism, which suggests that the molecular features have an influence on the distribution of metastasis to certain organs [34]. A study conducted by the Surveillance, Epidemiology, and End Results Program has revealed that all subtypes are mainly prone to bone metastasis and even more significantly for the luminal subtypes (HER2-). Patients with the

subtype HER2-enriched have more brain metastasis, compared to HR+/HER2- patients. Liver metastasis were more frequently observed in the HER2+ subtypes, and triple-negative patients have a higher tendency for lung metastasis [38].

1.2.4 Angiogenesis In Tumor Progression

In the initial stages, a tumor is a conglomerate of cells without a vascular system. However, as the number of cells increases, oxygen and nutrients become scarce (especially in the core of the tumor), making it crucial for cells to find access to a blood vessel in order to continue proliferating. In this sense, angiogenesis is a key step in tumor progression, not only for nutrient attainment, but also for disposing of metabolic waste and carbon dioxide to maintain homeostasis.

Angiogenesis is regulated by a cooperation of pro- and anti- angiogenic factors. These molecules act as activators and inhibitors of the formation of new vessels respectively. When there is an equilibrium of these factors, endothelial cells are quiescent and, therefore, the vasculature remains unchanged. Up-regulation occurs when the net balance of these molecules tips towards a pro-angiogenic profile, which means there is an increase in activator molecules (such as vascular endothelial growth factor (VEGF) and the platelet derived growth factor-B (PDGF-B)), and a simultaneous decrease in inhibitor molecules [39].

This process has been denominated the **“angiogenic switch”** (Figure 5) and it can be triggered by chemical factors (hypoxia, nutrient deficiency, low pH), mechanical factors (increasing pressure caused by the proliferation of cells), the immune response (presence of inflammatory cells in the tumor microenvironment (TME)) or due to genetic mutations that cause the deletion of tumor-suppressing genes or activation of oncogenes [40], [41]. This switch ignites the rapid proliferation of neoplastic cells, together with the growth of new vasculature.

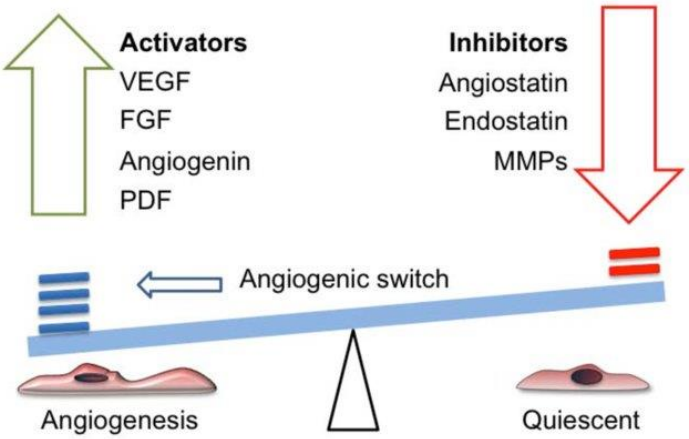

Figure 5 | The angiogenic switch. Activators 'outweigh' inhibitors and promote sprouting of ECs. Adapted from [41].

Blood vessels can be formed through different cellular mechanisms (Figure 6): sprouting angiogenesis, vasculogenesis, vasculogenic mimicry and intussusceptive angiogenesis.

Sprouting angiogenesis involves the outgrowth of cells from preexisting parental vessels leading to the formation of sprouts. It initiates with the disruption of endothelial cell-pericyte contact, when a cell from the host vessel goes through an endothelial–mesenchymal transition. This cell gains migratory ability and becomes the "tip cell", responsible of leading the process. At the base of the sprout, high proliferating cells will begin branch formation. These are designated "stalk cells" and they will assure vascular expansion and contribute to the integrity of the new sprout [42].

Vasculogenesis was first described as the mechanism of *de novo* formation of blood vessels in the embryo through differentiation of endothelial progenitor cells (EPCs). Later on, in the adult, vasculogenesis was found to play a role in the neo-vascularization of tumors as the need for oxygen and nutrients increases. Mediated by growth factors, cytokines and chemokines, EPCs are recruited from bone marrow to the tumor site. They will then differentiate into endothelial cells and integrate the new network of vessels [43]. Shirakawa *et al.* were able to isolate EPCs from three different areas (peripheral blood, bone marrow and from tumor-infiltrating cells) from mice bearing human breast cancer xenografts. This demonstrates that postnatal vasculogenesis can be induced in *in vivo* models [44]. Another work showed that mesenchymal stem cells (MSCs) are also capable

of gaining endothelial features when growing in endothelial growth medium. This was more evident when MSCs were cultured together with VEGF or MCF-7 cell line, revealing the formation of tubular structures resembling capillaries [45].

Vasculogenic mimicry refers to the formation of vessel structures by proliferating malignant cells. Endothelial cells do not contribute to this process. Instead, tumor cells can dedifferentiate, acquire endothelial-life phenotypes, and participate in the development of new pathways that will allow tumor growth and progression. This mechanism promotes the formation of a heterogeneous tumor vasculature which has been described as a possible reason for resistance to antiangiogenic drugs and therapy failure. Mao *et al.* report a novel subtype of cancer cells designated breast cancer stem-like cells (BCSLCs) that contributed to the establishment of new vessels through vasculogenic mimicry and could resist antiangiogenic therapy with sorafenib [46].

Intussusceptive angiogenesis is a faster process than sprouting angiogenesis because it does not require high proliferative endothelial cells. It consists in the splitting of a preexisting vessel into two new ones which contributes to the increase in the number of microvessels within the tumor. It starts with the formation of an interstitial pilar of endothelial cells within an existing vessel that eventually widens and creates two individual vascular structures. This process leads to a more complex microvascular network and provides a larger surface for activating other angiogenic mechanisms.

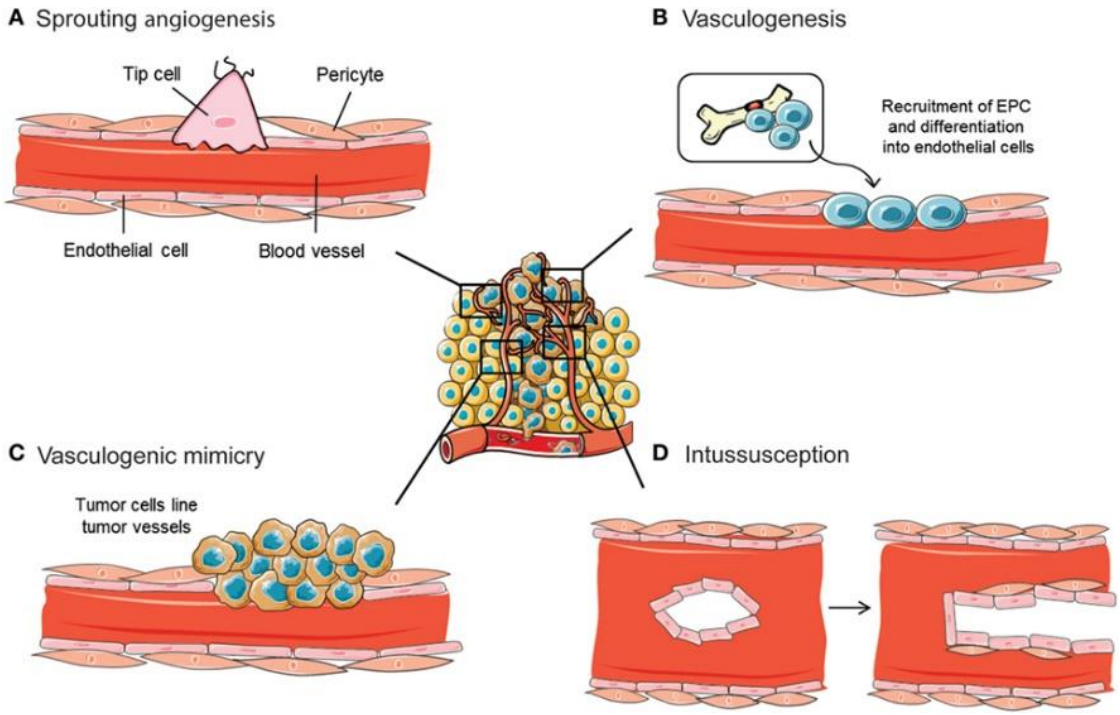

Figure 6 | Mechanisms for the formation of new blood vessels. Adapted from [42].

1.3 Brave Little Worlds - 3D *in vitro* Models of Breast Cancer

In this context, it becomes evident that the tumor vasculature is a defining factor in breast cancer prognosis, determining the formation of metastasis and the aggressiveness of the disease. Multiple research groups focus on unraveling the mechanisms behind angiogenesis to ultimately find an effective treatment for cancer that counteracts the development of metastasis.

In vitro, pre-clinical studies to evaluate the activity of a new candidate cancer drug have traditionally been performed in a bi-dimensional manner. Bi-dimensional models present various benefits like the low complexity, making it more practical to examine the distinct effect of each parameter tested. The problem is that the monolayer of cells ends up adapting to the two-dimensional (2D) environment and cells lose their original

phenotype. Moreover, these models do not truly represent the microenvironment of the tumor and are incapable of recapitulating the actual response of the malignant cells to the drug. This eventually contributes to the lack of efficacy of cancer drugs when tested in humans. When comparing with cardiovascular diseases (whose mortality reduced by 59%), cancer related deaths only decreased by 14% between 1975 and 2010 [47]. The lack of effective predictive cancer models makes the development of anti-cancer drugs a slow process, which in turn contributes to the fairly small decrease in mortality rates.

Three-dimensional (3D) cultures have been originally attempted by Emerman *et al.* around 1970s–1980s. The first trial was conducted with normal epithelial cells from the mammary gland cultured in collagen gels and demonstrated that the 3D environment could promote growth and differentiation with unique features, not observed in previous 2D cultures [48]. Therefore, the motivation to create more trustworthy models that more closely mimic the TME has led to the evolution of 3D models. Some examples will be discussed in detail in the following subsections, which are typical and illustrative rather than all-inclusive.

1.3.1 Organoids

The revolution of 3D culture models brought the development of organoids: miniaturized, *in vitro* tissue cultures that self-assemble and display a realistic micro-anatomy, correspondent of its parent organ. These constructs are derived from stem cells that can be either pluripotent (induced or embryonic) or adult stem cells from a specific organ or tissue. Initial studies involved culturing organoids from embryonic stem cells from cortical tissue or adult stem cells from intestinal tissue, but nowadays, reports include organoids that model the brain, retina, kidney, liver, and many other organs [49]. Organoids have also been applied in the study of multiple diseases, specifically different types of cancer.

When it comes to the study of breast cancer, organoids can be derived from different sources: primary breast tumor tissues, stem cells from the mammary gland, or even normal breast tissue.

Tissues originated from primary breast tumor can be mechanically and/or chemically dissociated. Organoid growth can be affected by cell concentration and nutrients available in the media. Hence, Sasmita and Wong recommend the use of promoters of stem cell survival (like fasudil) to avoid anoikis, and also the addition of growth factors to the media to further accelerate organoid growth [50]. Once formed, the organoid can be tested for the degree of invasion via viability assays and immunofluorescence analysis, and for *in vitro* drug-screening.

Bischel *et al.* combined organotypic culture with microfluidics to create a device that models the DCIS. They added DCIS cells with human mammary fibroblasts (hMF) and examined the transition to an invasive phenotype by the loss of cell polarity and cell-cell adhesions, typical of this breast cancer type [51].

Another example is presented by Dekkers *et al.* and comprises the use of normal breast tissue obtained from mammoplasties patients to generate breast epithelial organoids. They applied the CRISPR-Cas 9 technology to knock-out four tumor suppressor genes (PTEN, RB1, NF1, P53) from mammary progenitor cells and studied cancer progression and the organoid response to various therapies [52].

As previously stated, for breast cancer patients, metastatic disease is the leading cause of death. Since vascularization is one of the key aspects implicated in metastasis, scientists are trying to create models enriched with vascular structures that can replicate angiogenesis that occurs in tumors *in vivo*. Yanagisawa and colleagues developed a 3D organoid vascular system [53] based on a fibrin gel with collagen microfibers. This gel was then embedded with HUVECs, normal human dermal fibroblasts (NHDF) and cancer cells (HCT116 – human colon cancer cell line). Researchers observed that HUVECs could form lumen structures within the gel and that cancer cells could invade those structures. Additionally, they used the organoid model to study the effect that exosomes produced by cancer cells had on the ability of these cells to invade the capillary lumens. Results showed that the exosomes could decrease the number of tight junctions in the vascular endothelium and thus increase the permeability of these vessels. These eventually had a positive impact on the number of cancer cells that was found contained in the formed lumens.

Another challenge faced by research teams has been trying to replicate the later stages of metastasis (extravasion and colonization of the new site). The limited number of cells that undergo each step, together with the fact that some pertinent anatomical locations are inaccessible makes developing a model that faithfully recapitulates these events an arduous task. In this sense, novel animal models are being developed as a tool to better understand the core cellular mechanisms implicated in the final steps of the metastatic cascade. A published work describes the co-implantation of HUVECs and human MSCs derived from the bone marrow suspended in a Matrigel® matrix in immunodeficient mice [54]. This implantation resulted in the formation of mature, functional human blood vessels that were able to anastomose with the mouse's own vessels, hence forming vascularized organoids. Next, researchers evaluated the ability of human cancer cells of colonizing the organoid. For that, they inoculated mice with MDA-MB-231 cells and later detected the tumor cells in the organoid, including inside its vascular structures. Moreover, some cancer cells were already escaping the vasculature and invading the surrounding matrix. Altogether, these results represent a promising model to analyze the extravasion stage in a deeper detail, and help identifying new molecular targets for therapeutic purposes.

Organoids present countless advantages as study models. They are better platforms to study diseases when compared to animal models, that are far less convenient. Specifically, organoids possess faster obtainable endpoints and objective quantitative data. Organoids can also retain their phenotype for up to 70 days, and are more practical for immunofluorescence, which is relevant in the drug response prediction in breast cancer [55], [56] . Even though organoids serve as a powerful platform for understanding detailed features of an organ's development or how a disease progresses, they still present several downfalls. Most models lack vasculature, which means that they only grow until a finite size without experiencing significant cell death and they cannot be used to study processes where vascularization is a key component. Typical models also lack immune cells and they cannot entirely recapitulate the architectural structure of the *in vivo* organ [49].

Organoids are usually assembled in ECM-derived matrices such as Matrigel® that is extracted from a murine tumor. For this reason, Matrigel® presents poorly tunable

properties, high batch-to-batch variability, and intrinsic bioactivity. This hinders the comparison of results between different experiments or even laboratories, leading to a lack of reproducibility and compatibility with clinical applications [57]. Finally, organoid models are costly and not easily scalable, so the search for improved 3D culture methods still prevails.

1.3.2 Spheroids

Tumor spheroids are currently widely used models to replicate the architecture of a tumor *in vitro*. These spheroids are multicellular aggregates that allow the study of cell-cell interactions and also evaluate how the individual cell communicates with its own extracellular matrix (ECM) [58]. The basic principle to culture spheroids is that cells must prefer to adhere to each other instead of adhering to the bottom of the container they are plated on. Several methods may be applied to develop multicellular spheroids.

In **liquid overlay technique** cells are seeded in non-adherent plates coated with agarose or polyethylene glycol (PEG) that contain round-bottomed wells. In these conditions, cells end up aggregating and forming small colonies that have a regular shape and can be maintained in culture for several days [59]. Another method is using **spinner cultures**. The constant movement of the flask prevents cell adhesion to its surface and instead promotes cell-cell attachment and consequently spheroids' formation. The main advantage of this method is that it can be used to produce spheroids in a larger scale, but the mechanical forces applied can also result in damage of the cells [60]. **Hanging drop method** consists of plating cells in small drops of media on the lids of traditional culture plates and placing them upside-down. Gravitational force will then be the driver of cell aggregation. This a simple and cheap method, however, formed spheroids are not homogenous in size and it is low throughput [61].

Spheroids are commonly used as a 3D model for breast cancer since they can exhibit multiple tumor-like features. They can recapitulate the typical necrotic core encircled by quiescent cells, with an outer layer of active proliferating cells. Moreover, some reports have also showed their ability to display pH gradients, as well as oxygen and cell metabolites [59].

Many breast cancer spheroids are cultured using either MCF-7 or MDA-MB-231 cell lines. These can be cultured alone, creating spheroid monocultures or in combination with other cells, originating spheroid cocultures, tricultures and so on [62]. These multicellular tumor spheroids (MCTS), as they are also known for, have been widely applied in cancer research since they can mimic the heterogenous cell population and the pathophysiological gradients found in *in vivo* tumors. MCTS with diameters above 500 µm usually display three different layers owing to the gradient of nutrients and oxygen that forms from the outer to the center of the sphere (Figure 7). The first layer in the periphery of the spheroid is constituted by proliferating cells that have an easier access to oxygen and nutrients. Then it follows a layer of viable but quiescent cells and finally, the inner layer is formed by a necrotic core, due to the limited diffusion of nutrients and oxygen [63], [64].

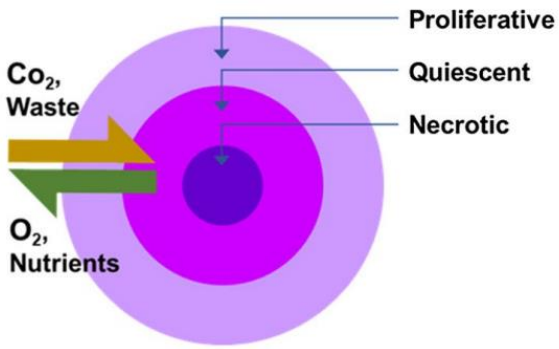

Figure 7 | The three layers in a MCTS: proliferative cells in the outer layer, quiescent but viable cells in the inner layer, and a necrotic core. Adapted from [64].

Since they contain multiple cell types, that are naturally present in the tumor, it makes it possible to create the typical heterogeneous environment and to evaluate how this affects tumor evolution [65]. Stromal cells typically recruited by cancer cells are fibroblasts, MSCs, pericytes, endothelial cells or immune cells, and they often change their phenotype, gaining a more permissive and tumor-supporting role that promotes cancer progression [66]. Hence, these stromal cells are responsible for assembling the tumor niche that provides de optimal conditions for the proliferation of neoplastic cells. As a result of the clear relevance of the TME in the development of cancer, models using

cocultures of breast cancer cells together with stromal cells are often performed to better mimic the *in vivo* conditions.

For example, **coculture of tumor cells with endothelial cells** is relevant to study the process of neo-angiogenesis which is one of the hallmarks of cancer. This ultimately leads to extravasion of tumor cells and metastasis [67]. Shoval *et al.* report the creation of hybrid spheroids containing endothelial cells and tumor cells (either from cell lines or patient-derived cancer cells) using four different methods [68]. Spheroids formed using agarose molds with micro-wells (Microtissues Inc., RI, USA) exhibited a more robust shape and they were more homogenous in size and circularity. Additionally, spheroids originated from patient-derived tumor cells and HUVECs exhibited the organization of endothelial cells (ECs) in tubular structures. Although these structures were primitive and non-functional, models like these can be the foundation for reliable predictive models of biological cancer processes.

Other examples comprise the **culture of breast tumor cells with fibroblasts**. These cells are highly abundant in the stromal compartment and are responsible for remodeling the ECM. The equilibrium between deposition and degradation of ECM constituents is crucial to keep a healthy functioning tissue. In cancer, this balance is disrupted when tumor cells recruit normal fibroblasts and stimulate their activation. This activated phenotype fibroblasts were coined cancer-associated fibroblasts (CAFs) and they are able to produce large amounts of ECM, stiffening the tumor circulating stroma. Contrary to normal fibroblasts, CAFs do not return to their original phenotype and are also resistant to apoptosis [66]. Besides resident fibroblasts, CAFs can be originated from other cell types such as MSCs derived from bone marrow, endothelial cells that undergo an endothelial-to-mesenchymal transition or cancer cells themselves that experience EMT [69].

Identification of CAFs can be carried out using different markers. Some of the markers currently being used are expression of alpha smooth muscle actin (α-SMA), fibroblast activation protein (FAP), fibroblast-specific protein (FSP-1), platelet-derived growth factor-α receptor (PDGFR-α), platelet-derived growth factor-β receptor (PDGFR-β), and vimentin. However, CAFs population can be extremely heterogeneous, with CAFs from different types of tissues expressing different markers. Ideally, a combination of

certain relevant markers would be the most suitable to identify a specific set of CAFs [70]. Activation of CAFs in breast cancer is mostly stimulated by factors derived from tumor cells, such as TGF-β, epidermal growth factor (EGF), and chemokine CXCL12, and evidence suggests that various other factors contribute to their activation. Downregulation of tumor-suppressor genes, like p53, p21, PTEN, and CAV-1, also plays a role on activation of these fibroblasts [66], [71] .

Mei *et al.* have developed a 3D model comprising breast cancer cells (MCF-7 or BT474) and either immortalized foreskin BJ1-hTert fibroblasts or human dermal fibroblasts (HDF) [72]. These coculture spheroids were then embedded in a synthetic matrix (Cultrex® Spheroid Invasion matrix - 3500-096-03 Trevigen), which allowed to understand that the presence of fibroblasts in the spheroids enabled tumor cells to invade into the matrix. Another work demonstrated that coculture spheroids with triple negative breast cancer (TNBC) cells and hMF or CAFs were a useful method to study interactions amongst these cell types. These spheroids revealed that CXCL12–CXCR4 signaling could significantly induce proliferation of cancer cells and also contribute to drug resistance via mitogen-activated protein kinase (MAPK) and phosphoinositide 3-kinase (PI3K) [71].

Spheroid models can be very useful for enlightening several features of tumor growth, as well as demonstrating the cell-cell interaction. However, they lack the matrix component that it is known to have a massive impact on the way tumor cells behave, and how the tumor progresses and metastasizes. Furthermore, they underrepresent more dynamic relationships happening in the microenvironment. Spheroids embody somewhat static models, and so they lack features related to transport across the endothelium, such as shear stress and hydrostatic pressure that highly influence tissue architecture [73].

1.3.3 Tumor-on-Chip Models

Microfluidic devices have increasingly been used as platforms to study the angiogenic process and how it is influenced by the application of different chemical gradients, flow profiles and ECM-like matrices. Microfluidics presents multiple advantages when it comes to developing models for oncological investigation. They require small

sample preparation and enable precise tuning of fluid properties. Moreover, they are cost-effective, portable, and allow for high-throughput measurements [74].

A microfluidic chip is a set of micro-channels that, depending on the material, may be fabricated resorting to soft lithography, hot embossing, micro-machining, or etching. The channels are connected to the outside by inlets and outlets that are punctured in the chip and function as the interface between the macro- and the micro- world. Polydimethylsiloxane (PDMS) is the elected polymer for the fabrication of microfluidic devices due to being chemically inert, presenting optical transparency, tunable stiffness, low toxicity, and permeability to gases. PDMS is mixed with a cross-linking agent and poured into a mold (for example a silicon mold) containing the microstructures. Once hardened, PDMS can be peeled from the mold and will exhibit the micro-channels previously drawn [75]. Microfluidics has been extensively applied in oncology research as a way to capture the tumor vascularized microenvironment by the integration of a perfusable vascular network. Nashimoto and colleagues developed a tumor-on-a-chip system (Figure 8) with three parallel channels that integrates breast cancer spheroids with endothelial cells [76]. The group applied coculture spheroids of normal human lung fibroblasts (hLF) and MCF-7 or tri-culture spheroids with the addition of human umbilical vein endothelial cells (HUVECs). This vascularized model was used to study the effects of paclitaxel administration on proliferation and cell death within the spheroids. The group demonstrated how dynamic conditions have a profound effect on dose-dependent responses of cells to anticancer drugs, showing the relevance of adding more dynamic conditions to *in vitro* models. This way, it will be possible to replicate *in vivo* tumor activities that contribute to the fabrication of reliable and effective drug screening platforms.

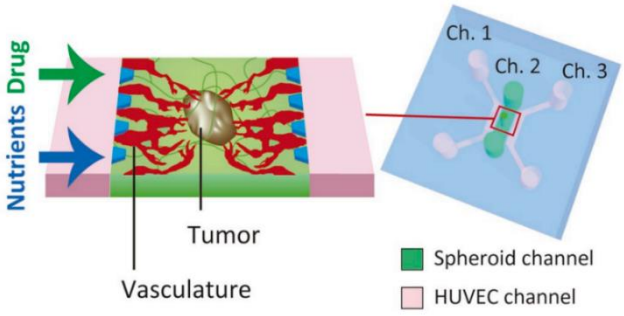

Figure 8 | Microfluidic platform designed by Nashimoto *et al.* to recapitulate in vivo tumor microenvironments (TMEs). Adapted from [76].

Other groups have focused on developing models that intend to mimic the extravasion stage during metastasis. Humayun *et al.* microfluidic platform consists of a collagen-fibrinogen matrix with a central channel in which they applied induced pluripotent stem cell derived endothelial cells (iPSCs-EC) to generate a vessel [77]. BCCs were then either injected through this vessel to evaluate the direct crosstalk between cancer and endothelial cells or in the adjacent channel to study paracrine signaling. Altogether, their results show that cancer cells upregulate the secretion of cytokines that promote extravasion of endothelial cells, namely IL-8 and IL-6. Contrarywise, iPSC-ECs produce MMP-3 that degrades components from the basement membrane and stimulates migration of cancer cells.

Despite the clear benefits that microfluidics brings to 3D cell culture, efforts need to be made when interpreting results and comparing cellular responses observed from this technology versus traditional 2D cell culture. It is important to have in mind that there is a wide range of designs, with multiple parameters that can be adjusted in a single device. Small changes in those parameters can determine very different outcomes, and cells will likely present behaviors that are specific to the microfluidic environment [78].

1.3.4 Bioengineered Matrices

In vivo, the ECM constantly interplays with cells, offering a multitude of biophysical and biochemical signals that modulate cellular behavior. Specifically, matrix stiffness, architecture and composition influence each stage of metastasis, from cancer cell proliferation to extravasion, as well as playing a part in cells' response to anticancer therapies.

ECM in cancer is responsible for specific structures such as the tumor capsule, that determines the communication between cancer cells and stromal cells. On the other side of the spectrum, cancer cells are able to degrade and produce ECM, remodeling it overtime. This remodeling is accompanied by changes in the biochemical composition that can transform the microenvironment into a more permissive one, allowing for numbness to therapy and tumor growth [79].

Among all biomaterials used to design 3D matrices, hydrogels have shown to be successful in replicating the native ECM. Hydrogels are hydrophilic cross-linked polymers that form 3D networks which can retain large amounts of water. They exist naturally which is the case of alginate, collagen, or Matrigel®, but can also be synthetically produced, like poly(hydroxyethyl methacrylate) (PHEMA) or polylactic acid (PLA). Besides their origin, hydrogels can also be classified according to their physical structure (amorphous, semicrystalline, crystalline, and hydrocolloid aggregates), ionic charge (anionic, cationic, non-ionic), preparation method (homopolymer, copolymer or interpenetrating networks (IPN)), and type of cross-linking agent, which can either be chemical or physical [80].

Several models include the embedding of tumor spheroids in a hydrogel matrix that mimics the ECM. This allows the creation of a model that represents the TME and depicts how it influences the cells [81]. One of the most widely used natural biomaterial is **type I collagen**, which is the most abundant protein of the ECM in mammals. It is a bioactive protein that promotes cell proliferation and adhesion and regulates various signaling pathways. Since collagen is naturally present in tissues, it makes it an attractive material for synthesizing hydrogels for cell embedding [82]. Plaster *et al.* have developed different coculture spheroids using a combination of TNBC cells (normal MDA-MB-231 or overexpressing CXCR4 receptors) and fibroblasts (normal hMF or CXCL12-producing hMF) [83]. These spheroids were then embedded in a collagen type I 3D matrix, where they were evaluated over a 5-day period. Matrix invasion by cancer cells was analyzed using confocal microscopy and they realized that the spreading of the cells was influenced by two different phenomena: splitting of the two cell types in the $CXCR4^{+}$TNBC:hMF coculture spheroids and invasion into the matrix performed by cancer cells in the $CXCR4^{+}$TNBC:$CXCL12^{+}$hMF spheroids. When blocking the CXCR4-CXCL12 signaling using a CXCR4 antagonists, they could see that matrix invasion was clearly reduced in the $CXCR4^{+}$TNBC:$CXCL12^{+}$hMF model, but not in the second model, where fibroblasts were not expressing CXCL12. They realized that segregation of the two types of cells only occurred in the second model, and this segregation was responsible for the dispersion of the cells into the matrix [83].

Another example was performed using triculture spheroids with breast cancer cell line MDA-MB-231, endothelial cells and fibroblasts in a ratio of 2:2:1 respectively [84].

These spheroids were then embedded in collagen-type I gels to study angiogenesis. This work demonstrated that endothelial cells formed tubular-shaped structures and that their sprouting was supported by fibroblasts and promoted by the cancer cells. Moreover, the model was used to study the role of MT1-MMP (Membrane-Type 1 Matrix Metalloproteinase) in sprout formation. Each cell type was transduced by delivering short hairpin RNA (shRNA) targeting the metalloproteinase. The knock-down of this protein in the endothelial cells and fibroblasts resulted in reduced sprouting, but that was not observed for the breast cancer cell line.

Another biomaterial is **fibrin**, a natural hydrogel which polymerization is initiated by the conjunct action of thrombin and fibrinogen and that has been applied in several biomedical fields. Its widespread application can be attributed to its biocompatibility and excellent 3D processing capabilities [85]. Ehsan and colleagues developed a method to produce spheroids containing tumor cells and endothelial cells in a 3:1 ratio that were then embedded in a fibrin gel that also contained normal human lung fibroblasts (NHLF) dispersed [86]. They applied this method with multiple malignant cell types including breast cancer cell lines (MCF10A and MDA-MB-231). Their model showed that tumor cells were able to separate from the initial tumor mass and migrate the surrounding matrix, and that endothelial cells could form capillary-like structures, that was enhanced under hypoxic conditions.

Matrigel® is another protein-based hydrogel used for spheroid growth *in vitro*. Breast cancer cell lines were cultured embedded in a Matrigel® matrix and it was discovered that the neoplastic phenotype could be reverted to the normal phenotype by inhibiting the receptor for β1-integrin or by decreasing the expression of epidermal growth factor receptor (EGFR) [87]. Moreover, Matrigel® was also used to embed 3D cultures of various breast cancer cell lines as a platform to study the correlation between cell morphology and gene expression profiles [88]. As previously stated for organoids, Matrigel® has a widespread application in cell culture. Nevertheless, this matrix is known to have limited applicability due to its poorly defined composition, batch-to-batch variability and its animal origin. For this reasons, some uncertainty regarding interpretation of results and their reproducibility has been reported [89].

Another example is the 3D culture of MDA-MB231 in RGD-modified **alginate** hydrogels. Fischbach *et al.* observed that a high expression of IL-8 appears to be a marker of greater metastatic potential. Additionally, this overexpression was only observed when in contact with RGD-modified alginate and not as a response to 2D to 3D culture transition. This suggests that integrin engagement plays a role in the severity of a tumor by influencing cell proliferation [90]. Alginate hydrogels present key advantages such as low batch-to-batch variability, defined xeno-free composition, and, most importantly, precisely customizable biochemical/physical properties. Moreover, owing to its natural origin, alginate-based models are typically considered much safer for clinical applications, when comparing to synthetic polymers, due to their ability to biodegrade and to their biocompatibility. Our group has demonstrated that biofunctionalized alginate-based platforms, traditionally associated with tissue engineering approaches, can be successfully translated into cancer research for the design of advanced 3D *in vitro* models. We successfully developed a new 3D alginate-based model to investigate the role of the ECM on epithelial-to-mesenchymal transitions (EMT) and its reversion (MET) that are closely linked to cancer progression [91]. Additionally, we designed a unique 3D *in vitro* platform to dissect tumor-stroma interactions in tumor angiogenesis [92]. We established triple cultures of fibroblasts, epithelial and endothelial cells in hybrid hydrogels enabling direct and indirect cell-cell communication. The use of such model will greatly improve our understanding of tumor-driven angiogenesis.

1.4 Alginate – The Attractive Seaweed Product

Although biomaterials may sound like an invention of the modern world, they have been around for ages. Biomaterials are likely as ancient as the Egyptian civilization as it is reported the use of metallic implants to fix bone fractures. Other articles mention the discovery of a skull in Perú from 2000 BC displaying a bone defect fixed with a small piece of gold [93]. From then, biomaterials kept on evolving at light speed, and around 1970's, the first-generation of biomaterials emerged. In these early stages of biomaterial fabrication, scientists aimed to design something that was inert and did not interact with the biological systems of its host. The goal for the ideal biomaterial was to achieve a set of suitable physical properties that matched the tissue it was replacing and simultaneously maintain a minimum toxicity for the host. More recently, biomaterials evolution led to a fairly different definition, as now they are intended to have a more biological interaction with native tissues. More materials are being designed with bioactive features that aim to promote a more regenerative profile and that are able to interact with cells and modulate their response in terms of proliferation and differentiation, for example [94].

Nowadays, scientists are focused on achieving biocompatibility, creating biomaterials that mimic functions observed in the native tissues and that they can precisely tune in order to get specific outcomes. In that sense, natural biomaterials are gaining momentum mainly due to their intrinsic biocompatibility.

Alginate is isolated from different species of brown seaweeds (*Phaeophyceae*), which are highly abundant marine plants, thus making it an easily obtainable natural biopolymer. The low toxicity, reduced cost and versatile chemistry make alginate an attractive material for biomedical applications, where is currently extensively studied. Alginate is a structural component from the cell wall, generally insoluble, that is then washed, dried and turned into a powder. Next, the addition of NaOH or KOH to form sodium/potassium salt of alginic acid makes it water-soluble [95].

Structurally, it consists of a linear unbranched polysaccharide containing (1,4) linkages between β-d-mannuronic (M) and α-l-guluronic (G) acids. It can be composed of M-blocks (consecutive M residues), G-blocks (consecutive G residues) and MG-blocks (alternating G and M residues) with the G:M ratio varying depending on the source (Figure

9). Viscosity is affected by pH, increasing with the decrease of pH (reaching a maximum at pH ~ 3,5) due to protonation of the carboxylic groups in G monomers that allows for the formation of hydrogen bonds [96]. Mannuronic monomers moderate the polymer's elasticity, so gels formed with a higher content of M-blocks are softer and more elastic, with a higher rupture strength. On the other hand, gels with a higher percentage of G-blocks are hard and brittle and present increased water retention ability [97].

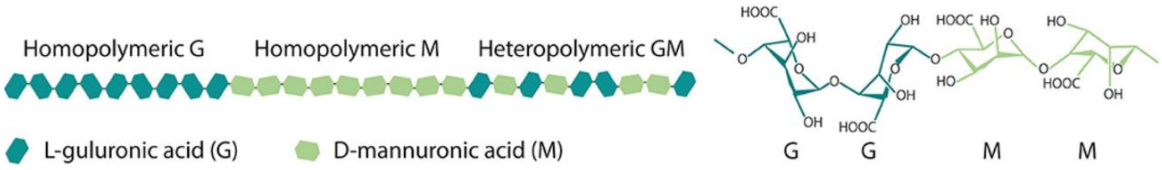

Figure 9 | Alginate structural data. Adapted from [105].

Alginates are anionic polymers that quickly form hydrogels by a process of chemical and/or physical cross-linking. Gelation of aqueous alginate may be performed by ionic cross-linking with divalent (Ca^{2+}, Sr^{2+}, and Ba^{2+}) or trivalent ions (Fe^{3+} and Al^{3+}) that interact with the G-blocks, which in turn form junctions with the G-blocks of adjacent polymer chains. Commonly, it happens in the presence of Ca^{2+} ions through a mechanism known as the egg-box model. Ionic cross-linking can occur by external gelation where calcium ions diffuse into the polymer droplets or internal gelation when calcium is slowly released into the polymer solution [98], [99]. Various studies have reported that internal gelation produces more homogeneous gels, however it takes longer than the external gelation [100]. Other types of cross-linking include covalent cross-linking, thermal gelation, or cell cross-linking (for alginate modified with adhesion ligands such RGD) [95]. This gelling features makes it a prime candidate for applications such as encapsulation of drugs in drug-delivery systems or the embedding of cells in its matrix.

Alginate chemical structure allows for a variety of possible modifications making it available with different functions for multiple applications. These modifications can tune the material's features such its stiffness or they can be related to functionalization. Functionalizing alginate with different receptors will influence the cell's response in

specific ways (for example in terms of adhesion to the substrate) and it can also be used for targeting purposes, as it is commonly applied in cancer-targeted therapy [101]. Barros da Silva *et al.* developed a hybrid 3D breast model that combines stromal cells with epithelial cells [102]. Porous alginate scaffolds were 3D printed and populated with hMF to create the stromal compartment, while an alginate gel laden with mammary epithelial cells recreated the parenchymal compartment. The gel was then used to fill the scaffold's pores forming an heterotypic system that promotes a crosstalk between the two types of cells together with cell-ECM interactions. As alginate naturally impedes cell adhesion, both alginate components were modified with RGD peptide to promote integrin-based adhesion. Fibroblasts in the scaffold showed enhanced spreading, and were able to fully populate the surrounding matrix [102].

Alginate composites have also been explored as a way to create hybrid systems that provide a more detailed control over the material's properties and expand its versatility. Cavo *et al.* combined alginate with Matrigel® in a 1:1 ratio forming a hydrogel that was then laden with the highly metastatic MDA-MB-231 cell line. This hydrogel influenced the cell cytoskeleton in a way that closely resembled the initial steps of metastasis observed *in vivo*. Cells presented the formation of actin-based structures that allowed their migration through the extracellular matrix and that conferred them a more elongated shape, which is characteristic of their neoplastic origin [103].

Motivation and Goals

Breast cancer is a disease with a tremendous negative impact in the life of an increasing number of people. Consequently, it is of primary importance to invest in studying the multiple factors that influence its initiation and progression. In that sense, *in vitro* models have played a crucial part in understanding the disease in more detail. Now, we are able to take a closer look at how cells communicate with each other and with the neighboring matrix in the cancer environment. Namely, 3D *in vitro* models are gaining traction, as the need to accurately replicate the cell-cell interactions that occur in the tumor is becoming more relevant. Amongst different 3D models, spheroids have emerged as a powerful tool. By being more physiologically pertinent, they provide a higher predictive potential when moving from *in vitro* to *in vivo* tests. Additionally, tumors, including breast cancer, are characterized by presenting various cell types, each with its own role in tumor development. Hence, it was important to represent that in the final model by incorporating not only the cancer cells, but also stromal cells, such as fibroblasts and endothelial cells.

The relevance of the tumor microenvironment is a factor that no longer leaves room for doubts, with the vasculature being one of the key factors influencing cancer evolution. With this in mind, we set the goal to embed the cultured spheroids in a 3D matrix that could capture the complex *in vivo* setting, where cancer cells are naturally inserted in. Hydrogels are typically the polymer of choice, and specifically alginate presented all the desirable features, as previously reported by our group [91], [92], [104], [105]. This system was crucial to dissect a multitude of interactions between cancer and stromal cells, as well as to highlight the role of angiogenesis in breast cancer.

By combining the relevance of spheroid models with the versatility of alginate, coupling up with microfluidics, we aimed to develop a hybrid model that more precisely reproduces the breast tumor *in vitro*. Hereafter, the main goals for this thesis were (Figure 10):

a) To produce coculture spheroids of breast cancer mammary epithelial cells and fibroblasts that represent the tumoroid model.

b) To develop coculture spheroids of endothelial cells and fibroblasts that embody the vascularized tumor compartment (designated as the vascular units model).

c) To incorporate both previous models in alginate and integrate them in a single microfluidic device that allows the evaluation of interactions between all the different cell types and the angiogenic potential of the whole system.

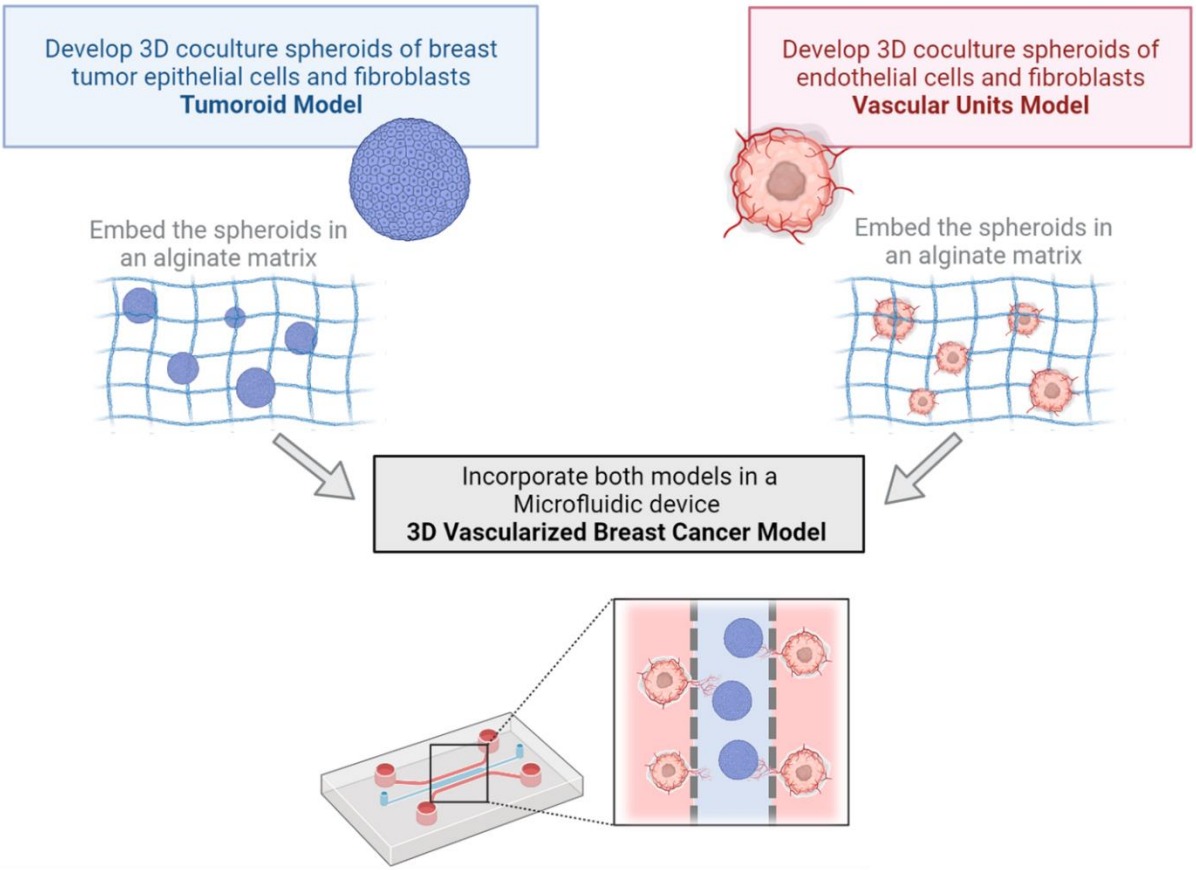

Figure 10 | Graphical Abstract. Schematical representation of the main goals and overall strategy to establish a 3D Vascularized Breast Cancer Model.

Chapter 2 - Materials and Methods

2.1 Cell Maintenance

Primary Cultures

Outgrowth endothelial cells (OECs) were previously isolated from human umbilical cord of healthy donors as previously reported [106]. OEC medium consisted on MCDB131 basal medium (Gibco) supplemented with 5% v/v FBS (Biowest), 1% of penicillin/streptomycin solution (Pen/Strep, Biowest), 2 mM L-glutamine (200mM, Biowest), 1 µg/mL ascorbic acid (1 mg/mL, Sigma), 0.2 µg/mL hydrocortisone (0.5 mg/mL, Sigma), 2 ng/ml VEGF (2 µg/mL, ImmunoTools), 20 ng/mL IGF-1R (20 µg/mL, Sigma), 10 ng/mL FGF (10 µg/mL, PeproTech) and 5 ng/mL EGF (100 µg/mL, Sigma). OECs were used between passages 7 and 10.

Normal human mammary fibroblasts (nFib) were cultured and maintained in Dulbecco's Modified Eagle Medium with Glutamax (DMEM GlutaMAX™ (Gibco) supplemented with 10% v/v non inactivated FBS (Biowest) and 1% v/v of Pen/Strep. nFib were used between passages 8 and 11 in the experiments.

Cancer associated fibroblasts (CAF) were also maintained in DMEM GlutaMAX™ (Gibco) and used between passages 8 and 11.

Before seeding both nFib or CAF, the T-flasks were previously coated with poly-L-lysine solution (15 µL in 10 mL of filtered deionized water) to assure a better and more efficient cell adhesion and proliferation.

To assure physiological conditions, cells were cultured in 75 cm^2 T-flasks and kept at 37ºC in a 5% v/v CO2 humidified incubator. Medium was changed every other day, and when cells reached about 80%-90% confluence they were passaged.

Cell Lines

The epithelial cell line MCF-7 was cultured in DMEM/F12 without phenol red (Gibco, ref:21041), supplemented with 10% v/v inactivated FBS (Biowest) and 1% v/v Pen/Strep. These cells were also kept in 75 cm^2 T-flasks inside a 5% v/v CO^2 humidified incubator at 37ºC.

Gene expression

nFib and CAF from different passages were collected. Pellets were then recovered by suspension and centrifugation in phosphate buffered saline (PBS, pH 7.4). For mRNA expression quantification, RNA was extracted from hydrogels using the Quick-RNA MiniPrep (Zymo Research), as recommended by the manufacturer. Subsequently, RNA was reversed transcribed to single stranded cDNA using Takara cDNA synthesis kit. Quantitative Real-Time PCR (qRT-PCR) was carried out using source RNA from 3 biological replicas for the target genes Fibronectin (FN,), type I collagen (Col1a1, Hs.PT.58.15517795), matrix metalloproteinase-2 and -12 (MMP2, MMP12), vimentin (Vim), alpha-smooth muscle actin (α-SMA), Fibroblast Activation Protein (FAP), Fibroblast-Specific Protein 1 (FSP-1) and for endogenous control GAPDH (Hs.PT.51.1940505) using as probe sets Hs.PT.58.40986315, Hs.PT.58.15517795, (Applied Biosystems and Integrated DNA Technologies), respectively. Samples were run in triplicates in the ABI Prism 7000 Sequence Detection System under the following conditions: 95 ºC for 20 sec, followed by 40 cycles at 95 ºC for 3 sec and 60 ºC for 30 sec.

2.2 Agarose Molds Preparation

Agarose molds were prepared according to manufacturer's protocol (MicroTissues®, USA). Briefly, 50 mL of 0.9% (w/v) NaCl was added to a flask containing 1 g of high quality pure autoclaved agarose powder to obtain 2% w/v agarose. The agarose was then melted and filtered in sterile conditions. Afterwards, 330 µL of melted agarose were pipetted into a silicon template mold (MicroTissues® 3D Petri Dish® micro-mold, 24-35 and 24-96). Two different molds were used (Figure 11): one was size large, with 35 U-shaped micro-wells (5 x 7 array) and the other was size small, with 96 U-shaped micro-wells (8 x 12 array). Once hardened, the agarose mold was carefully detached, placed in a 24-well plate, and equilibrated in culture medium overnight (ON) inside an incubator.

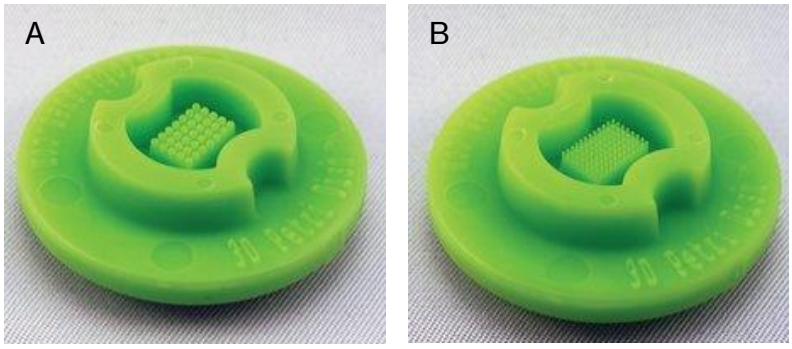

Figure 11 | Silicon 3D Petri Dish® micro-molds used to produce agarose molds. A) Mold for large spheroids - 24-35. B) Mold for small spheroids 24-96.

2.3 Spheroid Generation

Vascular Units (VUs)

To generate VUs, cocultures spheroids of OECs and CAF/nFib were prepared. In some experiments, spheroids contained a total of 10 000 cells/spheroid with ratios of 1:1, 1:5 or 5:1 OEC:CAF/nFib. Spheroids were prepared in the large molds with a total number of 35 000 cells/mold.

In another experiment, coculture spheroids were generated with different cell densities: 1000, 500, 250 and 125 cells/spheroid with a ratio of 1:5 (OEC:CAF/nFib). These spheroids were prepared in the small molds (24-96).

Cells were first trypsinized and counted using a Neubauer chamber. The correspondent volumes were then calculated and collected from each cell suspension to form a mixed suspension for each condition. Next, cells were centrifuged (1200 rpm, 5 minutes) and resuspended in the appropriate volume of culture medium (75 µL per mold). After seeding, cells were left for 30 minutes in the flow chamber at RT to allow for cell settling. Later, 1 mL of culture medium was added to each well.

Tumoroids

To produce spheroids for the tumoroid model MCF-7 cells and CAF or nFib were used. Different strategies were adopted in order evaluate which one enabled the production of spheroids with a higher density of cancer cells in the center and a periphery mostly populated by fibroblasts.

A first experiment involved seeding both types of cells simultaneously to form spheroids with a total of 4000 cells in a 1:1 ratio. Spheroids were prepared in the small molds and further steps followed the methodology adopted for the generation of VUs.

A different set of experiments consisted in the addition of fibroblasts (CAF/nFib) 1 or 6 days after seeding the MCF-7 cells (sequentially). In the sequential seeding after 1 day, tumoroids had a total of 4 000 cells/spheroid with a 1:1 ratio. For the sequential seeding after 6 days approach, tumoroids were generated with 10 000 cells/spheroid and 1:1 and 1:4 ratios (MCF-7:CAF/nFib). The medium was firstly removed, and the appropriate volume of fibroblasts suspension was then added to the molds.

For all the previous experiments plates were incubated at 37 °C under a 5% v/v CO^2 humidified atmosphere. Cell culture medium was changed every other day. Brightfield images were obtained at day 1, 3/4, 7 and 14 using the Inverted Fluorescence Microscope Axiovert 200M (Zeiss), at magnifications 5X and 10X. Spheroid's diameter was measured using the brightfield images with the Fiji/ImageJ software.

2.4 Viability of VUs and Tumoroids

To assess the viability of the VUs and tumoroids the CellTiter-Glo® 3D Cell Viability Assay (ProMega) was used, which is specifically designed to determine the viability of 3D microtissue spheroids. This assay reagent measures ATP as an indicator of viability and generates a luminescent readout. The amount of ATP in the sample is proportional to the amount of metabolically active cells.

First, a defined number of spheroids (usually around 4) were transferred from the agarose mold to a white opaque 96-well plate together with 100 µL of culture medium and 100 µL of CellTiter-Glo® 3D reagent for each condition. Control wells containing medium without cells were prepared to obtain a value for background luminescence. The plate was shaken for 5 minutes in the microplate reader (Synergy MX, BioTek) to induce cell lysis, and then incubated for 30 minutes at RT. Next, luminescence was measured using the microplate reader (integration time of 0.5s, sensitivity of 135, top probe vertical offset of 1 mm).

2.5 Sprouting Assay - Embedding VUs in Fibrin

First, it was necessary to prepare the fibrin gel. For that, two solutions were necessary: solution A – containing fibrinogen (weighted and dissolved in 0,9% NaCl), aprotinin, and cell culture medium; and solution B – with PBS and thrombin. Afterwards, solution A and B were mixed and 300 µL were added to the bottom of an Ibidi well (4-well Ibidi) and left for 20 minutes to let the fibrin polymerize (Figure 12). Next, 4-5 spheroids were placed on top of the fibrin layer and a second layer (300 µL) was added over the spheroids. Finally, cell medium was added to the wells and the Ibidi slide was incubated at 37 °C under a 5% v/v CO^2 humidified atmosphere. Cell culture medium was changed every other day and images were acquired at day 1, 3 and 7 using a ZOE™ Fluorescent Cell Imager (BioRad).

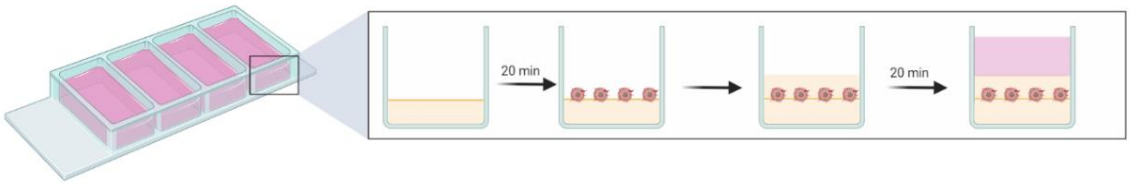

Figure 12 | Schematization of the Sprouting Assay.

2.6 Live/Dead Assay of VUs

Briefly, ethidium homodimer stock solution (2 mM in DMSO:ddH2O, 1:4) and calcein stock solution (1 mg/mL) were diluted in 1 mL of cell culture medium. Then, 250 µL of each solution were added to the samples and incubated for 45 minutes in 5% CO^2 at 37ºC. After the incubation time, samples were washed and observed under confocal laser scanning microscope (CLSM, Leica TCS-SP5 AOBS, Leica Microsystems).

2.7 Immunohistochemistry of spheroids for CLSM

Whole-mounted samples

VUs embedded in fibrin were fixed directly in the Ibid slide at days 1, 3 and 7 using 4% w/v PFA (30 min, RT). Samples were permeabilized in 0.25% v/v Triton X-100 (Fisher Scientific) in PBS for 20 min, washed twice with 0.05% v/v Tween-20 (Fisher Scientific) in PBS for 10 minutes, and blocked with 5% w/v BSA for 1h at RT, all the steps with agitation.

Then the samples were incubated ON with the following primary antibodies diluted in 1.5% w/v BSA: mouse anti-CD31 (Dako, 1:100); rabbit anti-laminin (Sigma, 1:100); rabbit anti-von Willebrand Factor (vWF, Dako, 1:50); mouse anti-alpha smooth muscle actin (α-SMA, Abcam, 1:200), and 4',6-diamidino-2-phenylindole (DAPI, 1:1000) (Table 1).

Samples were then washed twice with 0.05% v/v Tween-20 and incubated with the corresponding fluorochrome-conjugated secondary antibodies (Alexa 488 anti-

mouse, Alexa 488 anti-rabbit, Alexa 594 anti-mouse and/or Alexa 594 anti-rabbit, Invitrogen, 1:500) for 4h at RT. After washing twice with 0.05% v/v Tween-20 for 10 minutes, PBS was added, and samples were imaged in Confocal Laser Scanning Microscopes Leica TCS SP5 and SP5II (Leica). Data analysis was performed using Fiji Imaging software.

Table 1 | Stainings performed in the whole-mounted samples of VUs embedded in fibrin. The first antibodies were added together with DAPI (1:500).

	1st Antibody	Dilution	2nd Antibody	Dilution
Staining 1	Mouse anti-CD31 (M0823)	1:100	Anti-mouse 594 (A11029)	1:500
	Rabbit anti-laminin (L-9393)	1:100	Anti-rabbit 488 (A11072)	1:500
Staining 2	Mouse anti-α-SMA (A5188)	1:200	Anti-mouse 488 (A11029)	1:500
	Rabbit anti-vWF (A0082)	1:50	Anti-rabbit 594 (A11072)	1:500

Paraffin-embedded sections

VUs or tumoroids were fixed at days 1, 3/4 and 7, directly in agarose molds, with 4% w/v PFA (20 min, RT). Each mold was sealed with 100 µL of molten agarose and spheroids were further processed and paraffin embedded. Afterwards, 3 µm sections were obtained and stained for Hematoxylin and Eosin (HE) and used for immunohistochemistry. Briefly, sections were deparaffinized and rehydrated, stained 5 minutes in Gill's Hematoxylin and tap water washed. Afterwards, sections were stained in

Eosin for 4 minutes, dehydrated and mounted in Entellan. Sections were then deparaffinized in xylene (5 minutes, 3 times) and rehydrated in sequentially decreasing ethanol concentrations (from 100% to 50%, for 5 minutes). Antigen retrieval was performed with TE buffer solution (10 mM Tris and 1 mM EDTA, pH 9) or citrate buffer (10 mM, pH 6), at 90 °C for 30 min. Sections were then washed 3 times with PBS under agitation, permeabilized in 0.25% v/v Triton X-100 for 10 min, washed again with PBS, immersed in 200 mM ammonium chloride for 10 minutes, washed 3 times with PBS, and blocked with 1,5% w/v BSA and 5% v/v FBS in PBS for 1h at RT. After, samples were incubated ON, at 4ºC, with the following primary antibodies diluted in blocking solution (Table 2 and Table 3Table 2): mouse anti-CD31 (Dako, 1:50); rabbit anti-fibronectin (FN, Sigma, 1:100); rabbit anti-laminin (Sigma, 1:100); rabbit anti-von Willebrand Factor (vWF, Dako, 1:100); mouse anti-vimentin (VIM, Santa Cruz, 1:200); mouse anti-alpha smooth muscle actin (α-SMA, Sigma, 1:200); rabbit anti-E-cadherin (E-cadh, Cell Signaling, 1:100); rabbit anti-ZO-1 (ZO-1, Thermofisher, 1:100); mouse anti-β-catenin (β-catenin, BD Biosciences, 1:100); mouse anti-collagen type IV (COL IV, Dako, 1:100); rabbit anti-collagen type I (COL I, Rockland, 1:100); and 4',6- diamidino-2-phenylindole (DAPI, 1:500). Sections were then washed with PBS and incubated with the corresponding fluorochrome-conjugated secondary antibodies (Alexa 488 anti-mouse, Alexa 488 anti-rabbit, Alexa 594 anti-mouse or Alexa 594 anti-rabbit, Invitrogen, 1:500) for 1h at RT. Samples were then washed and mounted with VectaShield and imaged in the Confocal Laser Scanning Microscope Leica TCS SP5. Data analysis was performed using Fiji Imaging software.

Table 2 | Stainings performed on histological sections of VUs (OEC:CAF/nFib). The first antibodies were added together with DAPI (1:500).

	1st Antibody	Dilution	2nd Antibody	Dilution
Staining 1	Mouse anti-CD31 (M0823)	1:50	Goat anti-mouse 594 (A11020)	1:500

	Rabbit anti-fibronectin (F3648)	1:100	Goat anti-rabbit 488 (A11008)	1:500
Staining 2	Mouse anti-vimentin (Sc-6260)	1:200	Goat anti-mouse 488 (A11029)	1:500
	Rabbit anti-vWF (A0082)	1:100	Goat anti-rabbit 594 (A11072)	1:500
Staining 3	Mouse anti-CD31 (M0823)	1:100	Goat anti-mouse 594 (A11020)	1:500
	Rabbit anti-laminin (L-9393)	1:100	Goat anti-rabbit 488 (A11008)	1:500
Staining 4	Mouse anti-Col IV (M0785)	1:100	Goat anti-mouse 488 (A11029)	1:500
	Rabbit anti-Col I (600-401-103-0.1)	1:100	Goat anti-rabbit 594 (A11072)	1:500

Table 3 | Stainings performed on histological sections of tumoroids (MCF-7 and CAF/nFib). The first antibodies were added together with DAPI (1:500).

	1st Antibody	**Dilution**	**2nd Antibody**	**Dilution**
Staining 1	Mouse anti-vimentin (Sc-6260)	1:50	Goat anti-mouse 488 (A11029)	1:500
	Rabbit anti-E-cadherin (3195)	1:100	Goat anti-rabbit 594 (A11072)	1:500

Staining 2	Mouse anti-α-SMA (A5188)	1:200	Goat anti-mouse 488 (A11029)	1:500
	Rabbit anti-ZO-1 (61-7300)	1:100	Goat anti-rabbit 594 (A11072)	1:500
Staining 3	Mouse anti-β-catenin (610153)	1:100	Goat anti-mouse 488 (A11029)	1:500
	Rabbit anti-fibronectin (F3648)	1:100	Goat anti-rabbit 594 (A11072)	1:500
Staining 4	Mouse anti-Col IV (M0785)	1:100	Goat anti-mouse 488 (A11029)	1:500
	Rabbit anti-Col I (600-401-103-0.1)	1:100	Goat anti-rabbit 594 (A11072)	1:500

2.8 Maleimide-Alginate Production

Ultrapure low viscosity (≈199 mPa) sodium alginate (PRONOVA UP LVG, Novamatrix, FMC Biopolymers) 07-02), with a molecular weight of 197.9 kDa and an approximate content of guluronic acid of 70% was modified with maleimides. Maleimide was introduced into the backbone of alginate by amidation of the carboxyl groups of alginate with the amine groups of 1-(2-Aminoethyl)maleimide, using 4-(4,6-Dimethoxy1,3,5-triazin-2-yl)-4-methylmorpholinium chloride (DMTMM) (Mw: 276.72) as the coupling reagent. In brief, alginate (1% w/v) was dissolved in ultrapure (UP) water, and DMTMM was added to activate the polysaccharide carboxyl groups (e.g. 100% COOH activation: 1.34 g of DMTMM per g of alginate) and left to react for 30min. Subsequently, 21.2 mg maleimide / g alginate was added, and the mixture was stirred at RT for 24h. The reaction products

were dialyzed against decreasing solutions of NaCl in UP water for 3 days. Lastly, the samples were filtered and lyophilized to remove the water from maleimide-alginate and stored at -20ºC for further use. The degree of substitution was assessed by ^{1}H-NMR. Spectra were acquired on a 400MHz Bruker spectrometer and analyzed using the MestReNova software. NMR samples were prepared 1.3-1.5 % w/v in D_2O and TSP (trimethylsilylpropanoic acid) at 0.05M was added as an internal standard. DS was determined correlating the area of ALG peaks (δ = 4.97-5.13 and 3.33-4.53 ppm) with the new maleimide peak (δ = 6.82-6.97 ppm), according to the following equation (1):

$$\text{MD} = \left(\frac{\frac{\int \delta M}{H_{\delta M}}}{\frac{\int \delta ALG}{H_{\delta ALG}} + \frac{\int \delta M}{H_{\delta M}}} \right) x\ 100\ (\%) \quad (1)$$

where integrals correspond to the area of the peaks in a particular δ and H corresponds to the number of protons attributed to those same peaks.

Rheological characterization

The gelation kinetics with the CGPQGIWGQC peptide (further referred as GI-linker) was evaluated by single frequency oscillation assay, using a Kinexus Pro rheometer (Malvern). Maleimide-alginate was dissolved in HBSS and, immediately after adding the crosslinker, the hydrogel precursor was placed between the rheometer plates. Different final GI concentrations were tested: 120 μM and 240 μM. The parameters used were: Frequency (Hz)= 0.05 Hz, Sheer strain (%) = 1, Gap (mm)= 0.5 mm, Temperature (ºC) = 37. The storage modulus (G') and the loss modulus (G") were monitored.

2.9 3D Culture within Bioresponsive Alginate

Maleimide-alginate at 2.2% w/v was previously prepared and used to synthesize RGD-alginate. RGD peptide (CG_4RGDSP) was grafted to the maleimide-alginate backbone through the Thiol-Michael addition reaction. During this reaction, the thiol group of the cysteines (present in each end of the peptide) reacts with the double bound of the maleimide ring, producing RGD-alginate with a concentration of 2% (w/v). Spheroids were

collected and resuspended in HBSS and added to the RGD modified-alginate solution. Afterwards, crosslinking occurred with the addition of a protease sensitive peptide, CGPQG↓IWGQC (the arrow indicates the site of cleavage) reaching a final concentration of 1% (w/v). Then, droplets of 20 µL were placed between Teflon plates separated by 750 µm spacers and the alginate was left to polymerize for 20 minutes at 37ºC (Figure 13). The hydrogels were transferred to 24-well plates with cell culture medium. The spheroid-laden hydrogels were maintained in cell culture medium that was exchanged every 72h for a maximum of one week. This was performed for both VUs (spheroids with OEC and CAF/nFib and tumoroids (spheroids with MCF-7 cells and CAF/nFib).

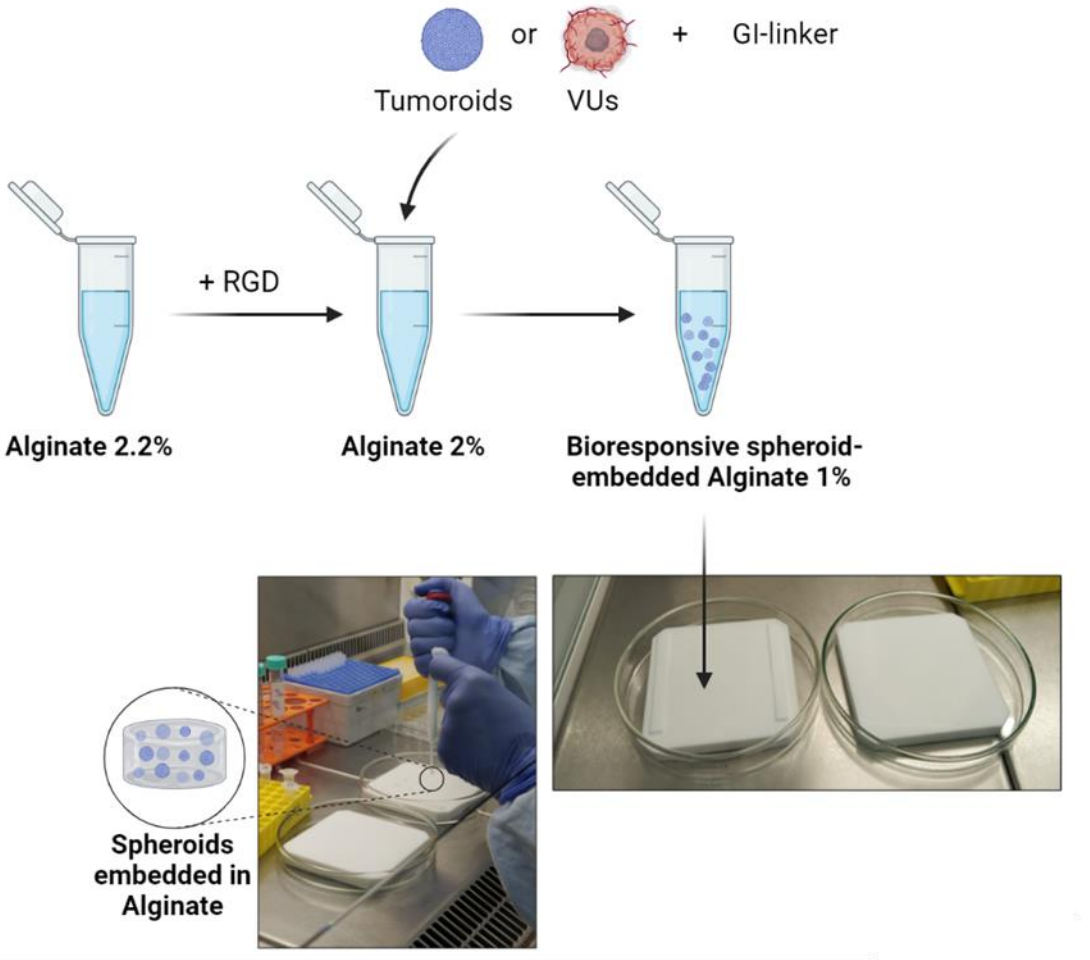

Figure 13 | Schematics of the preparation of spheroid-embedded bioresponsive alginate hydrogels. Micro-drops of the alginate embedded with spheroids were applied on top of a Teflon plate between two spacers and then another Teflon plate was placed on top of those spacers. After 20 minutes of gelation time, alginate 3D matrices were obtained and put in culture.

Immunofluorescence analysis of 3D cocultures in Alginate by CLSM

At different time points, spheroid-laden hydrogels were washed twice with HBSS to remove cell culture medium and fixed with 4% v/v paraformaldehyde (PFA) in HBSS for 20 minutes, at RT. After another washing to remove the PFA, the samples were incubated in blocking buffer (1.5% BSA in HBSS) for 1 hour to minimize non-specific adsorption of antibodies. At the end of that incubation, the blocking buffer was removed. Hydrogels were incubated ON at 4ºC with the following antibodies: phalloidin 488 for F-actin staining (1:100, Flash Phalloidin Green 488), mouse anti-vimentin (1:50, Santa Cruz Sc6260), and UEA1-Rhodamine (1:200, Vector, RL-1062), for the VUs and phalloidin 488 for F-actin staining (1:100, Flash Phalloidin Green 488), mouse anti-vimentin (1:50, Santa Cruz Sc6260) and rabbit anti-E-cadherine (1:100, Cell signaling, 3195), for the tumoroids. On the next day, all samples were washed 3x with HBSS, and incubated with DAPI for nuclei staining (1:500) and the secondary antibodies: Alexa 594 goat anti-rabbit (1:500, A11072) and Alexa Fluor 647 chicken anti-mouse (1:500, A21463), for 1 hour in the dark, at RT. Finally, samples were washed and left at 4ºC with HBSS until imaging. The samples were imaged on a Confocal Laser Scan Microscopy (CLSM, Leica TCS SP5). Data analysis was performed using Fiji Imaging software.

2.11 Microfluidics Fabrication

The microfluidic design was based on the one used by Nashimoto *et al.* as shown in Figure 14 [76]. SolidWorks™ was used to design the molds for the perfusion chips. The molds were 3D printed on a FormLabs™ Form3 Low Force Stereolithography (LFS) 3D printer according to Figure 15.

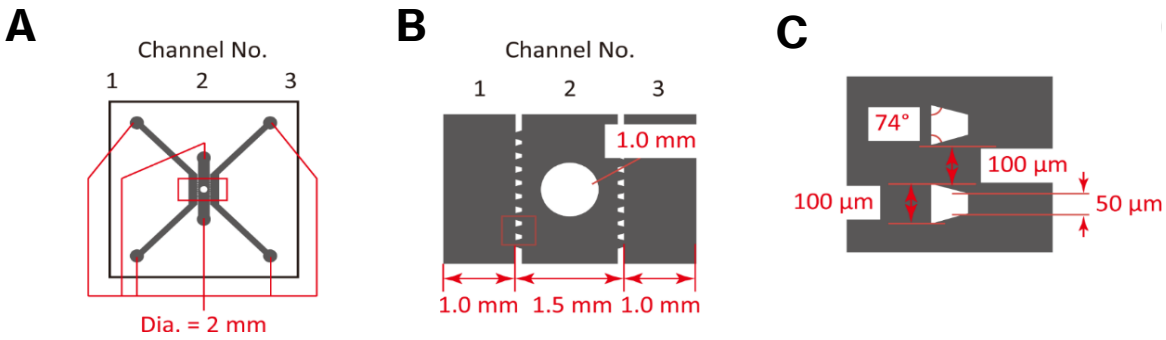

Figure 14 | The original design of the microfluidic device used by Nashimoto *et al*. A) Design overview of the microfluidic device. 2-mm diameter holes were punched on the inlets and outlets of channels 1, 2, and 3, using a biopsy punch and a 1-mm diameter hole was punched on the spheroid well at the center of channel 2. B) The enlarged view of the red rectangle area in (A). C) The enlarged view of the microposts area in the red rectangle in (B).

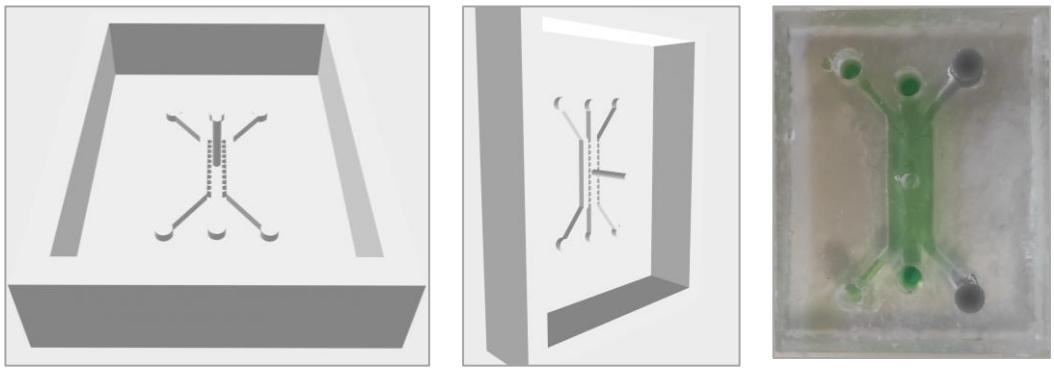

Figure 15 | Microfluidic platform. On the right, green dye was added to check for channel connectivity.

Once printed, the resin mold was washed with isopropanol for 15 minutes, dried in with compressed air, and placed under ultra-violet (UV) light ensure correct polymerization. Then, Polydimethylsiloxane (PDMS) resin and curing agent were thoroughly mixed in a 10:1 ratio and placed in vacuum for 2 hours to remove bubbles. The PDMS was then cast onto the mold and cured for 2 hours at 70°C, with each mold's first 2 casts being discarded to prime the mold.

2.12 Statistical analyses

Statistical analyses were performed using GraphPad Prism 8 software version 8.0.1. Tests to assess normality of the values were performed to assure the correct parametric analyses of the measured values. According to the D'Agostino & Pearson test the numeric values followed a normal distribution. The two-way ANOVA test followed by Tukey's multiple comparisons test were used to compare the different groups of data that followed a parametric distribution. A value of $p \leq 0.05$ was considered statistically significant, assuming a 95% confidence interval. Statistically significant differences are marked with one symbol (* or #) for $p \leq 0.05$, two for $p \leq 0.01$, three for $p \leq 0.001$, or 4 symbols for $p \leq 0.0001$.

Chapter 3 - Results and Discussion

Multicellular tumor spheroids (MCTS) have been one of the tools that have been bridging the gap between *in vitro* 2D studies and *in vivo* studies. Specifically, in cancer research, MCTS can replicate relevant aspects affecting tumor growth, such as biochemical gradients and complex interactions occurring between different cell types. With that in mind, the first step was to characterize monoculture spheroids of MCF-7 cells.

3.1 Characterization of Monoculture MCF-7 Spheroids

The initial experiment consisted in evaluating MCF-7 capacity to form spheroids when cultured in the agarose molds. Although it is described that MCF-7 show high efficiency of spheroid formation, its morphology and stability is dependent on medium formulation, cell density and culture methods [64], [107]. MCF-7 is a breast cancer cell line established in 1973. Cells were isolated from the pleural effusion of a patient with infiltrating ductal carcinoma [108]. This cell line has been propagated for years and has been a model to investigations worldwide. It is a ER-positive, progesterone receptor (PR)-positive and it belongs to the luminal A molecular subtype of breast cancer. This is a non-invasive cell line with low metastatic potential.

To generate the monoculture spheroids, two different molds were used: one that produces large spheroids – mold L - (MicroTissues® 3D Petri Dish® micro-mold 24-35) and other that generates small spheroids – mold S - (MicroTissues® 3D Petri Dish® micro-mold 24-96). Different cell densities were applied in each mold according to Table 4.

Table 4 | Summary of the different spheroid's cell densities.

	1	**2**	**3**
MOLD L	10 000 cells/spheroid	5 000 cells/spheroid	2 500 cells/spheroid
MOLD S	3 645 cells/spheroid	1 822 cells/spheroid	911 cells/spheroid

In all condition, MCF-7 cells started aggregating on day 1 as depicted in Figure 16, and over time, spheroid's circularity seemed to decrease. Day 1 spheroids displayed a smoother and more continuous surface, while on day 7 cell proliferation in the periphery was visible, making the surface more ruffled, as described by Raghavan *et al.* [109].

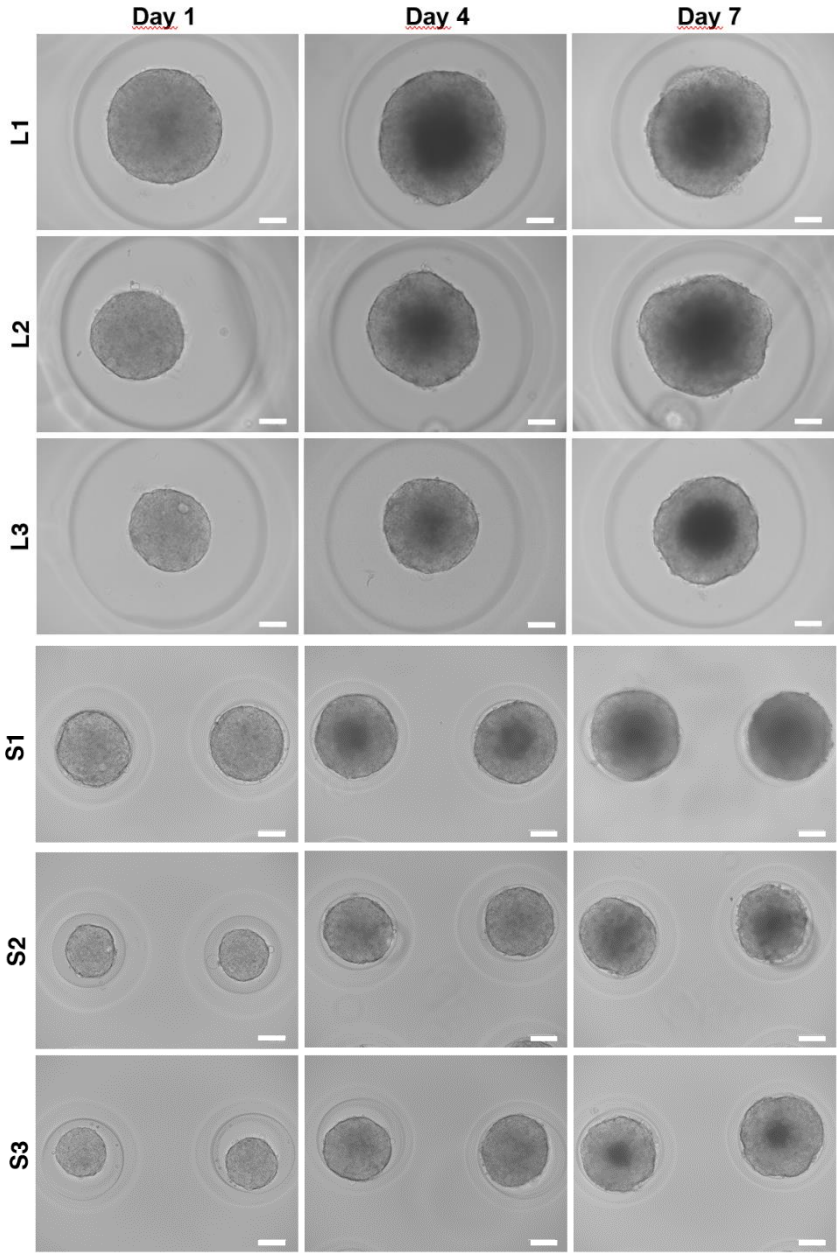

Figure 16 | ZOE™ imaging of MCF-7 spheroids with different cell densities. L – large mold. S – small mold. Numbers 1-3 correspond to the cell densities displayed in Table 4. Scale bars: 100 µm.

The growth kinetics of the spheroids in function of the cell density per well was evaluated over time at days 1, 4 and 7 after seeding and it is represented in Figure 17. Spheroid diameter was dependent on the cell concentration, and it increased over time in every condition, indicating MCF-7 proliferation, as observed by [110]. For the smaller spheroids, on day 1, the presented diameter was 183 ± 13 µm and it increased to 263 ± 15 µm by day 7. The larger spheroids presented a diameter of 469 ± 24 µm on day 1, and it increased to 524 ± 54 µm on day 7.

As previously mentioned, and according to Yakavets *et al.*, large spheroids usually generate molecular gradients (nutrients, O^2, CO^2), so they display a core of necrotic cells, surrounded by a layer of quiescent cells and proliferating cells on the periphery [65]. For the seeding concentrations applied, diameters varied from 180 - 500 µm, thus for the following experiments, cell concentration did not go above 10 000 cells/spheroid.

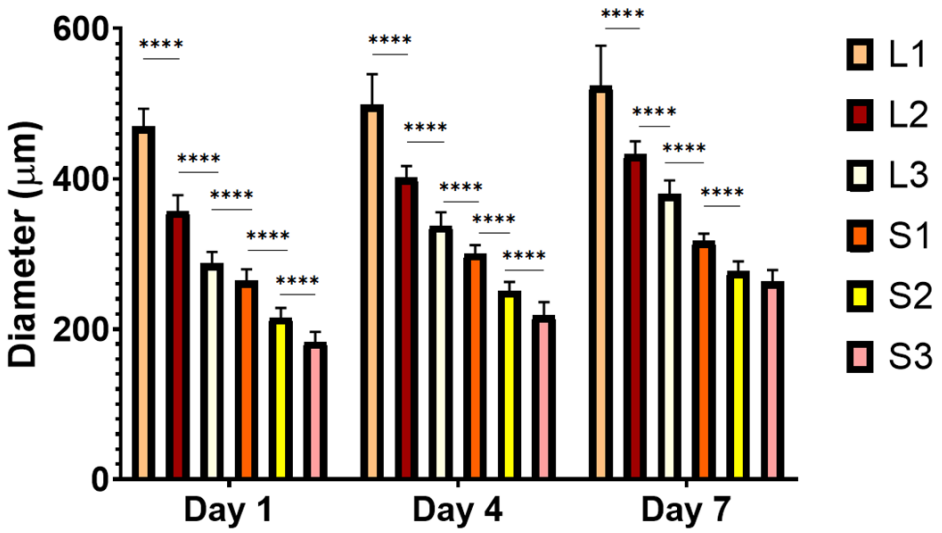

Figure 17 | Growth kinetics of MCF-7 monoculture spheroids. Symbology: * indicates significant differences between different conditions at the same timepoint (n=20).

Agarose is an optimal material for mold fabrication since it is a natural polymer, that is biodegradable and non-toxic for cells [111]. Additionally, it presents the needed characteristics for the generation of spheroids. It is non-adherent, it solidifies at RT, and is optically transparent, so it is convenient for microscopic visualization. The use of agarose molds allowed for a fast cellular assembly that generated spheroids without the need for external forces. The spheroids showed homogenous sizes and growth characteristics, which is important to evaluate the results consistently [63]. This method also demonstrated to be advantageous as a high-throughput technique that enabled the qualitative and quantitative analyses of a single spheroid. Displayed in Figure 18 are some representative images of paraffin-embedded spheroids stained with H&E. These brightfield images were acquired using the *Mosaic* function on the Inverted Fluorescence Microscope Axiovert 200M (Zeiss) and it is possible to visualize all the wells in the agarose molds demonstrating how a single mold that fits in a 24-well plate is able to generate as many as 96 spheroids.

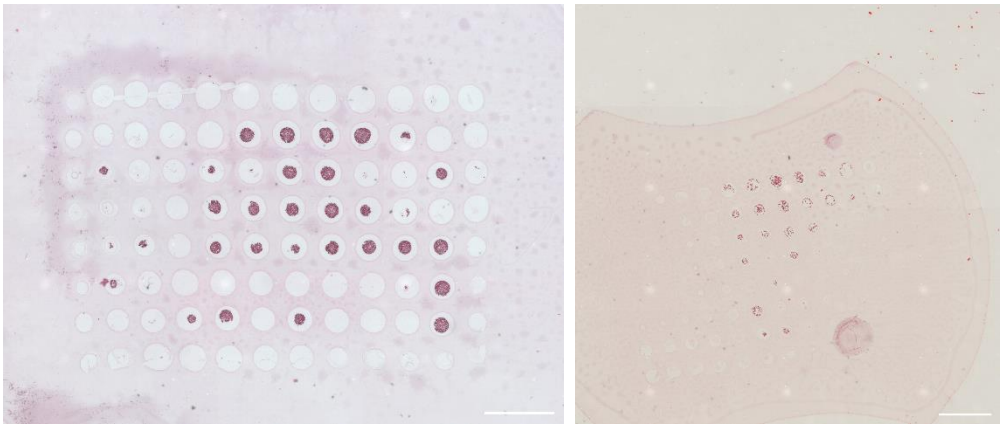

Figure 18 | Brightfield images of paraffin-embedded spheroids stained with H&E in the small agarose molds (24-96). Images were acquired using the *Mosaic* function on the Inverted Fluorescence Microscope Axiovert 200M (Zeiss). Scale bars: 1 cm.

3.2 Generation of Tumoroids

3.2.1 Characterization of CAF *versus* nFib

In breast cancer tissue, fibroblasts constitute a significant component of the surrounding stroma, exerting a modulatory effect on epithelial cells. This effect is dependent upon not only the phenotype of the fibroblasts, but also the epithelial cells themselves. In breast tumors, two types of fibroblasts are commonly found. Normal human mammary fibroblasts (nFib) derive from healthy mammary tissue, and have demonstrated to inhibit epithelial growth, and serve a more protective function [112]. On the other hand, cancer-associated fibroblasts (CAF) likely derive from resident fibroblasts and/or marrow-derived mesenchymal stem cells (MSC), are generally more permissive and may allow/promote growth of the epithelium in a tumor, while also affecting the cell's sensitivity to treatment [113], [114]. In the TME, it is often observed that the majority of normal fibroblasts acquires the CAF phenotype. These fibroblasts exhibit molecular and functional features that are associated with the activated fibroblasts found during wound healing processes, such as high proliferative rate and increased secretion of growth factors [115], [116]. The incorporation of fibroblasts in breast cancer spheroids brings a new component to this 3D model that can now be a more complete representation of the actual tumor.

Envisaging how fibroblasts are such a crucial component in breast tumors, their gene expression profile was first characterized. RNA from both types of fibroblasts was extracted from 2D cultures and analyzed by real-time PCR (qPCR).

Selected genes comprised a group of genes commonly overexpressed in CAF, namely α-SMA, FAP and FSP1 [117]. Vimentin is a mesenchymal marker correlated with EMT in cancer and its expression is also associated with lymph nodes metastasis and overall poor survival rates. This protein is also expressed at higher levels in CAF. Collagen I and fibronectin are proteins found in abundance in the ECM. Their production is usually increased for CAF, which results in matrix stiffening [118]. Lastly, MMP-2 and MMP-14 are matrix metalloproteinases that are known to promote migration and invasion of cancer cells [119]. Results disclosed the expression of all the genes in nFib, and that they were overexpressed in CAF (Figure 19).

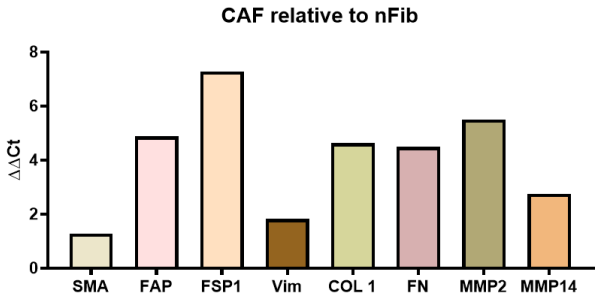

Figure 19 | Relative fold gene expression of key genes commonly expressed by nFib and CAF.

Next experiment consisted of generating monoculture spheroids of nFib and CAF. The large molds were used and a total of 35 000 cells/mold (10 000 cells/spheroid) were added. Spheroids were maintained for a total of 7 days and brightfield images were acquired overtime. On day 1, the two types of spheroids were similar in terms of morphology and size (Figure 20A and Figure 20B). Both form a compact aggregate of cells, rounding 400 µm in diameter. Throughout time, spheroids for both types of fibroblasts decreased in size. However, a significantly higher reduction was observed in nFib-spheroids, reducing to half the initial size (198 ± 24 µm by day 7). The higher diameter observed for CAF-spheroids, is most likely due to the deposition of higher amounts of ECM, such as fibronectin and type I collagen, that act as "glue", generating denser spheroids [120].

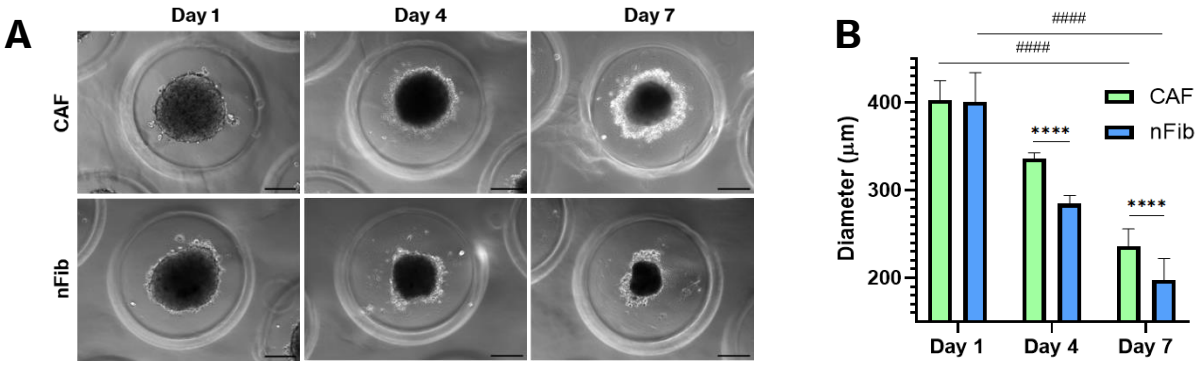

Figure 20 | Characterization of nFib and CAF cultures. A) Brightfield images of monoculture CAF and nFib spheroids at day 1, 4 and 7. Scale bars: 200 µm. B) Diameter measurements of monoculture spheroids overtime (n=20). Symbology: * indicates significant differences between different conditions at the same timepoint, while # indicates significant differences for the same condition at different timepoints.

3.2.2 Incorporation of Fibroblasts in MCF-7 spheroids

Bearing in mind how tumor-stroma interactions play such a vital part in the evolution of breast cancer, MCF-7 cells were combined with fibroblasts to generate coculture spheroids, also further designated by tumoroids.

A first strategy encompassed the generation of MCTS with both CAF and nFib using a **simultaneous seeding approach**. A suspension of MCF-7 and the respective fibroblasts was prepared and added to the small molds, as represented in Figure 21. The seeding concentration was 4 000 cells/spheroid with a 1:1 ratio.

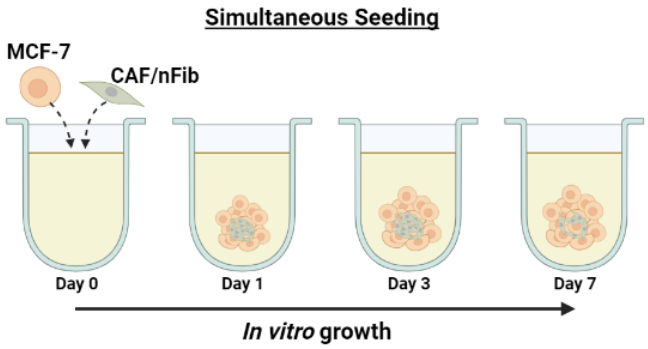

Figure 21 | Schematics of the simultaneous seeding. MCTS assembly by combining MCF-7 and CAF/nFib on the same day.

The samples were then fixed at day 3 and 7 and scaled-up immunohistochemistry was performed for each time-point. Spheroids were immunostained for DAPI to stain DNA; vimentin (Vim), a protein that constitutes the type III intermediate filaments (IF) and that is highly expressed by various types of fibroblasts [121]; fibronectin (FN), a major ECM component that participates in cell adhesion, migration and growth in multiple processes; E-cadherin (E-cad) a key regulator of cell-cell adhesion that is present in the epithelial cell membrane and is in charge of maintaining cell polarity; β-catenin (B-cat) that interacts with E-cad and together play an important role in maintaining epithelial integrity [122].

Confocal images from day 3 (Figure 22A) revealed that fibroblasts (both CAF and nFib; Vim+) were concentrated in the center of the spheroid, while tumor epithelial cells (E-cad+ and B-cat+) lined the periphery. Additionally, fibronectin expression was visible in both types of spheroids, but more prominently in CAF-tumoroids. That can be explained by the fact that CAFs are known to produce a FN-rich matrix that strongly influences cancer cell migration [123], [124]. This is supported by previous results that demonstrated that CAF produce more FN than nFib (Figure 19).

When analyzing confocal images from day 7 (Figure 22B), the spheroids showcased a very low expression of vimentin, indicating a decrease in the number of fibroblasts in the center, while epithelial cells were able to continue proliferating, substantially overgrowing the fibroblasts, as observed by Fang *et al.* [125]. The fast growth of MCF-7 cells leads to a spheroid with a thicker cancer cell layer largely devoid of fibroblasts [72].

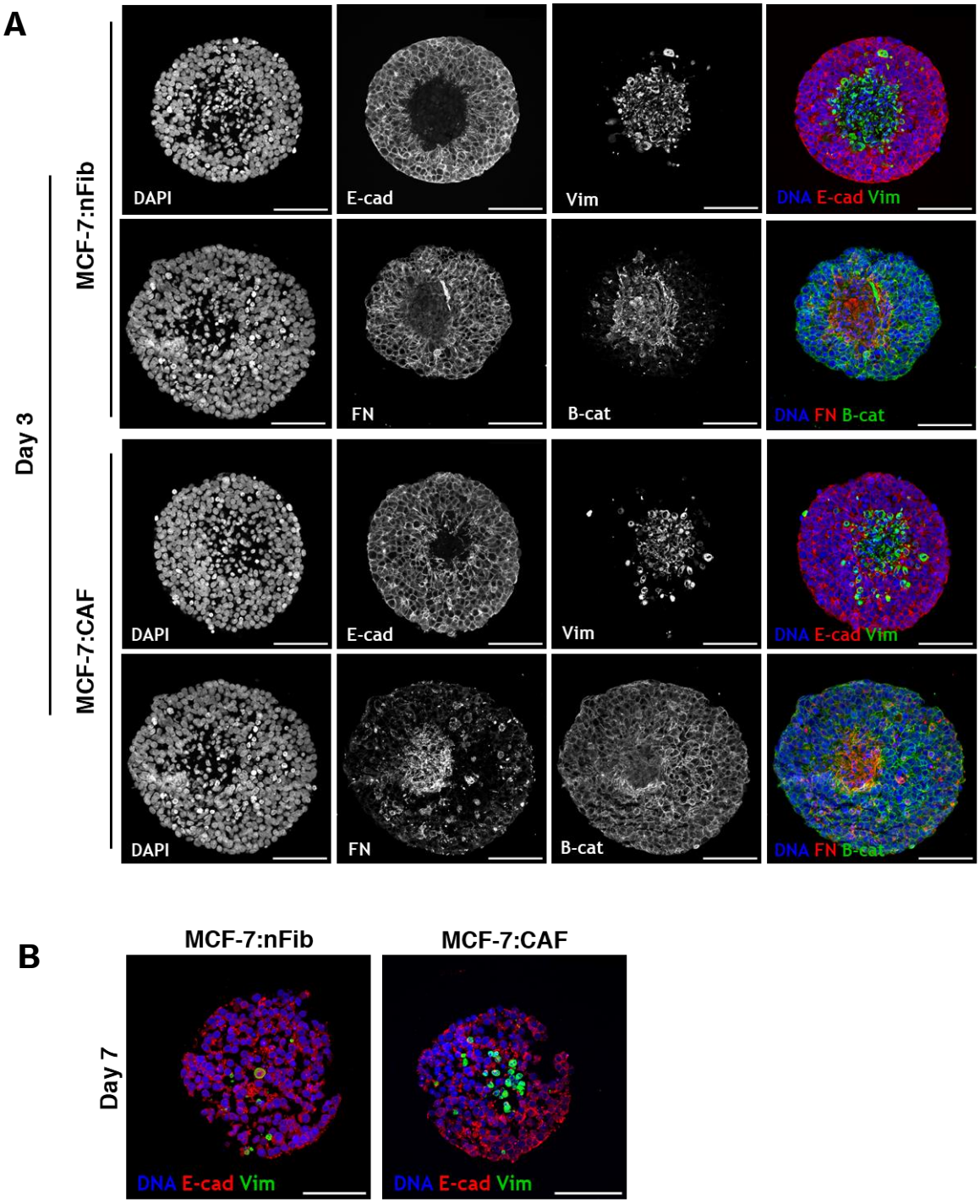

Figure 22 | Characterization of tumoroids generated by simultaneous seeding. CLSM images of tumoroids at day 3 (A) and day 7 (B). Scale bars: 100 µm.

The spatial organization of cells in a tumor is a relevant factor that conditions the TME and affects cell response to certain therapies and anti-cancer drugs. Since these results do not mirror the clinical situation, in which fibroblasts are distributed more uniformly in the tumor, a different experiment was performed, this time using a sequential seeding approach (**sequential seeding after 24h**). Various research groups have tested this cell seeding strategy to try to obtain a different cell organization that prevents the aggregation of fibroblasts in the center of the spheroid [65], [126].

Tumoroids were also generated in the small molds, with the same cell concentration and ratio, however, MCF-7 cells were seeded first in the agarose molds and incubated for 24h, after which, fibroblasts were added (some molds with CAF and others with nFib), as schematized in Figure 23. Samples were fixated with paraformaldehyde and immunostaining was performed.

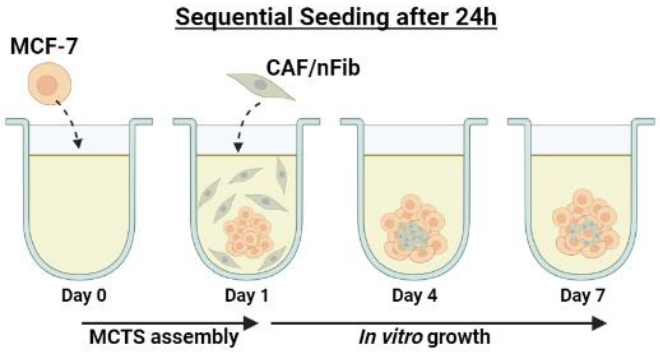

Figure 23 | **Schematics of the sequential seeding after 24h.** MCTS assembly by adding CAF/nFib to MCF-7 spheroids after 24h.

Results revealed that already by day 1 (Figure 24A), some segregation of the two cell types began to happen. E-cadherin was detected in the periphery and vimentin on the core of the spheroid. However, β-catenin was visible throughout the spheroid, which indicated that some tumor epithelial cells remained in the center and had not yet migrated to the outside edge. It is worth noting that the β-catenin marked in the center displayed a more disorganized structure, comparing with the one marked in the outside layer. This suggests that perhaps the two cell types start reorganizing by day 1, which is further supported by day 4 results (Figure 24B). By this time-point, fibroblasts fully separated from epithelial cells and started gathering in the center of the spheroid. Nevertheless, when

comparing the area occupied by fibroblasts in each type of seeding (simultaneous versus sequential after 24h) at day 4, it was possible to observe that in the sequential experiment, fibroblasts took a bigger area of the spheroid. By day 7 (Figure 24C), vimentin expression had decreased and there were very few fibroblasts (nFib or CAF) left in the spheroid. In both seeding strategies, it was possible to observe that CAFs remained present longer than nFib, as vimentin expression was higher for those spheroids by day 7. This is explained by the high proliferative nature of CAF, that can control and shape the surrounding matrix, possibly contributing to their survival [127].

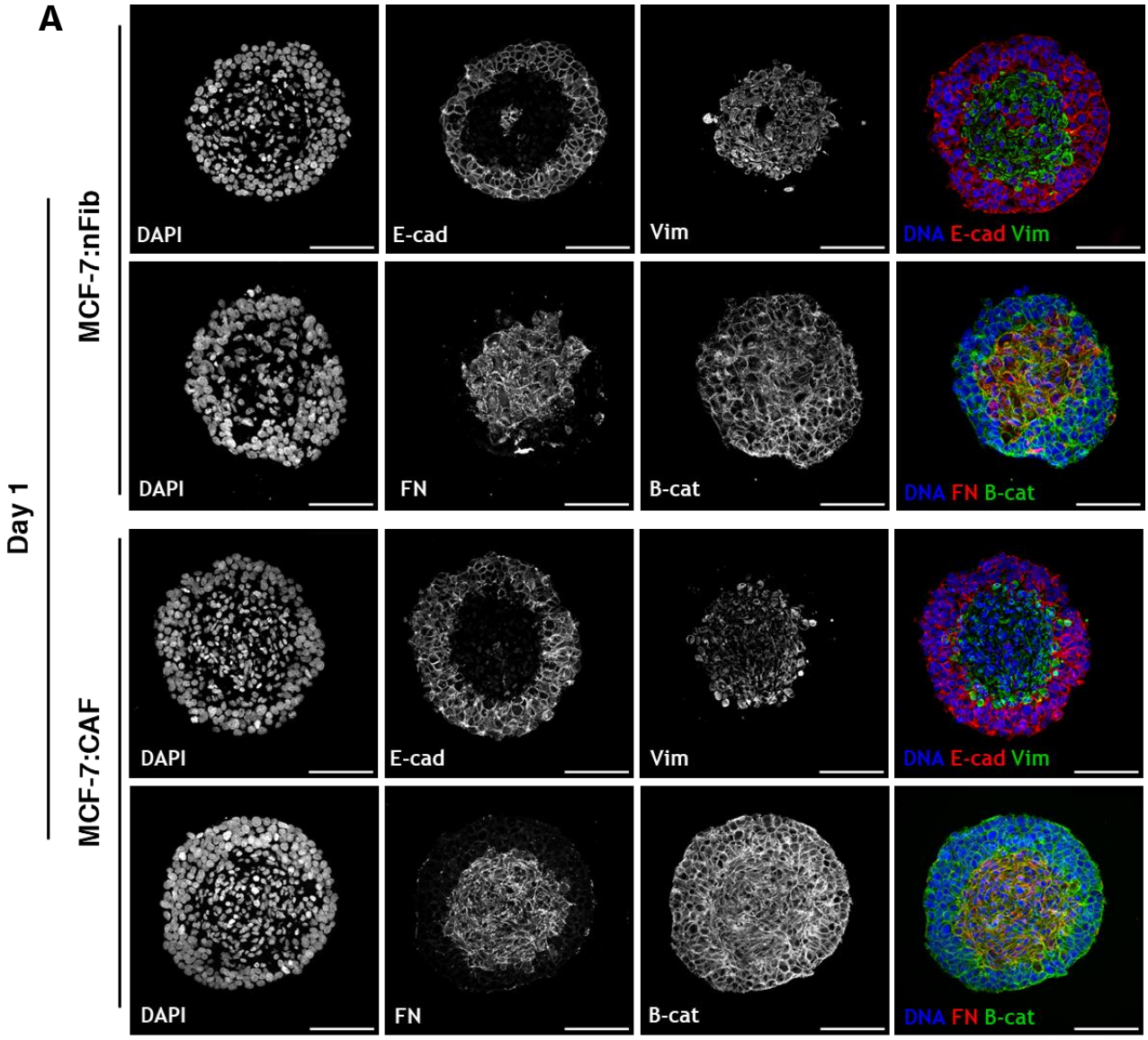

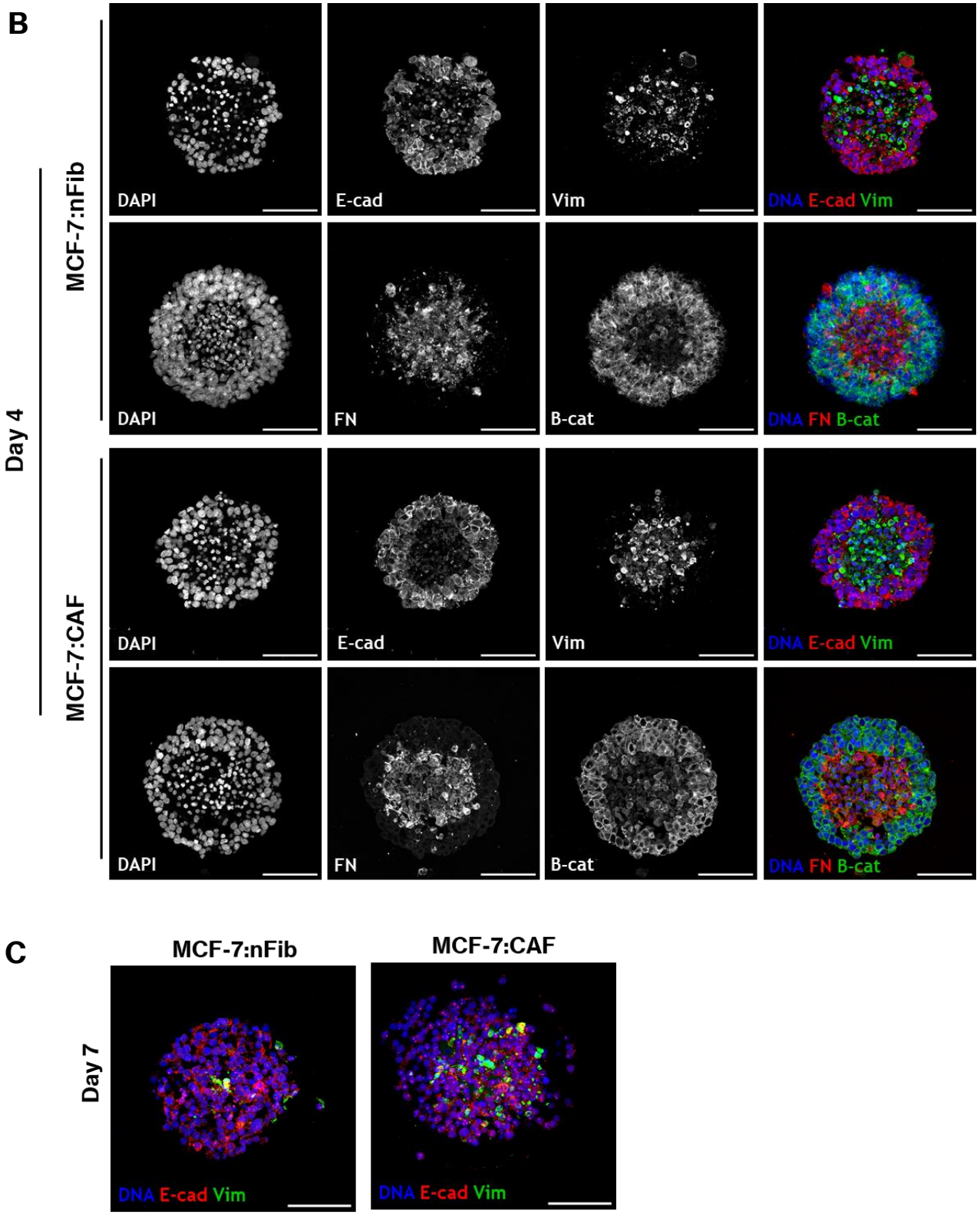

Figure 24 | Characterization of tumoroids generated by sequential seeding after 24h. CLSM images of tumoroids at day 1 (A), day 4 (B) and day 7 (C). Scale bars: 100 µm.

To generate spheroids that more closely recapitulate the spatial distribution of cells found in the *in vivo* breast tumor a third strategy was attempted. It consisted in a sequential seeding, but this time, fibroblasts (CAF or nFib) were added on the 6th day of culture (**sequential seeding after 6 days**), after MCF-7 cells had previously self-aggregated and formed a more maturated mass (Figure 25). This approach had already been performed by other research groups to try to achieve a more stratified cell organization found in the pancreatic ductal adenocarcinoma, where fibroblasts are organized in the periphery of the spheroid and tumor cells in the center [126]. In this strategy, spheroids had a total of 10 000 cells and coculture spheroids were generated with two different ratios: 1:1 and 1:4 (MCF-7:CAF/nFib). The ratio 1:4 was based on the knowledge that CAF not only make up the bulk of cancer stroma, but also may represent up to 70% of the whole breast tumor volume [128].

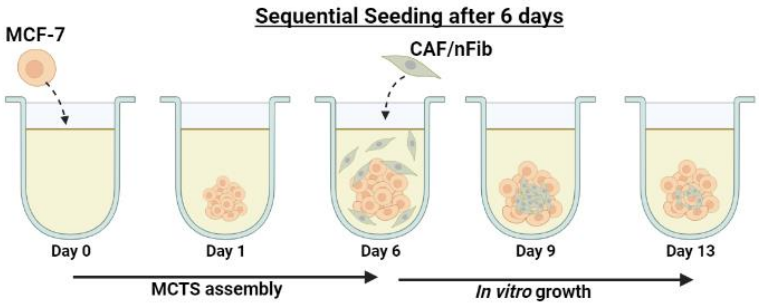

Figure 25 | Schematics of the sequential seeding after 6 days. MCTS assembly by adding CAF/nFib to 6 days MCF-7 spheroids.

The first stage of this approach consisted in the initial assembly of MCF-7 spheroids. These were cultured for 6 days, and medium was changed every other day. By day 6, MCF-7 spheroids had formed a core of compacted cells for both conditions 1:1 and 1:4 (Figure 26). The initial aggregation of MCF-7 is initiated by integrin-mediated attachment to ECM molecules, and the cells are aggregated compactly by E-cadherin mediation [64]. The optical micrographs showed an opaque and chaotic area after 6 days of culture, which have already been observed by Fang G *et al.* in larger spheroids of MCF-7 compared to smaller spheroids (initial diameter below 100 µm) [125].

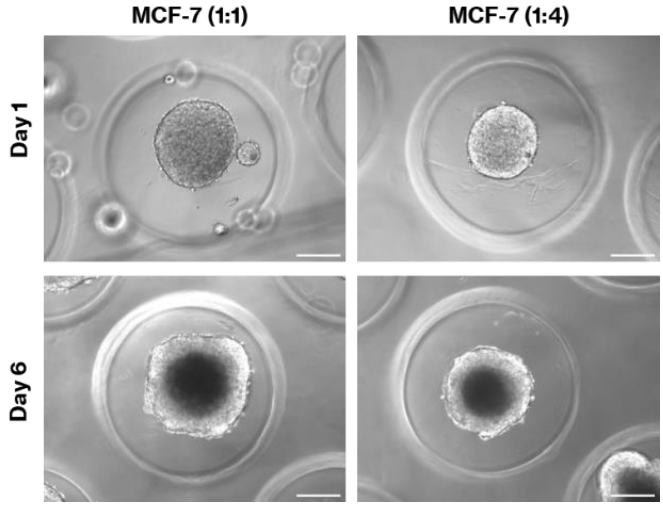

Figure 26 | Brightfield images of the monoculture MCF-7 spheroids from day 1 and 6. The 1:1 ratio had a total of 5 000 cells, while the 1:4 ratio had 2 000 cells. Scale bars: 200 µm.

The second stage happened at day 6, with the addition of fibroblasts to the agarose molds. After 24h, the spheroids remained compact demonstrating that fibroblasts could establish close interactions between them and with the tumor cells. This also indicated a successful inclusion of both cell types (Figure 27A). The homogenous periphery of the spheroids persisted until day 7.

Tumoroids' diameters were measured at days 1, 3 and 7 (Figure 27B). Throughout the different time-points, tumoroids generated with the ratio 1:4 presented a smaller diameter in comparison with the 1:1 condition. Moreover, 1:1 tumoroids diameter increased over time, while that was not observed for the 1:4 tumoroids. This can be attributed to the higher number of fibroblasts (either nFib or CAF) in the 1:4 ratio, that by producing larger amounts of ECM lead to the formation of more compact spheroids. When comparing 1:4 CAF-tumoroids with 1:4 nFib-tumoroids, it was verified that the ones with CAF presented smaller diameters through all the timepoints (493 ± 29 µm *versus* 538 ± 42 µm, on day 1). CAF are known to produce more ECM, while also having a stronger role in its remodeling. This remodeling feature is also related to contractility of CAF, which is deeply related to their ability to induce cancer cells migration and invasion. CAF can promote matrix stiffening, which in turn, activates molecular mechanisms that cause changes in the contractile actin cytoskeleton of fibroblasts and that are related to invasion

of cancer cells [129], [130]. The ability of CAF to stiffen the matrix and contract explains the smaller diameter observed for CAF-containing spheroids. Additionally, assessment of metabolic activity revealed a high metabolic activity for all the tumoroids, which increased throughout time (Figure 27C).

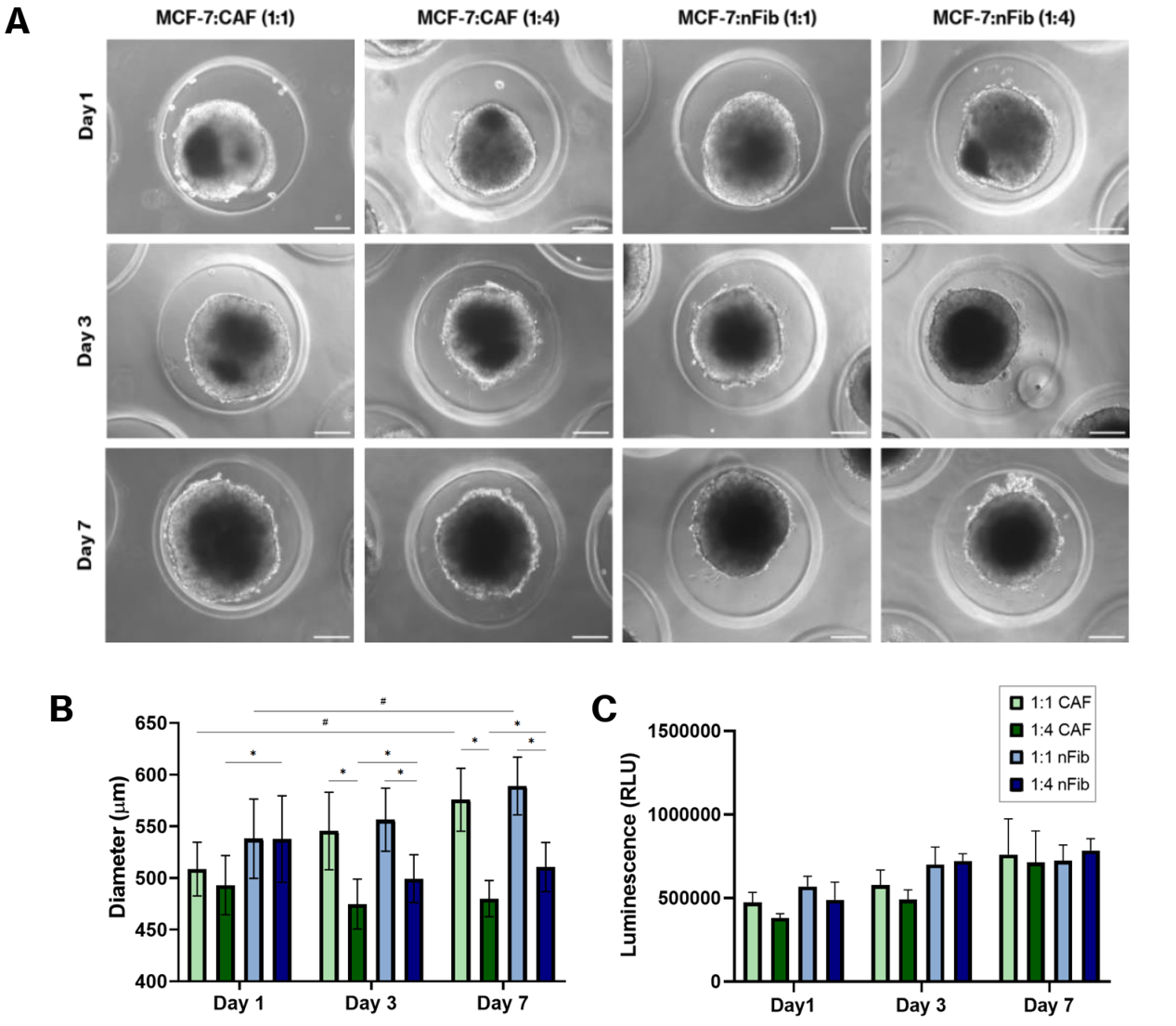

Figure 27 | Characterization of tumoroids generated by sequential seeding after 6 days. A) Brightfield images were acquired at days 1, 3 and 7. Scale bars: 200 µm. B) Tumoroids diameter measurements from day 1, 3 and 7 (n=20). C) Metabolic activity assessment overtime (n=3). Symbology: * indicates significant differences between different conditions at the same timepoint, while # indicates significant differences for the same condition at different timepoints.

Afterwards, immunohistochemical analysis of the tumoroids was performed and confocal images revealed different organization of cells by day 1. For all four conditions, distinct groups of cells seemed to form within the spheroid (Figure 28). The groups were constituted by aggregates of cells marked with vimentin (green), that correspond to fibroblasts, surrounded by epithelial tumor cells marked with E-cadherin (red). Comparing with the two previous seeding methods, this one allowed for fibroblasts to take up a bigger area of the spheroid. At day 1, it was possible to see that fibroblast (both CAF and nFib) formed compact aggregates that clearly segregated from epithelial cells and created very defined spaces within the spheroid (Figure 28). Curiously, an area of cells only marked with DAPI (not with vimentin nor E-cadherin) was present in all the conditions. This group of cells possibly corresponds to cells from the initial MCF-7 spheroid that eventually died and stopped producing E-cadherin. This is supported by the H&E-stained spheroids (Figure 29) that also showcased an area populated with cells with necrotic nuclei. An article by Froehlich *et al.* also reports that MCF-7 monoculture spheroids exhibited a disintegrating core after 48h in culture. This core was Ki-67 (proliferation marker) negative and cPARP (apoptosis marker) positive [131].

After one week, fibroblasts still occupied a considerable area of the spheroid and were not completely overgrown by the highly proliferative epithelial cells. This was more evident for the CAF-spheroids, especially for the 1:4 ratio, once more fibroblasts are present in this condition (Figure 28B). Another particular aspect found in this approach was that, by day 7, the conditions with a higher number of fibroblasts (1:4) presented a wheel-like morphology with branches of epithelial cells (E-cad+) followed sequentially by empty spaces (Figure 28B and Figure 28D).

Overall, in all seeding approaches fibroblasts have a tendency to go to the center of the spheroid. This central tendency of fibroblasts could be due to the different cohesion of the two cells as also hypothesized by Fang *et al.* [125]. Additionally, it has been reported that hypoxia could attract the migration of fibroblasts into the tumor microenvironment, which could be another reason for the core–shell structure [132], [133]. Numerous articles report the strong ability of CAF to remodel the ECM (which includes deposition of new components, matrix expanding, crosslinking, and stiffening), introducing a stiffness heterogeneity [115]. Tumor cells could then take advantage of this heterogeneity to either

migrate between looser fibers or use aligned fibers as directional cues that pave the way for their migration [114].

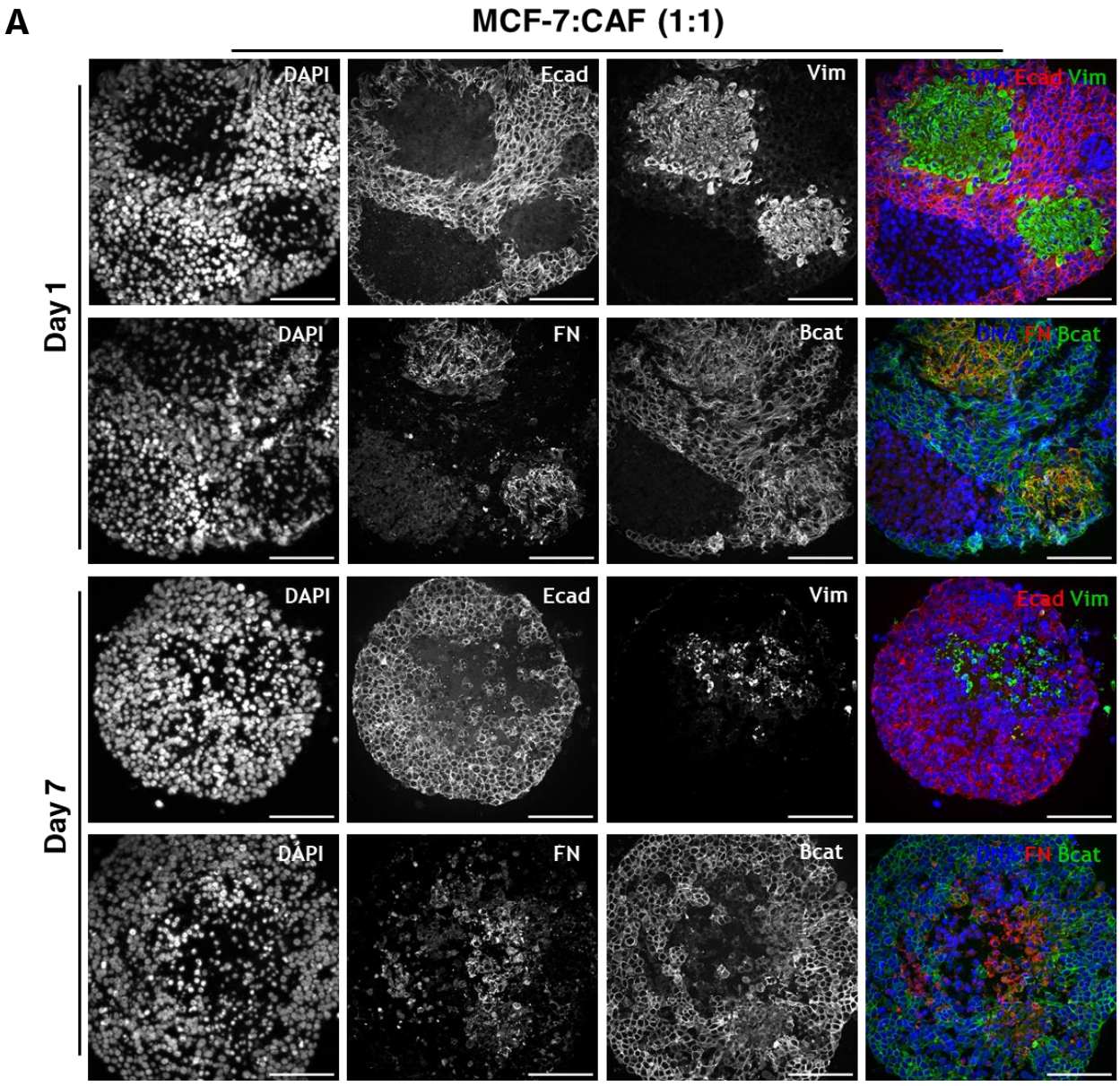

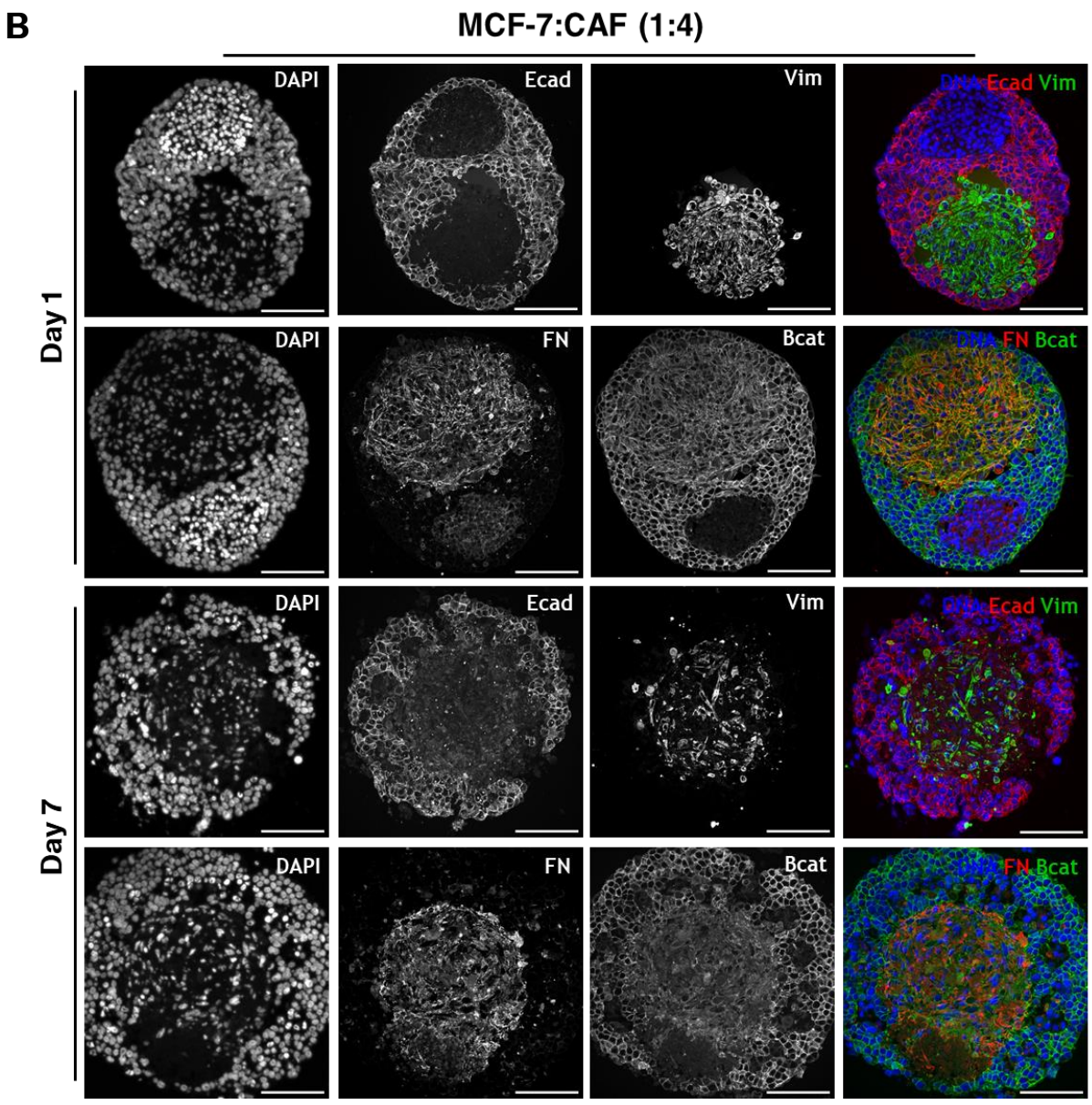
B
MCF-7:CAF (1:4)
Day 1
Day 7
DAPI
Ecad
Vim
DNA Ecad Vim
DAPI
FN
Bcat
DNA FN Bcat
DAPI
Ecad
Vim
DNA Ecad Vim
DAPI
FN
Bcat
DNA FN Bcat

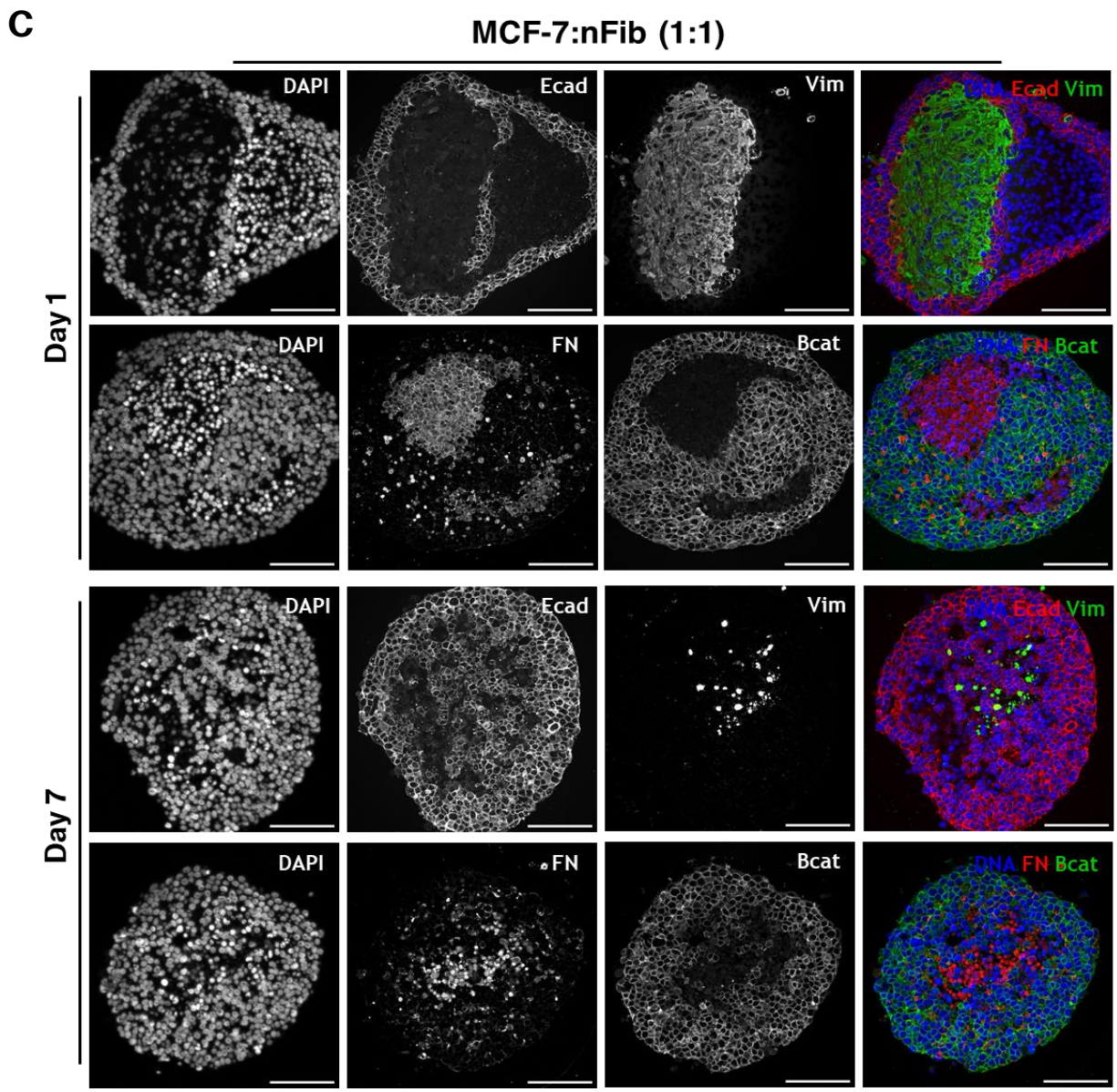
C
MCF-7:nFib (1:1)
Day 1
Day 7
DAPI
Ecad
Vim
DNA Ecad Vim
DAPI
FN
Bcat
DNA FN Bcat
DAPI
Ecad
Vim
DNA Ecad Vim
DAPI
FN
Bcat
DNA FN Bcat

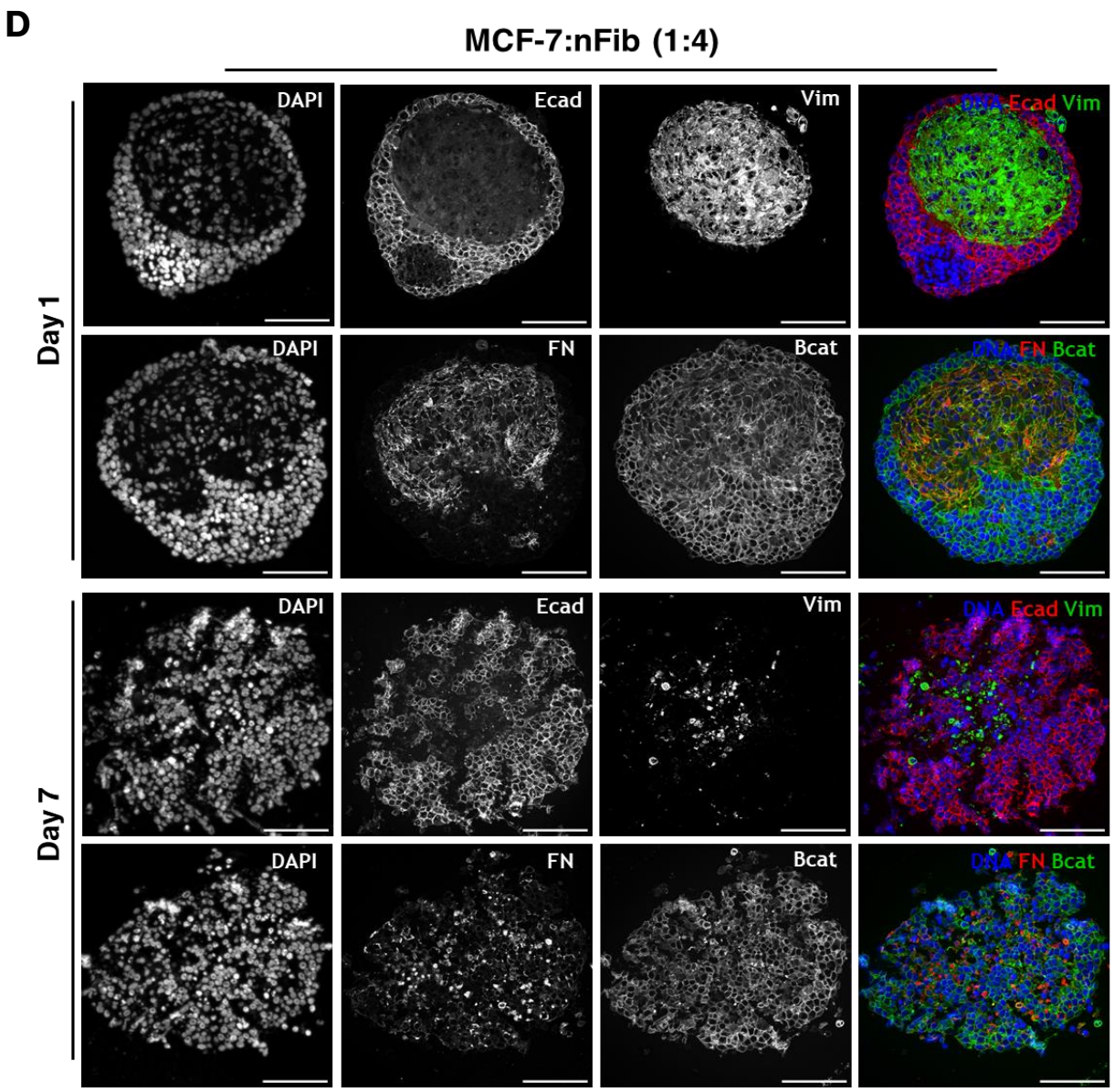

Figure 28 | CSLM images of tumoroids generated by <u>sequential seeding after 6 days</u>. Images acquired at day 1 and day 7. Tumoroids were generated using four different settings: MCF-7 and CAF with a 1:1 (A) and 1:4 (B) ratio; and MCF-7 and nFib also with a 1:1 (C) and 1:4 (D) ratio. Scale bars: 100 µm.

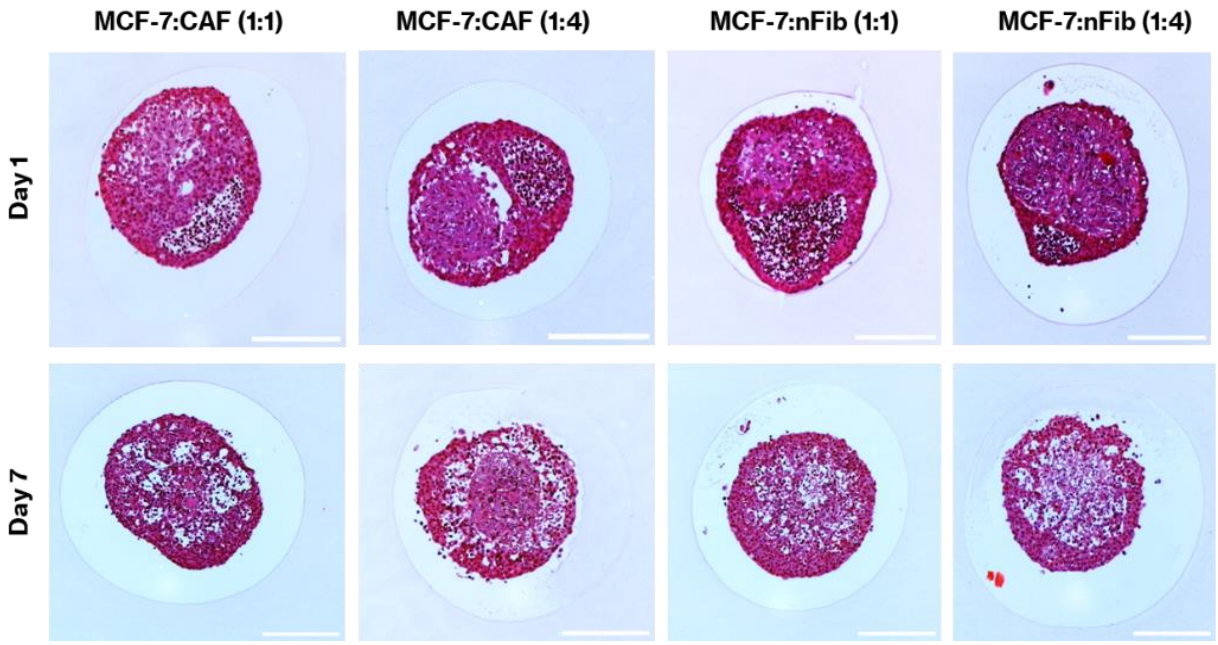

Figure 29 | Brightfield images of H&E-stained sections of the different tumoroids overtime. Scale bars: 200 µm.

3.3 Generation of Vascular Units

Outgrowth endothelial cells (OEC), also called late endothelial progenitor cells, can be isolated from the peripheral blood as well as the human cord blood [134]. They can also be isolated from other sources such as porcine, murine, and canine. When cultured in a commercially available cell culture medium, they form colonies that present a cobble stone-like morphology. Additionally, OEC show several similarities with endothelial cells in terms of cellular markers and functional properties. Marker profile is characterized by the presence of CD31+ cells that already loss the hematopoietic marker CD45. These cells present high proliferation and angiogenic potential *in vitro* and can contribute to neo angiogenesis *in vivo*. For these reasons, OECs have been applied extensively in multiple applications involving the generation of vascular networks whether it is within scaffolds or tissue constructs [135], [136]. Moreover, several reports have stated that fibroblasts play

an important role in the formation of sprouts since they act as mural cells, supporting the formation of tube-like structures [84]. Hence, OEC, CAF and nFib were used to assemble the vascular units (VUs) model.

3.3.1 VUs Morphology and Characterization

The first experiment consisted of a screening of conditions to assess the most suitable one that originated the most uniform VUs. Hence, VUs with different ratios: 1:1, 1:5 and 5:1 using either CAF or nFib (OEC:CAF/nFib) were formed in non-adhesive microwells and monitored along 14 days.

When analyzing the brightfield images for the VUs formed with CAF (**CAF-VUs**), they showed the formation of round spheroids for all the ratios, however, some variations with morphology were observed (Figure 30A). At day 3, the average diameters of spheroids with different OEC:CAF ratios were 292 ± 30 μm (1:1), 326 ± 41 μm (5:1) and 287 ± 19 μm (1:5) (Figure 30B). The ratio with lower amount of fibroblast (5:1 ratio) displayed a significantly larger size with a thicker periphery of loose cells. Throughout time, spheroid maturation was observed, and it was accompanied by a gradual release of cells. This phenomenon was more evident in the ratio 5:1, with a significant increase of the spheroid diameter (reaching 363 ± 29 μm on day 7). At day 7, a separation of two groups of cells could be observed for the three conditions. One group consisted in a more circular, denser group of cells likely corresponding to the fibroblasts and a less compact group possibly formed by endothelial cells. In the work of Carvalho *et al.*, they also observed a similar behavior and identified that the majority of cells that were being released were endothelial cells [120]. This could explain why the ratio with less endothelial cells (1:5 ratio) presented a more compact and homogenous morphology with less cells being released. Spheroids from this ratio presented the smallest diameter at day 7: 242 ± 24 μm.

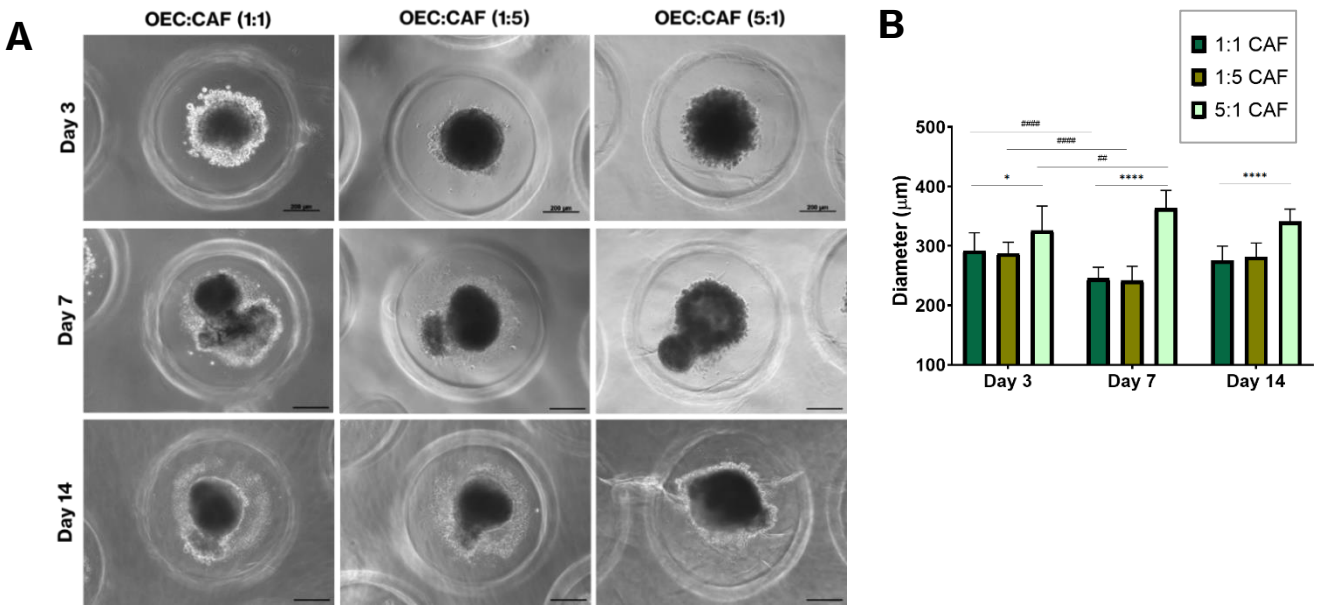

Figure 30 | VUs generated with OEC and CAF with the ratios 1:1, 1:5 and 5:1. A) Brightfield images were obtained at days 3, 7 and 14. Scale bars: 200 µm. B) VUs diameter measurements from day 3, 7 and 14. Symbology: * indicates significant differences between different conditions on the same timepoint, while # indicates significant differences for the same condition in different timepoints (n=20).

Brightfield images for **nFib-VUs** showed similar results, with 1:5 condition exhibiting the most homogenous and compact spheroids (with a diameter of 294 ± 12 µm at day 3 that decreased to 235 ± 23 µm until day 7), and also with the lowest number of dispersed cells on the outer layer (Figure 31A).

At day 3, spheroid size rounded the 300 µm, as observed with CAF-VUs, and the biggest diameter obtained was with the condition 5:1 (335 ± 34 µm) (Figure 31B). For all the conditions, spheroids shrinked from day 3 to day 14, but that was less significant for the 5:1 ratio (a decrease of about 60-70 µm for conditions 1:1 and 1:5 and about 30 µm for 5:1), which was possibly due to the fewer fibroblasts present in the spheroid. Interestingly, on day 7, 1:1 nFib-VUs were smaller than 1:5 albeit they contained less fibroblasts. This phenomenon, that can also be observed in Figure 31A, can perhaps be ascribed to the fact that more cells were found outside the spheroid in the 1:1 condition, when comparing to the 1:5 ratio. The latter displayed a spheroid with less cells surrounding the spheroid, which possibly indicates a better incorporation of the two cell types, ultimately forming a bigger spheroid with a bigger number of aggregated cells.

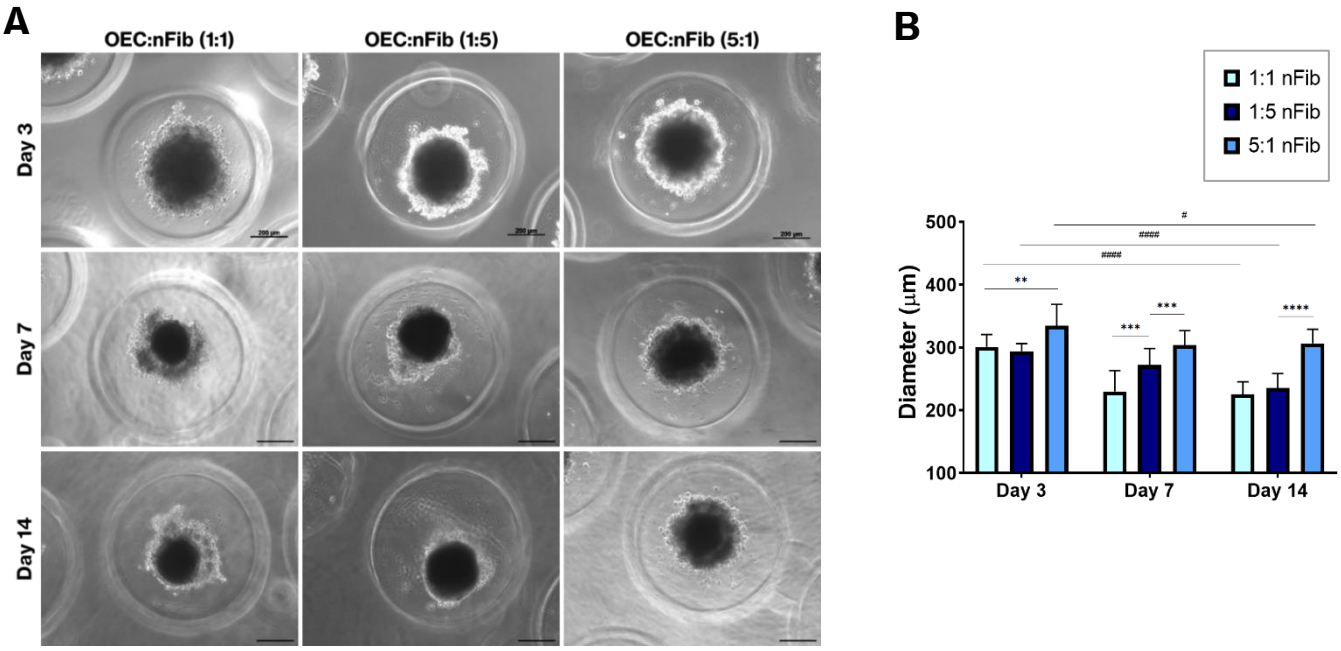

Figure 31 | VUs generated with OEC and nFib with the ratios 1:1, 1:5 and 5:1. A) Brightfield images were obtained at days 3, 7 and 14. Scale bars: 200 µm. B) VUs diameter measurements overtime. Symbology: * indicates significant differences between different conditions on the same timepoint, while # indicates significant differences for the same condition in different timepoints (n=20).

Following experiments were designed to further explore VUs characteristics comparing CAF *versus* nFib, and regarding their cellular organization and sprouting potential. Thus, VUs were once again generated, but this time using only the 1:5 ratio that

exhibited the most promising results in terms of homogeneity (Figure 32A). Moreover, in previous work of our group it was also observed that this 1:5 ratio (OEC: dermal fibroblast) formed compact spherical structures within 24 hours and this structure was preserved for extend culture periods [135].

Overall, CAF-VUs were more uniform forming more compact spheroids and with low cell release. They also had smaller diameters that decreased over time: 365 ± 26 μm to 292 ± 45 μm for CAF-VUs in comparison with nFib-VUs: 436 ± 30 μm to 312 ± 25 μm (Figure 32B). This was expected, once again, due to the highly contractile nature of CAFs [123]. Both VUs presented a high viability (Figure 32C) and metabolic activity (Figure 32D).

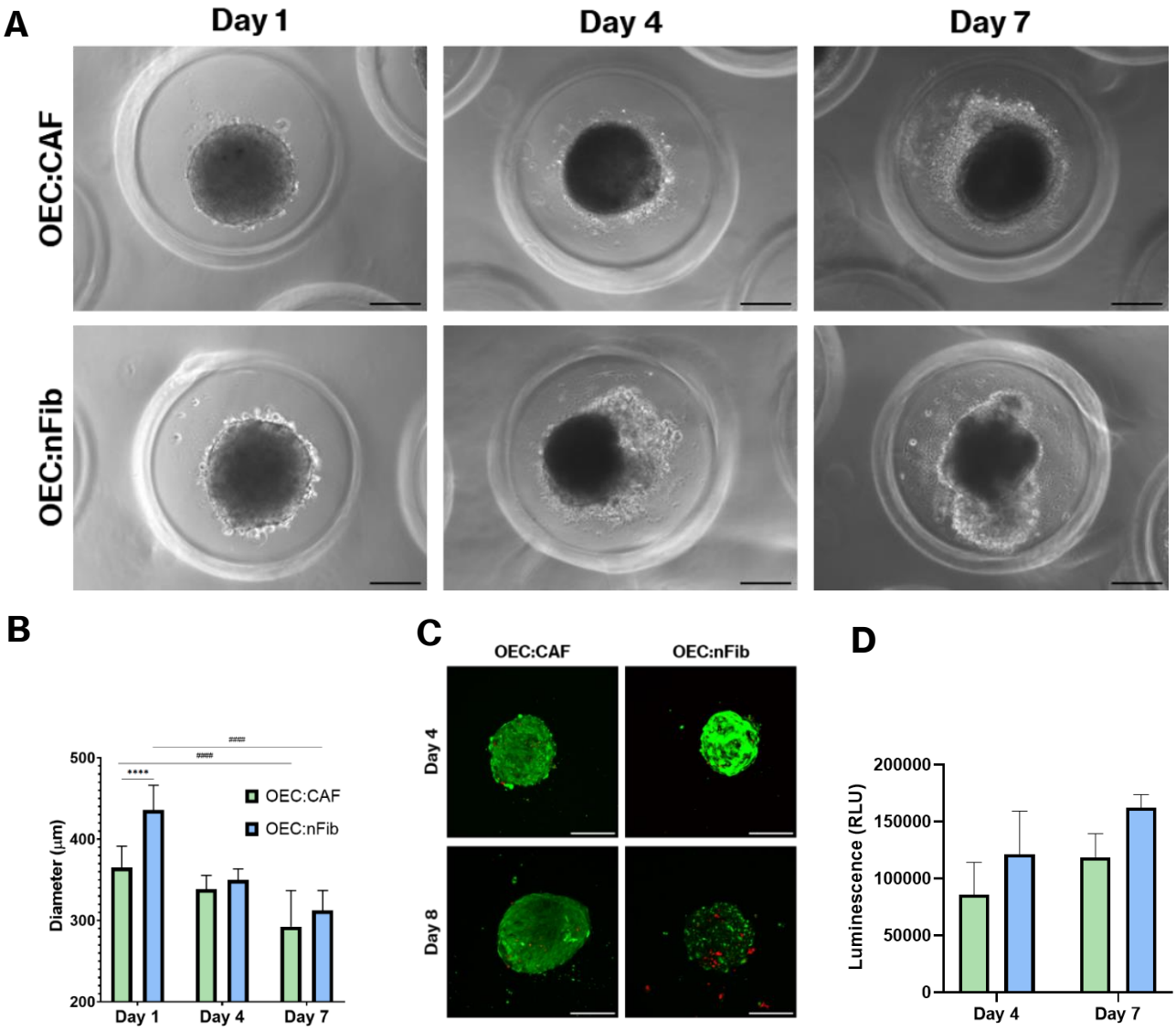

Figure 32 | VUs (1:5) generated with OEC and CAF/nFib. A) Brightfield images were obtained at days 1, 4 and 7. Scale bars: 200 µm. B) VUs diameter measurements overtime (n=20). C) Live/Dead assay: CLSM images of VUs at day 4 and 8 of culture. Live cells were stained for calcein AM (green) and dead cells by ethidium homodimer-1 (red). Scale bars: 200 µm. D) Metabolic activity assessment overtime (n=3). Symbology: * indicates significant differences between different conditions on the same timepoint, while # indicates significant differences for the same condition in different timepoints.

Next, VUs were processed still within the agarose mold and spheroid sections were subject to immunohistochemical analysis. Cells were immunostained for specific endothelial markers CD31 and von Willebrand Factor (vWF). CD31 is a transmembrane glycoprotein expressed by endothelial cells [137]. vWF is a glycoprotein required for regular hemostasis and that is produced by endothelial cells [138]. Other markers applied were vimentin (Vim), that labelled fibroblasts, while the production of ECM was detected by fibronectin (FN).

Results revealed the organization of an outer monolayer of OECs (CD31+ and vWF+ cells) surrounding fibroblasts (Vim+ cells) that were present in the spheroid's core, for both types of VUs at day 1 (Figure 33A). Cells rapidly (day 1) segregated into an OEC surface monolayer, enclosing an fibroblast-enriched core as described previously [120], [135]. For CAF-VUs it was possible to observe some rudimental vascular networks forming in the core of the spheroids at day 1, that further developed and matured till day 7 (Figure 33A, yellow arrows). On the other hand, nFib-VUs displayed a less organized architecture by day 7 and an unclear layer of OEC in the periphery (Figure 33B). Additionally, vascular structures could not be observed. The production and accumulation of ECM is important during spheroid formation and maturation, allowing cell-matrix interactions and guiding cell organization [139]. Therefore, the expression of higher amounts of ECM proteins, namely FN and Col I by CAF, could enhance endothelial cell organization.

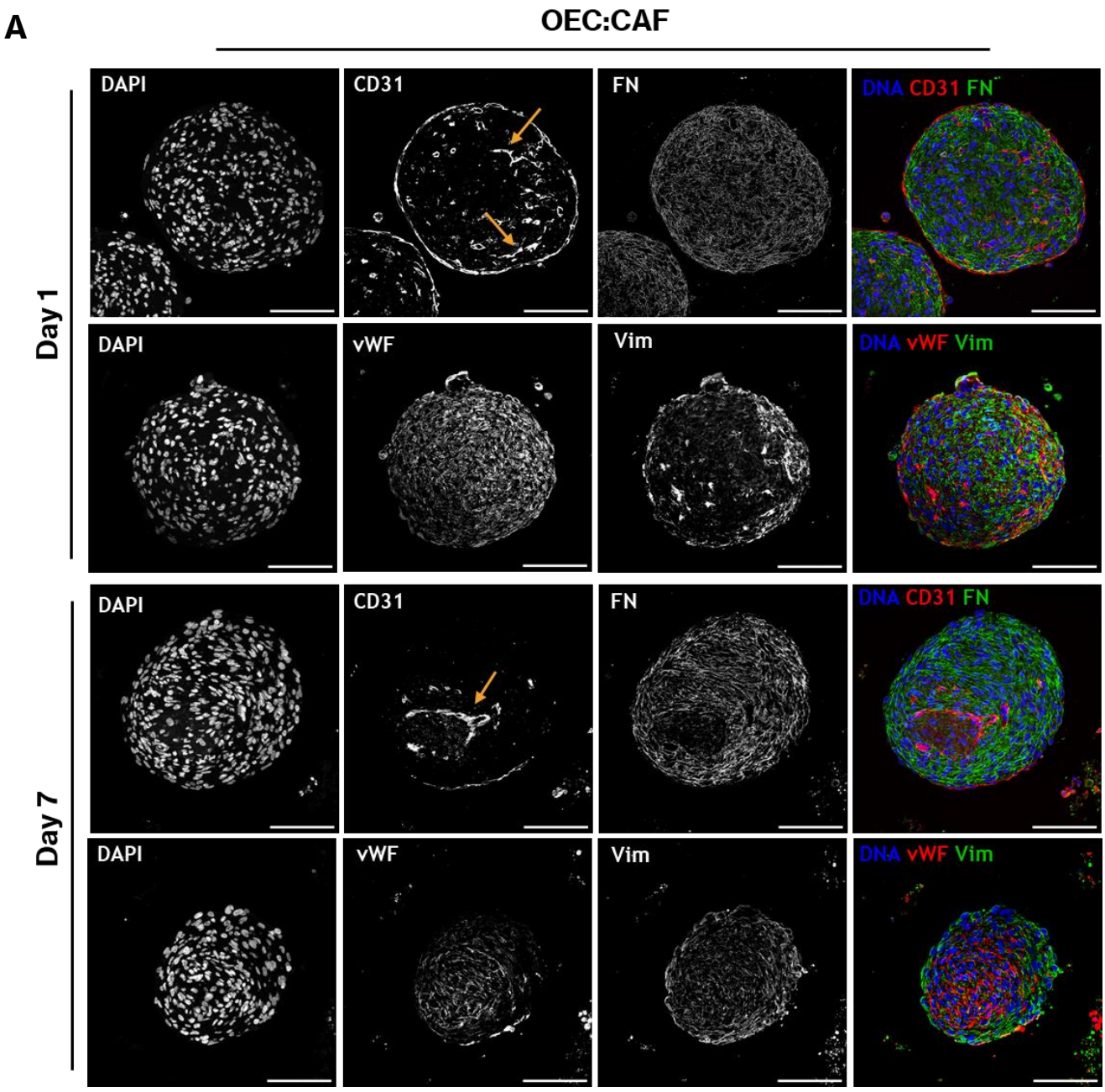
A
OEC:CAF
Day 1
Day 7
DAPI
CD31
FN
DNA CD31 FN
DAPI
vWF
Vim
DNA vWF Vim
DAPI
CD31
FN
DNA CD31 FN
DAPI
vWF
Vim
DNA vWF Vim

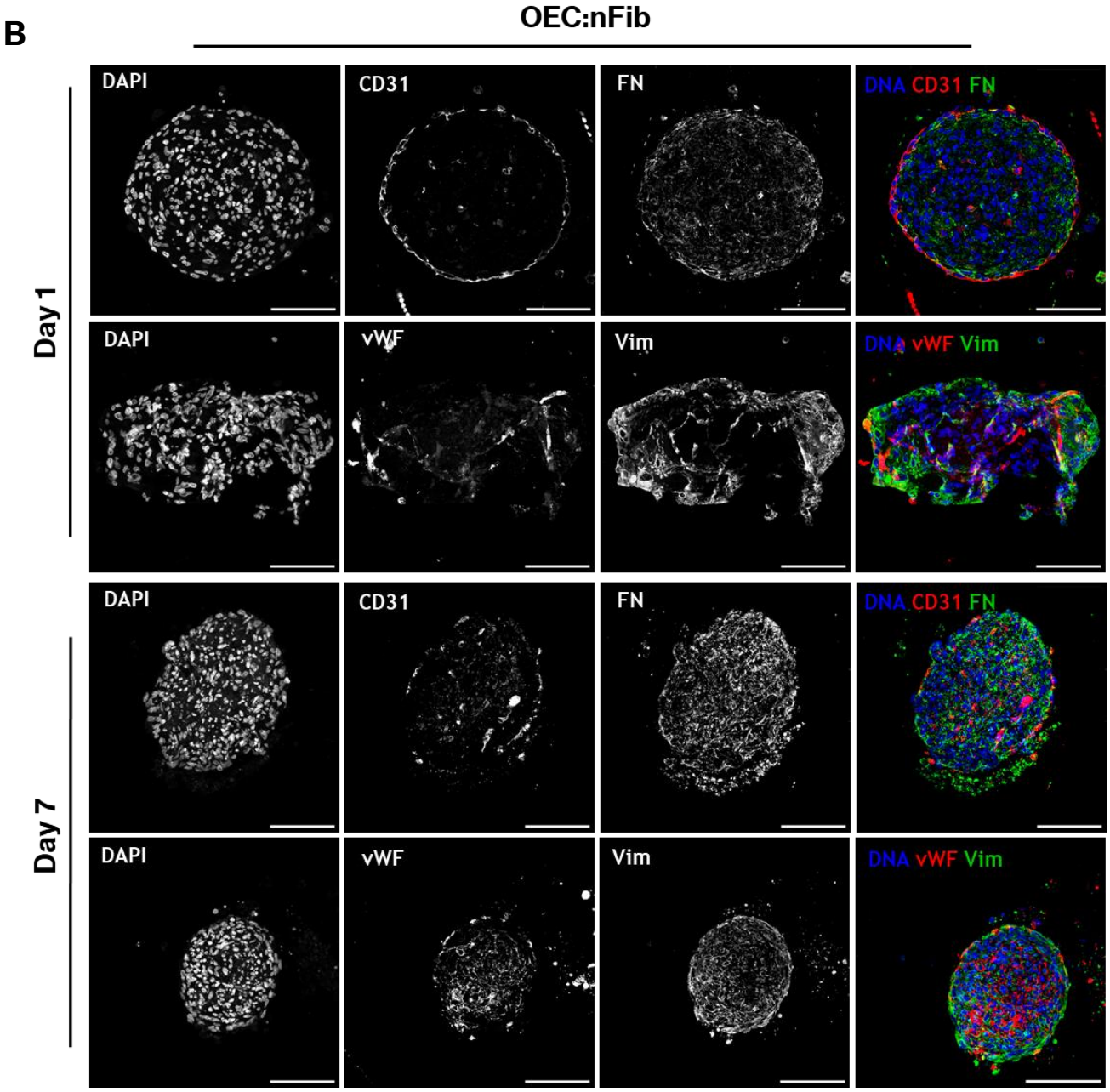

Figure 33 | Representative CLSM images of VUs morphology after 1 and 7 days of culture. A) Coculture spheroids with OEC and CAF (CAF-VUs); yellow arrows indicate organized OEC structures in the spheroid's core. B) Coculture spheroids with OEC and nFib (nFib-VUs). Cells were stained for DAPI (blue), CD31 (red), FN (green), vWF (red), and Vim (green). Scale bars: 100 µm.

Following, the sprouting potential of both VUs after 24h of maturation was determined. VUs were entrapped in a fibrin hydrogel for a maximum period of 7 days. Previous work from our group had already demonstrated that spheroids containing OEC exhibited a great sprouting potential when embedded in fibrin by day 1 [120], [140]. They observed that prolonged spheroid culture (7 days maturation) abrogates OEC sprouting capacity, which could be related to the loss of OEC and to the progressive differentiation of the endothelial surface monolayer, where cells eventually become quiescent [120].

ZOE™ images showed remarkable sprouting immediately by day 1, that further increased until day 7 (Figure 34A). This was observed for both CAF-VUs and nFib-VUs. By day 7, it was noted that spheroids containing nFib had suffered extensive sprouting and that cells ended up dissociating from the initial spheroid and spread within the fibrin gel. On the other hand, CAF-VUs held their shape for longer and a core of aggregated cells could still be observed by day 7, probably due to the production of higher amounts of ECM proteins.

To confirm that endothelial cells were sprouting and organizing into vascular structures spheroids embedded in fibrin were immunostained for specific endothelial markers, namely CD31 at day 1, 3 and 7 (Figure 34B). At day 1, nFib-VUs exhibited some initial sprouting that continuously spread overtime. After 24h in fibrin, clusters of OEC (CD31+) in the core of CAF-VUs were visible and sprouting was reduced. However, as cells began to migrate out of the spheroid into the fibrin matrix, the core became gradually less dense, and eventually allowed the expansion of extensive sprouts. After 1 week, OECs formed robust sprouting networks, demonstrated by the long and organized endothelial structures shooting from the central spheroid. Remarkably, it was verified that sprouts of CAF-VUs seemed to form lumen-like structures giving promising results towards the establishment of a vascularized 3D *in vitro* model.

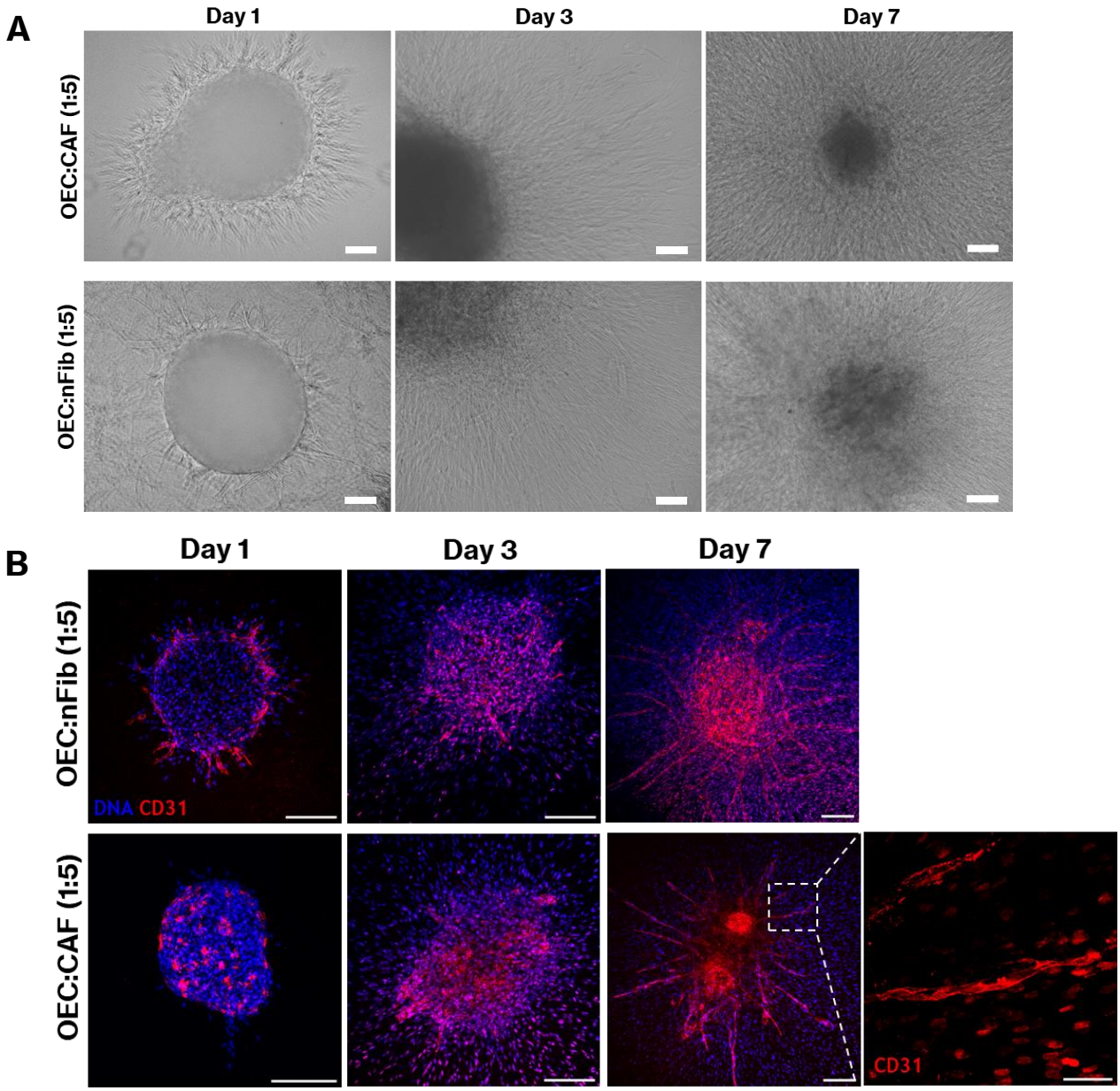

Figure 34 | Sprouting Assay - VUs embedded in fibrin hydrogels. A) ZOE™ images of day 1 VUs embedded in a fibrin gel at days 1, 3 and 7. Scale bars: 100 µm. B) CSLM images of cells stained for CD31 (red), DAPI (blue). Scale bars: 200 µm. The amplified section of the lumen-like structures on the right was taken with a 20X objective. Scale bar: 100 µm.

3.3.4 VUs Size Screening

Next, VUs (1:5 OEC:nFib) with lower cellular densities were generated to evaluate the lowest possible number of cells in a spheroid that could still allow for cells to aggregate, form a compact spheroid and outgrow. Since the final goal of the project was to incorporate these spheroids in a microfluidic platform, it was important to evaluate if smaller size spheroids could be formed and if they retained their sprouting potential. In this initial screening only nFib were used, since they were the ones that have shown less cohesiveness. VUs were generated with 1000, 500, 250 and 125 cells/spheroid and cultured for 7 days in small molds.

After 24h, spheroids with 1000, 500 and 250 cells exhibited an irregular shape, with rough edges and low circularity (Figure 35A). Nevertheless, cells managed to aggregate, and spheroids could form inside the wells of the agarose molds. Spheroids with 125 cells did not form by day 1, and only small clumps of cells, randomly arranged could be observed. However, after one week in culture, it was possible to observe small aggregates that seemed to have a more structured and compact organization.

On day 1, spheroid diameter ranged from 200 ± 22 μm for the 1000-spheroids to 85 ± 16 μm for the 125-spheroids, and their size decreased overtime to 162 ± 16 μm and 72 ± 13 μm respectively by day 7 (Figure 35B). After one week, all spheroids demonstrated a more compact and circular shape as observed with higher cell density using the same ratio 1:5. This may indicate that lower cell densities can still promote cell-cell and cell-matrix interactions leading to the formation of compact spheroids.

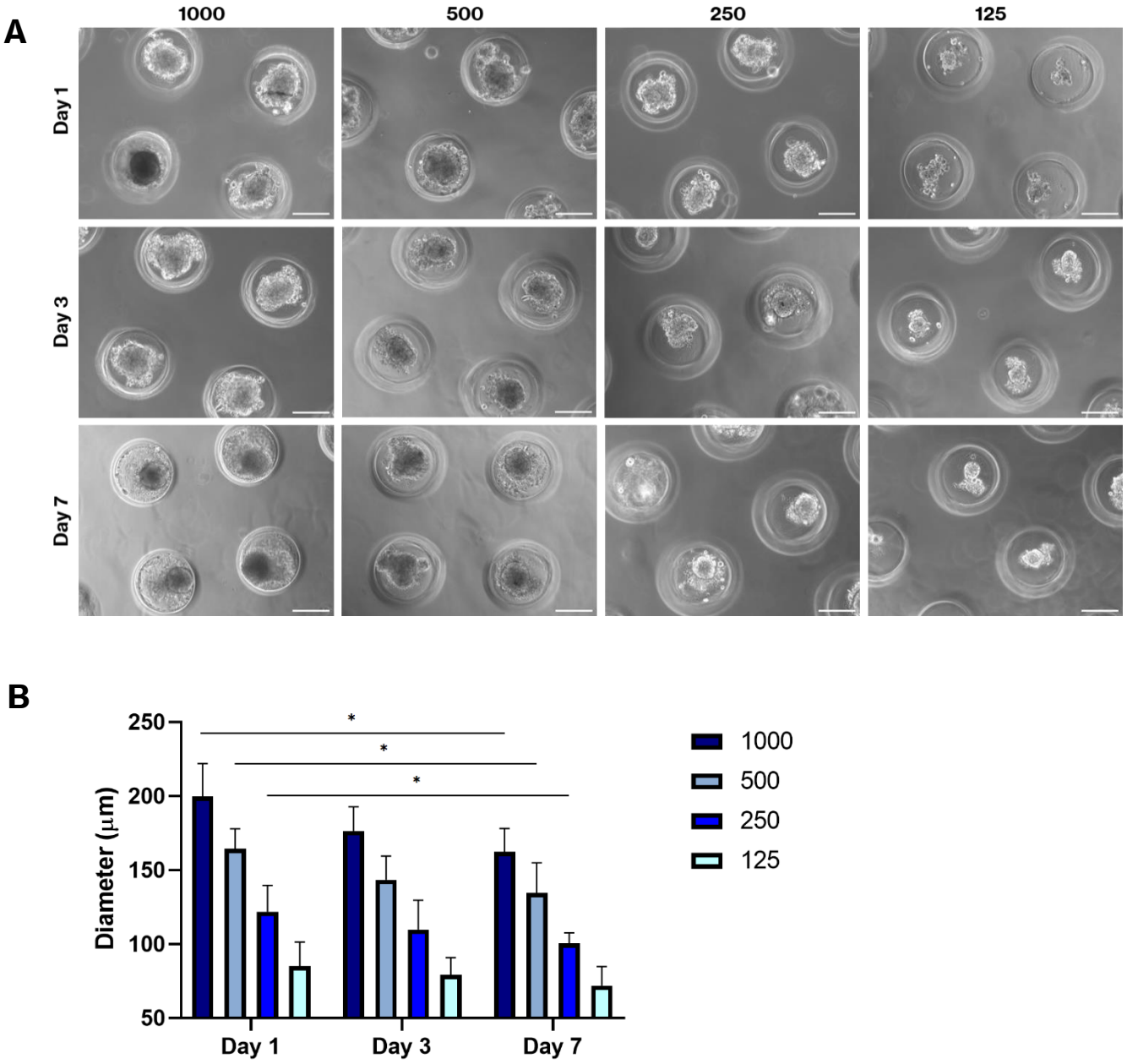

Figure 35 | nFib-VUs generated with 1000, 500, 250 and 125 cells/spheroid. A) Brightfield images acquired on day 1, 3 and 7. Scale bars: 200 µm. B) Diameter measurements overtime (n=20). Symbology: * indicates significant differences between different conditions at the same timepoint.

Due to the higher robustness of 1000, 500 and 250 spheroids by day 1, these spheroids were entrapped in a fibrin matrix to study their sprouting potential. After 24h in fibrin, cell migration into the gel could be observed for the three kinds of spheroids (Figure 36). Several sprouts were shown to expand forming tube-shaped structures into the surrounding matrix. By day 4, however, most spheroids were found disintegrating, as cells began disassociating from the spheroid into the matrix.

Altogether, these results demonstrated that spheroids with cell densities as low as 250 cells/spheroid are in fact able to aggregate and be compact enough for fibrin embedding, upon which, cells are able to migrate and form considerable sprouts.

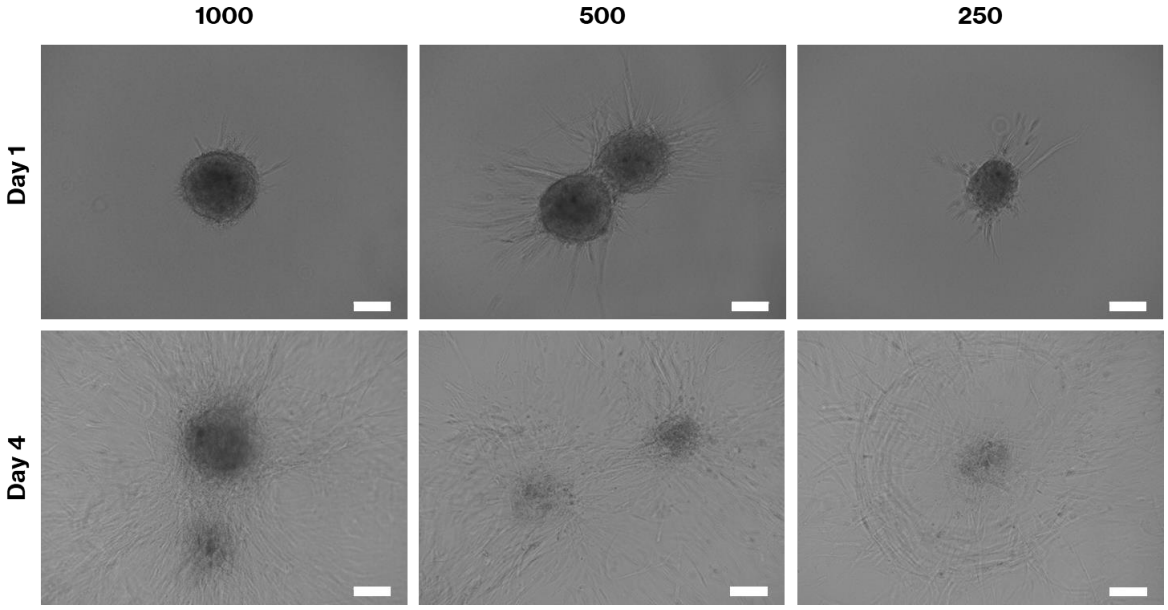

Figure 36 | Sprouting Assay for nFib-VUs with 1000, 500 and 250 cells/spheroid. ZOE™ images of day 1 VUs embedded in a fibrin gel at days 1 and 4. Scale bars: 100 µm.

3.4 Establishment of a Spheroid Culture within a well-defined ECM-like Matrix

3.4.1 Production and Characterization of a Multi-Functional Alginate Matrix via Thiol-Maleimide Click-Chemistry

The conjugation between a peptide and the alginate molecule involves the modification of the carboxylic acid on the alginate monomer to create an amide bond. A commonly used approach to insert amide bonds is with the carbodiimide chemistry using the coupling agent 1-Ethyl-3-(3-dimethylaminopropyl) carbodiimide/N-hydroxy succinimide (EDC/NHS) [105]. However, this method presents a slower rate when used with polymers with high molecular weight, due to the higher viscosity of the solution that results in a lower accessibility of the functional groups [141]. In addition, this approach requires the control of an acidic pH, leading to protonation of the amine group of the peptide. This means that there is a less efficient nucleophilic attack, which ultimately results in lower reaction yields. Another coupling agent that is gaining traction for alginate activation is the 4-(4,6-dimethoxy-1,3,5-triazine-2-yl)-4-methylmorpholinium chloride (DMTMM). This water-soluble agent is also resistant to hydrolysis and allows the formation of stable activated carboxyl acids without the need for pH control. Furthermore, DMTMM, which is cheaper and less toxic than EDC, does not generate N-acylurea by-products [142]. The insertion of a maleimide group is advantageous since it does not affect cell viability by the use of toxic chemicals or light-induced crosslinking [143].

To assess if the alginate modification was accomplished, H-NMR was performed, and results are depicted in Figure 37. The NMR spectra confirmed the presence of alginate with peaks at 5.126 – 4.966 ppm (1H) and 4.532 – 3.334 ppm (6H), successfully functionalized with maleimide with the characteristic peak at 6.968 – 6.818 ppm (2H).

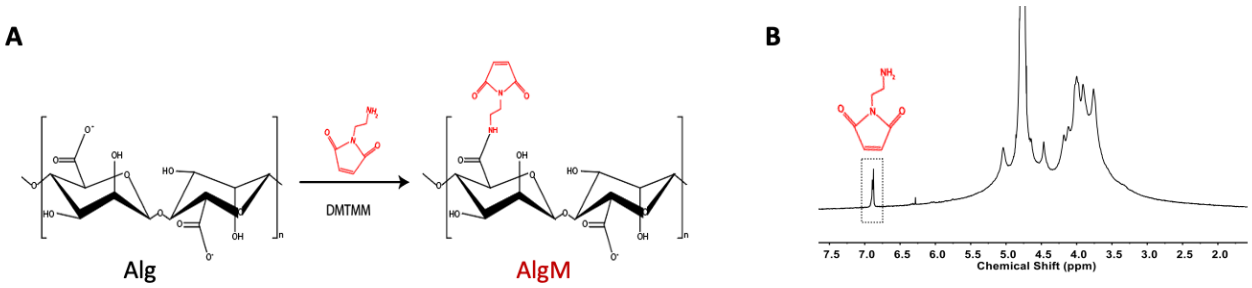

Figure 37 | Alginate modified with maleimides (AlgM). A) Schematic illustration of alginate modification with maleimide using DMTMM as coupling reagent. B) ^{1}H-NMR spectra of alginate modified with maleimide. A characteristic peak of maleimide is highlighted.

Maleimide-alginate can then be grafted with peptides via the Thiol-Michael addition reaction. This is a highly efficient reaction that due to its "click" nature, allows the conjugation of thiol-containing molecules with the maleimide molecule. In this case, the two peptides that were employed contain cysteine groups - RGD (CG_4RGDSP), that has one cysteine in one of its extremities, and GI-linker (CGPQGIWGQC) that has two cysteines, in both extremities. The reaction is schematized in Figure 38. Since the GI-linker can interact with different alginate chains, it will act as the crosslinking agent in the alginate matrix formation.

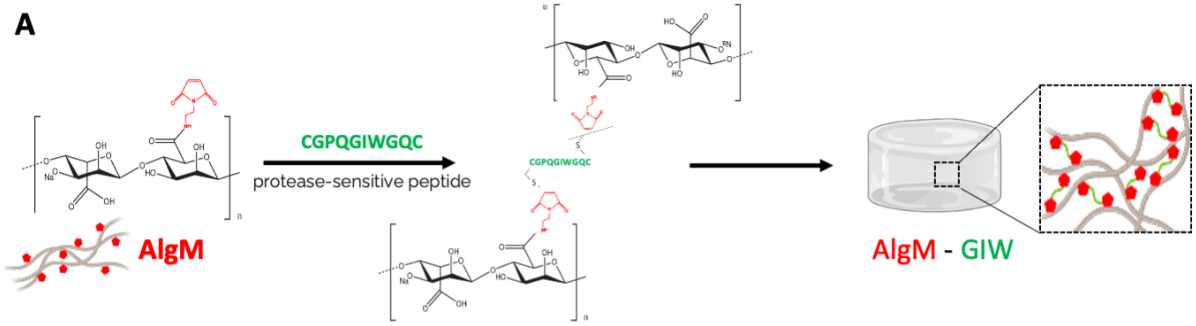

Figure 38 | Schematic representation of the process of grafting protease-sensitive peptide (CGPQCIWGQC, GI-peptide) to maleimide-alginate by thiol-Michael addition.

The rheological behavior of maleimide-alginate crosslinked with two concentrations of GI-peptide (120 and 240 μM) was tested by assessing gelation kinetics. The evolution of the elastic modulus over time was examined, while a deformation was being applied with a constant frequency [144]. For both GI concentrations, it was confirmed the formation of soft hydrogels, with AlgM-240GIW hydrogel presenting a higher stiffness (Figure 39). For both conditions, the elastic modulus G' was higher than the viscous modulus G'' with a low phase angle, which is characteristic of a more solid-like material.

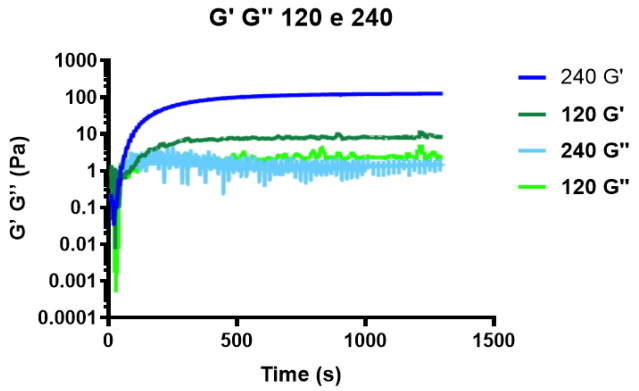

Figure 39 | Gelation kinetics of GI-crosslinked alginates. Alginate was crosslinked with two different concentrations of peptide: 120 and 240 μM. G' - storage modulus; G'' – loss modulus.

3.4.2 Tumoroids Embedded in a Bioresponsive 3D Alginate Matrix

Spheroids embedded in 3D matrices have emerged as powerful tools, that due to their physiological relevancy, are able to mimic key features of native tissues [111]. However, commonly used matrices, like Matrigel™, have high batch-to-batch variability and poorly tunable features, making it hard to evaluate and compare results from different experiments and/or different laboratories [57]. *In vitro* models that aim to replicate the tumor microenvironment more faithfully are gaining notable traction, as more research groups seek to find new ways of recreating the cellular organization and the ECM characteristics found *in vivo*. In this sense, ultra-pure alginate hydrogels have several advantages, namely the fact that they have a well-defined composition with features that are easily tunable and customizable [100], [105]. It had previously been reported that MMP-

sensitive pectin hydrogels enabled fibroblasts spreading [145]. Therefore, following experiments consisted in the embedding of tumoroids in a pre-synthesized multi-functional alginate hydrogel. Tumoroids were generated by the method sequential seeding after 6 days with MCF-7 and CAF/nFib using two different ratios: 1:1 (5 000 cells of each type) and 1:4 (2 000 MCF-7 and 8 000 CAF/nFib) and maintained for one week (Figure 40).

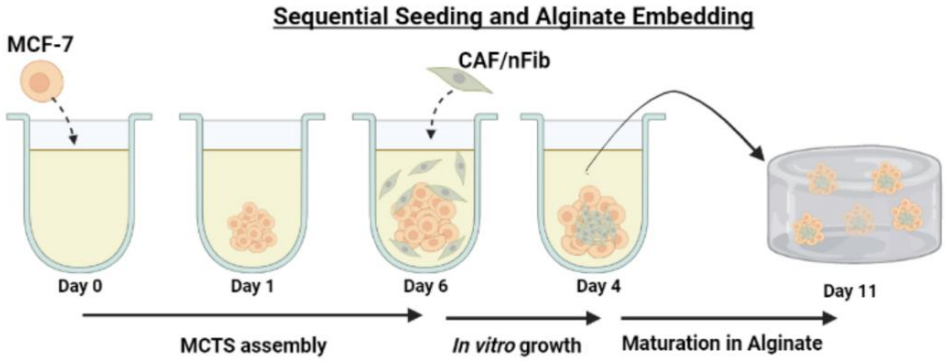

Figure 40 | Schematics of sequential seeding after 6 days followed by alginate embedding.

The tumoroids were succesffuly embedded with the bioresponsive alginate as depicted in Figure 41. On day 3, the conditions 1:1 (CAF and nFib) and 1:4 CAF-tumoroids exhibited similar results, with spheroids maintaining the morphology previous to embedding and a regular size. Interestingly, it was possible to observe that some 1:4 nFib-tumoroids already had some cells invading the alginate matrix, which was not the case for the other conditions, where spheroids displayed a smooth outer layer. CAF secrete higher amounts of ECM proteins that not only increase the stiffness of tumor tissues, but may also enhance epithelial cell adhesion [146]. After one week in alginate, tumoroids remained whole and retained their circular shape without disintegrating in the hydrogel.

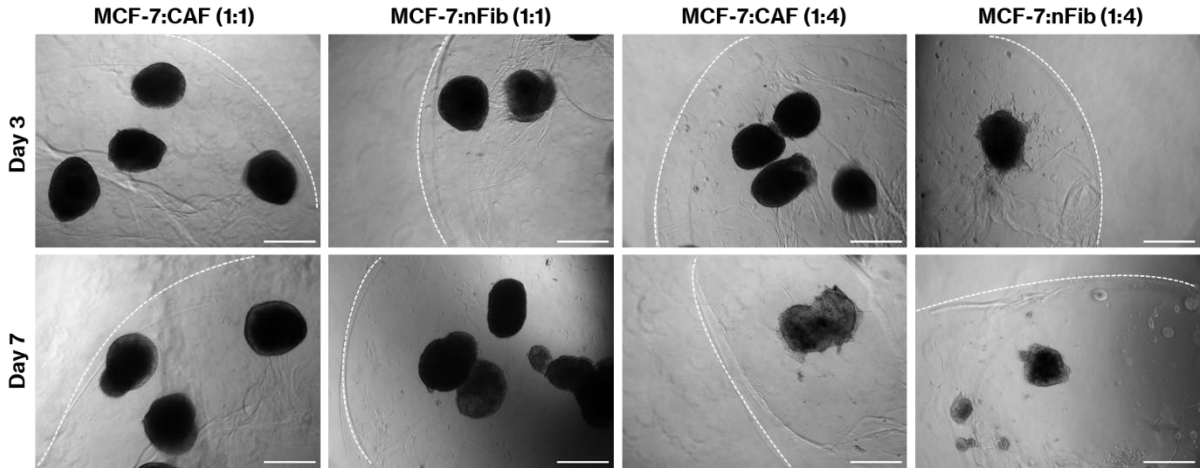

Figure 41 | Brightfield images of the different tumoroids embedded in a bioresponsive alginate modified with RGD and an MMP-sensitive peptide. Images were acquired at day 3 and day 7. The white dashed line delimits the periphery of the alginate disc. Scale bars: 500 µm.

To further comprehend the cellular organization and morphology within the spheroids, embedded tumoroids were fixed on day 3 and immunostainings were performed. Once again, E-cadherin (red) worked as a marker for epithelial cells, while vimentin (magenta) indicated the localization of fibroblasts. Phalloidin 488 probe was used to visualize the cytoskeleton (F-actin filaments - green).

All the tested conditions revealed the presence of an outer layer of epithelial cells (E-cad+) (Figure 42). CAF-tumoroids showed very low amounts of vimentin, and it was inclusively undetected in the 1:1 ratio. On the contrary, nFib-tumoroids exhibited significant networks of vimentin.

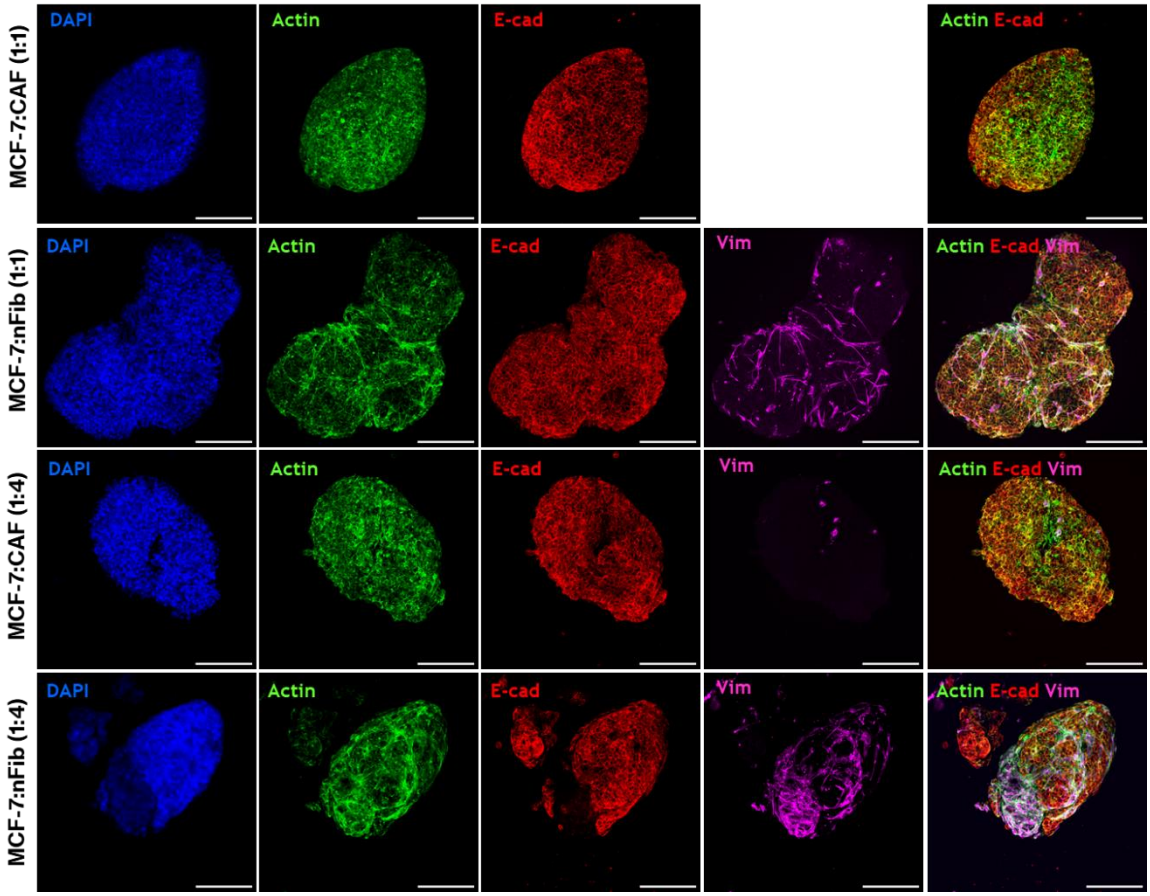

Figure 42 | Representative CLSM images of tumoroids embedded in a bioresponsive alginate by day 3. Cells were stained for DNA (nucleus, blue), F-actin (green), E-cad (red) and Vim (magenta). Scale bars: 200 µm**.**

To perform this embedding, tumoroids with 4 days maturation were used. In a future work we should study the effect of spheroid maturation on epithelial cells invasion since it is described that maturation has an impact on cell outgrowth within fibrin gels [120], [135]. Moreover, since this alginate matrix supports a longer period of culture, in future experiments longer time-points could be considered.

3.4.3 Bioresponsive Alginate 3D Matrix Supports VUs Outgrowth

Next, VUs ability to form vascular structures was evaluated by embedding them in the same alginate matrix used for tumoroids. Previous work from our group demonstrated that conjugating RGD sequences with alginate hydrogels does not just provides, but it is in fact mandatory to create a 3D environment suitable for endothelial cells to adhere and migrate [98]. According to aforementioned results obtained by VUs embedding in fibrin, extensive sprouting could be observed already by day 1, and by day 7, spheroids ended up disintegrating due to cell migration. Hence, day 1 CAF and nFib-VUs were entrapped in a matrix of alginate functionalized within RGD and MMP-sensitive peptide.

Brightfield images show that, by day 2, CAF-VUs begin sprouting and that those sprouts further increase in complexity overtime (Figure 43A). nFib-VUs sprouting is visible later, by day 4, and it also expands till day 7 (Figure 43B). Importantly, both types of VUs can hold their shape after one week embedded in alginate. This was not observed during fibrin-embedding, where, by day 7, cell migration was such that spheroids were practically undefined and VUs no longer had a distinct shape.

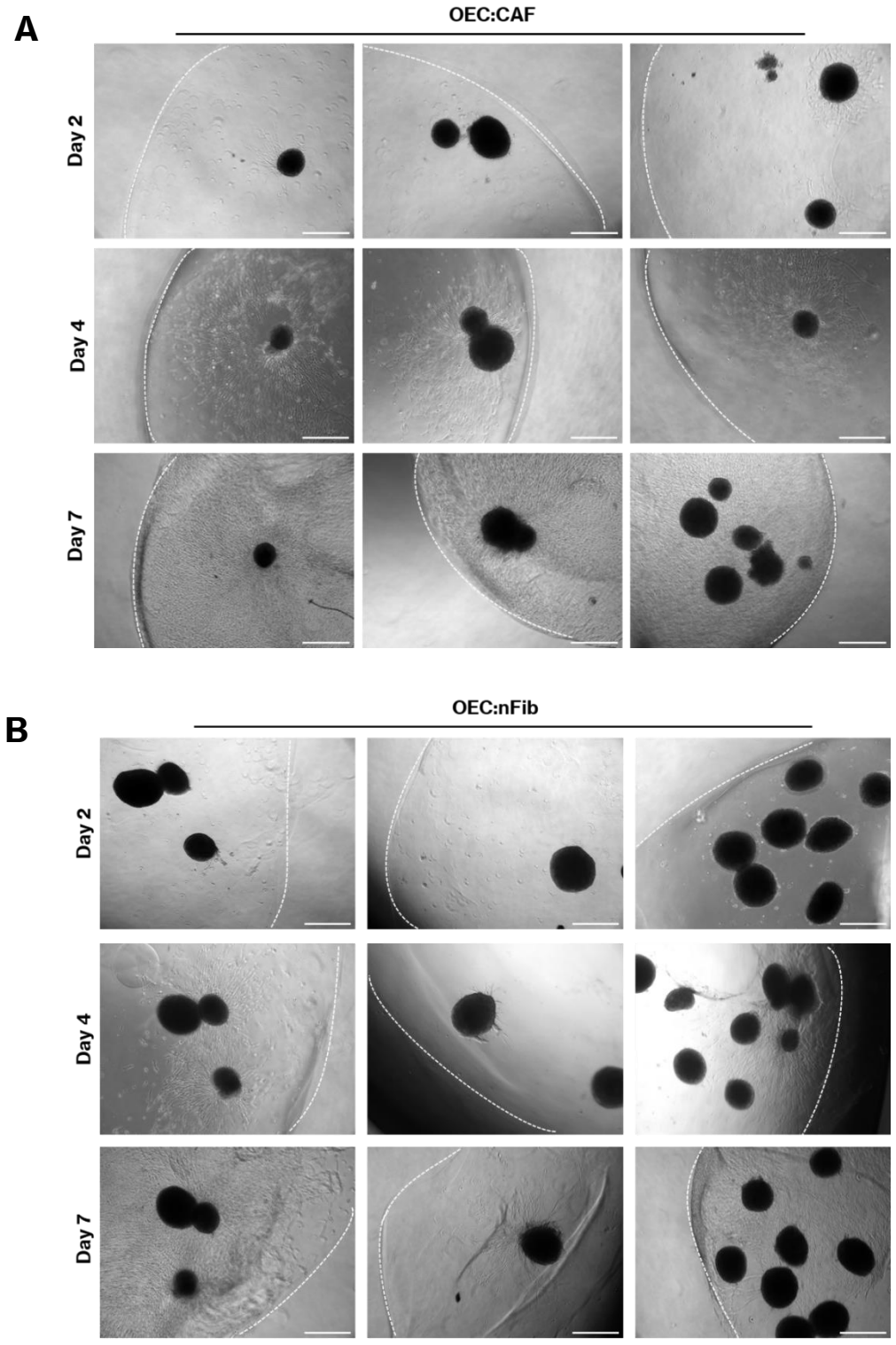

Figure 43 | Brightfield images of VUs (CAF-VUs (A) and nFib-VUs (B)) embedded in a bioresponsive alginate matrix. Images were acquired at day 2, 4 and 7. The white dashed line delimits the periphery of the alginate disc. Scale bars: 500 µm.

Cellular organization within the alginate matrix, together with sprouting potential were evaluated by immunohistochemistry. This time, cells were immunostained with a specific endothelial antibody designated Ulex Europaeus Agglutinin I (UEA I) labeled with rhodamine. This was performed so that vimentin staining (mouse anti-vimentin) could be carried out in the same samples, which was not possible with mouse anti-CD31 antibody.

Alginate samples were fixed at day 4 and 7, so that evolution of sprouting could be evaluated overtime. Confocal images revealed the formation of capillary-like structures by day 4 in both conditions (Figure 44). At day 7, it was observed for nFib-VUs that these structures expanded and displayed a higher complexity. It is possible that fibroblasts are able to provide additional support to the endothelial structures and contribute to their stable growth as observed by Feijão *et al.* [135].

Notably, it was verified that the endothelial sprouts were able to anastomose and form an intricate network of endothelial cells within the hydrogel (Figure 45). Moreover, the orthogonal views indicated that some of the structures were hollow, forming lumenized tubules already by day 4 in the CAF-VUs (Figure 45).

Another interesting aspect found in both conditions, was that at day 7, it was possible to observe that multiple spheroids could establish connections through endothelial cells (UEA I+) (Figure 46). In nFib-VUs, vimentin staining was detected surrounding the endothelial structures. This suggests that fibroblasts may have a potential role in supporting the establishment of vascular structures. This contributes to the increasing relevancy of multicellular spheroids, demonstrating how cell-cell interactions are essential when designing 3D *in vitro* models.

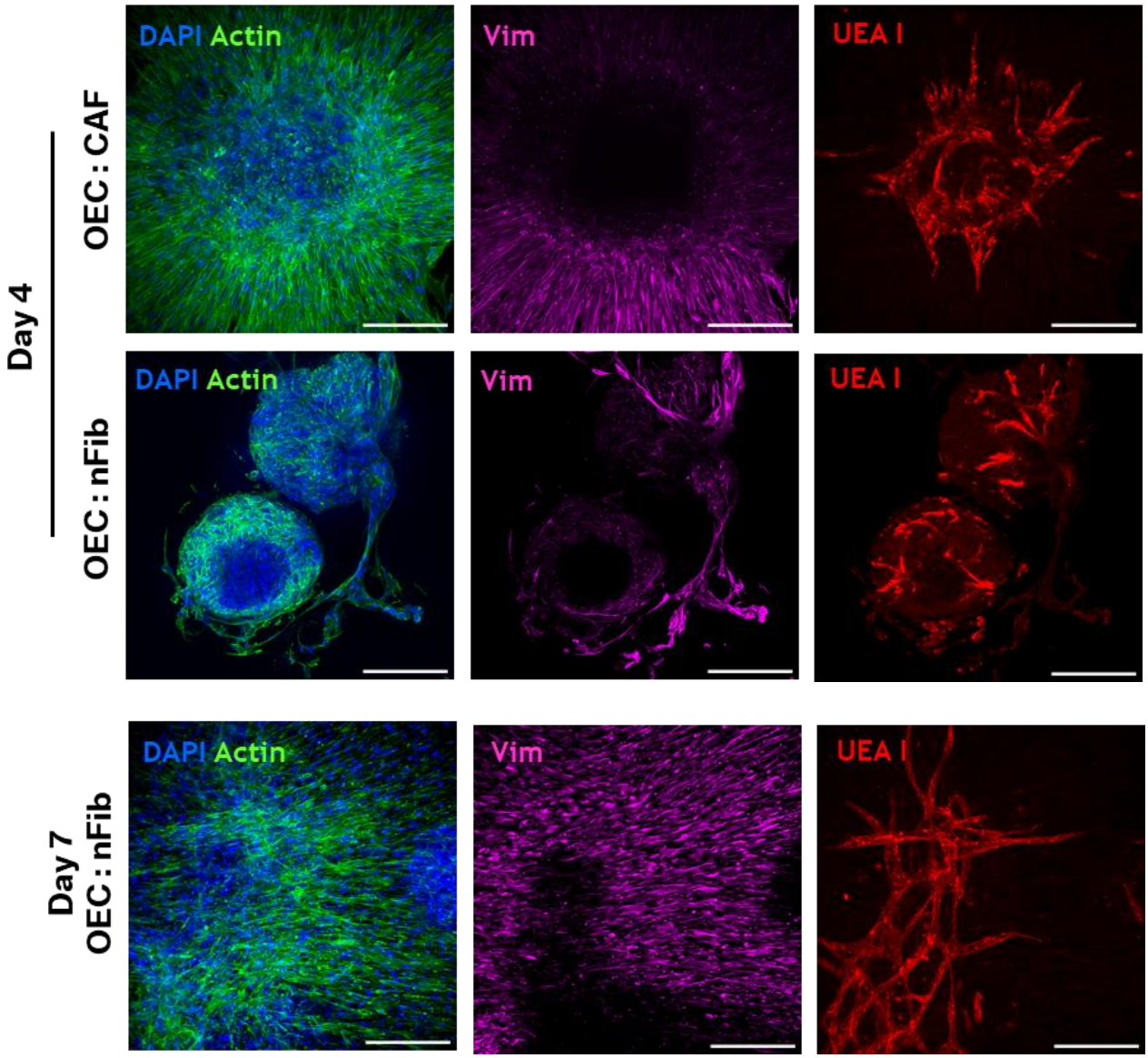

Figure 44 | Cellular organization within VUs embedded in bioresponsive alginate. CLSM images acquired on day 4 and 7. Cells were stained for DNA (nucleus, blue), F-actin (green), UEA I (red), Vim (magenta). Scale bars: 200 µm.

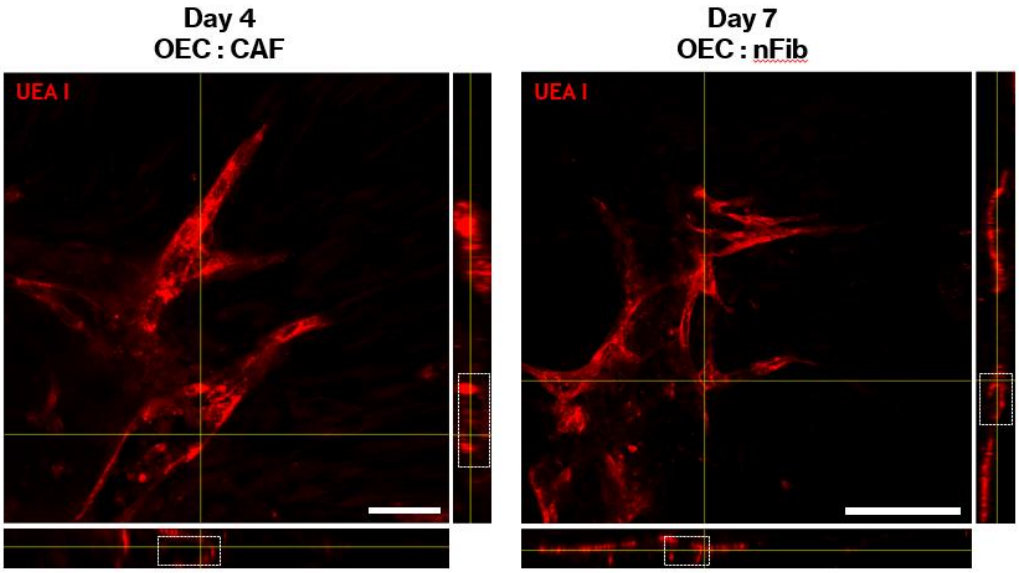

Figure 45 | Vascular-like structures formed by VUs in the alginate matrix. CLSM images and respective orthogonal views. Cells were stained for UEA I (red). Scale bars: 50 µm. Left image was acquired with a 1.5X zoom.

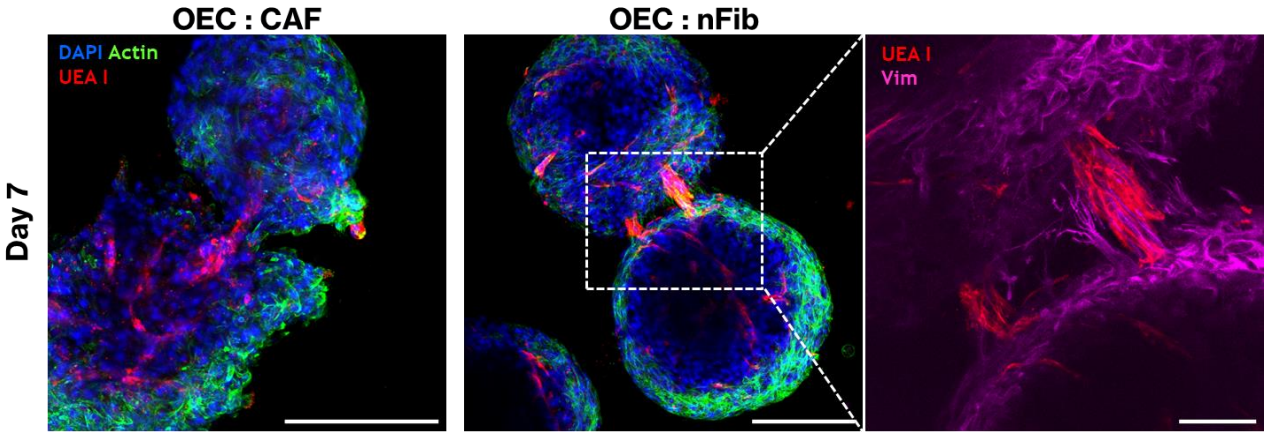

Figure 46 | CLSM images of different VUs establishing endothelial connections within alginate. Cells were stained for DNA (nucleus, blue), F-actin (green), UEA I (red), Vim (magenta). Scale bars: 200 µm. Right picture represents a zoom of 3X of the highlighted area. Scale bar: 50 µm.

3.5 Microfluidic Design

To further investigate and better control the interactions between all the previous cell types and evaluate the potential of establishing a vascularized 3D model, a microfluidic device was designed to incorporate and compartmentalize the different spheroids in a single device. The idea was to individualize the parenchyma and vascular/stromal compartments. This platform will allow to identify relevant features that determine the path of cancer progression, such as cancer cell migration and cancer-vascular crosstalk [77]. The key role of tumor vasculature in the evolution of breast cancer has been pushing many research groups into developing microfluidic platforms with established vascular networks that modulate the TME.

The first design consisted of a device with three parallel channels based on the one developed by Nashimoto *et al.* [76]. Figure 47 shows the initial design, with spaces between the microchannels and the size of the microchannels similar do the original, the difference was the height of the parallel channels that was 1 mm higher. 3D printing, despite its many advantages, proved to have some difficulties in reproducing the design. Due to the lower resolution achievable, the dimensions of the microchannels separating the parallel channels were altered to fit the fabrication method and the pillars were removed, except the central one (Figure 47B-ii).

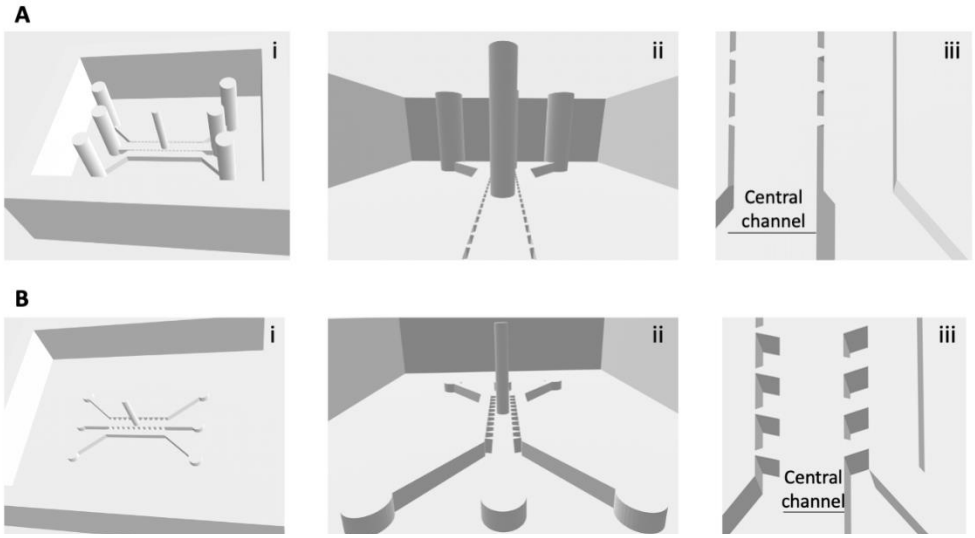

Figure 47 | Design evolution of the microfluidic device. 3D images of the first (A) and improved (B) design of the microfluidic device. B) For both (A) and (B) are displayed an offset (i), inside (ii) and detailed (iii) view of the channels.

The definition of the microchannels was improved upon a review of the design and washing process for the molds. The insufficient depth of the depressions was found to be caused by an accumulation of partly cured resin in the holes due to their small size (Figure 47A-iii). This was addressed in the last design by increasing the distance between the microchannels (Figure 47B-iii). In addition, a sonication step was added to the washing procedure of molds in isopropanol. Figure 48B shows an image of the resulting mold, where microchannels are significantly more defined than in the previous designs (Figure 48A).

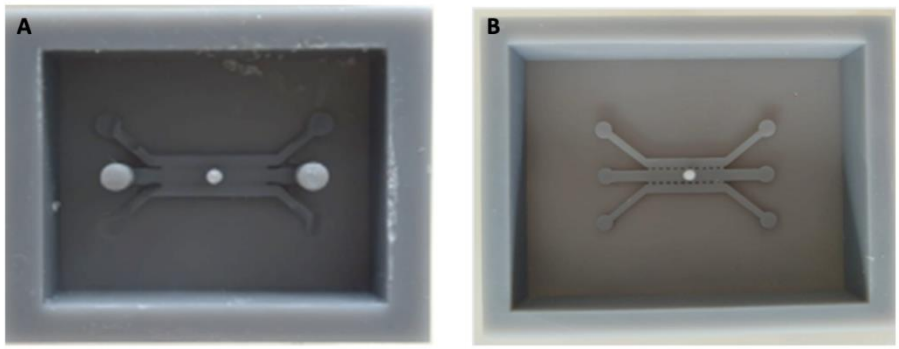

Figure 48 | Pictures of 3D printed molds. The first (A) and the improved (B) designs of the microfluidic device were 3D printed using a FormLabs™ Form3 Low Force Stereolithography (LFS) 3D printer.

Overall, using 3D printing as a fabrication method allowed for molds to be fabricated within two days of designing. This allows for multiple upgrades to be performed in a faster way, in comparison to the lengthier method of soft lithography. In the near future, this final mold will be used to fabricate our PDMS microfluidic platform and confirm the microchannels definition.

Chapter 4 - Concluding Remarks and Future Work

With an increasingly aging population, cancer is ever more relevant in today's society. Breast cancer is currently the leading cause of death for women and its incidence grows every year with more than 2 million cases diagnosed in 2020. The aggressiveness of this disease makes finding optimal treatment options that can improve patients' survival a priority. Overwhelming efforts have been done by the scientifical community to design innovative pre-clinical models with the aim of truthfully replicating the disease *in vitro*. However, many of those models lack key features present in the native tumor tissues that deeply influence how cancer cells behave and the overall evolution of the disease. Hence, it is crucial to try to eliminate such discrepancies and target those elements that will enable the accurate replicate of a breast tumor *in vitro*.

Three-dimensional models are considered powerful tools with the ability to tackle many of the current obstacles found with 2D models. Namely, multicellular spheroids embedded in 3D matrices and microfluidic devices are some of the most commonly applied strategies as ways to achieve a complete pre-clinical model of breast cancer. These strategies can encompass multiple features of cancer tissues, such as replicate the tumor microenvironment or integrate interactions between different cell types. Additionally, angiogenesis, which is considered an hallmark of cancer and determinant in the outcome of the disease, can also be replicated using such models. Although existing strategies have contributed tremendously to breast cancer knowledge and research, it is crucial to continue exploring new methods to develop more complex and integrative models. In that sense, the main goal of this thesis was to develop a

vascularized 3D *in vitro* platform, that could serve as a research tool to further study the role of angiogenesis in breast cancer. To reach that goal, the project was divided in two main branches: the development of tumoroids, coculture spheroids that replicate the breast tumor itself, and the development of vascular units (VUs), that represent the surrounding stroma. Both branches would then converge in a microfluidic device, in which alginate-embedded spheroids could establish cellular connections. This platform could ultimately be a comprehensive tool to study the various interactions between all the major cell types found in breast tumors, and also how the alginate matrix plays a role in their behavior.

The first set of experiments aimed to characterize MCF-7 spheroids and evaluate how cell density (ranging from 1000 to 10 000 cells/spheroid) impacted spheroid uniformity and how their size changes overtime. MCF-7 spheroids were successfully established with all different densities. Spheroids increased in size until day 7 of culture and were able to maintain their integrity. Additionally, these spheroids were generated using a high-throughput method of non-adherent agarose microwells that promoted quick cellular aggregation. The agarose molds were also used in further experiments due to their efficiency and ease of use. Afterwards, fibroblasts were cocultured with MCF-7 cells. Integrating fibroblasts was crucial to generate tumor spheroids, also known as tumoroids, that can meticulously reproduce the core properties of a breast tumor. CAF and nFib are highly abundant in the tumor microenvironment (TME) and are undoubtedly key players during tumor evolution, especially since they can directly communicate with cancer cells and influence their behavior. These two fibroblasts were first characterized in terms of gene expression. Key genes expressed by fibroblasts such as FSP1 or FAP were upregulated in CAFs, as well as ECM proteins (type I collagen and fibronectin) and MMPs (MMP-2 and MMP-14) expression. Then these fibroblasts were seeded together with MCF-7 cells using three different seeding approaches: simultaneously, where a suspension of the two cell types (MCF-7:CAF/nFib) was created and added to agarose molds on day 0; sequentially after 24h, where CAF/nFib were added to preformed MCF-7 spheroids after these had been in culture for 24h; and lastly, sequentially after 6 days, where fibroblasts were added to 6 day old MCF-7 spheroids. The goal was to develop tumoroids whose cellular organization closer resembled the one found *in vivo*, with tumor cells in the center circled by fibroblasts. Results revealed that the seeding strategy

strongly impacts the organization taken by cells. Although fibroblasts always ended up aggregating in the core of the spheroid, it was found that by adding fibroblasts on the 6th day, they could occupy a larger area of the spheroid without being rapidly overgrown by epithelial cells. That was more evident with tumoroids containing higher amounts of fibroblasts in the ratio 1:4. It was also possible to see an area of necrotic cells within the spheroid, corresponding to the core of MCF-7 after 6 days in culture. In terms of size, it was noted that CAF-tumoroids were generally smaller, which is explained by their increased matrix producing ability and consequent stiffening.

In the second step, vascular units (VUs) were designed with the capacity to establish sprouting structures when embedded in 3D fibrin and alginate matrices. Different outgrowth endothelial cells and fibroblasts (CAF and nFib) ratios and maturation time were considered. VUs with 1:5 ratio showed a correct incorporation of the two cell types, forming the most compact and even spheroids with a diameter of around 350 µm at day 1. Their size decreased overtime, once again due to spheroids' compaction caused by matrix production by fibroblasts. Importantly, these VUs formed organized endothelial structures that resembled primitive capillary vessels.

VUs (with 1 day of culture) embedded in fibrin and alginate hydrogels exhibited extensive radial sprouting. Surprisingly, these sprouts formed complex networks not only in fibrin, but in our multi-functional alginate and anastomosis was visible for sprouts from different spheroids. Remarkably, some of these capillary-like structures were hollow, indicating the formation of a lumen. The structures were supported by surrounding fibroblasts, that also helped establish intricate communications between different spheroids.

The biofunctionalized maleimide-modified alginate originated a multi-functional and bioresponsive ECM-like matrix that allowed cell invasion and supported capillary vessels formation. In the future both spheroids (tumoroids and VUs) could be embedded in this well-defined matrix to replicate and investigate tumor vascularization. Future perspectives will also be focused on optimizing the embedding of spheroids within alginate. It is vital that spheroids are not damaged during this process and that, upon embedding, alginate fully crosslinks. The alginate disc should be uniform and devoid of

imperfections in the matrix that could influence spheroid's growth. Moreover, this tunable alginate could be used as a 3D matrix in a microfluidic platform.

To improve the control over the vascularization process, a microfluidic platform, in which both parenchymal and vascular/stromal compartments are separated, will help to investigate interactions between these two 3D cellular aggregates. With this in mind, we have made the first steps on the design of such platform based on a previous published device. This platform should be height enough to allow the incorporation of spheroids embedded in our bioresponsive alginate. But at the same time, the separation between compartments should allow cell invasion, capillary vessels formation and multicellular crosstalk. To achieve this a polydimethylsiloxane (PDMS) microfluidic was fabricated with three parallel channels, separated by micropillars (100 μm). Although some improvements were made, optimizations in terms of resolution are still ongoing. Nevertheless, it will certainly have a huge impact into the comprehension of the interaction between these two 3D cellular aggregates, and in the long run, will contribute to a better understanding of breast cancer disease.

In the future, models like these will continue to evolve and will certainly be faithful tools, broadly applied by the scientific community and industry for the most diverse applications, from fundamental research studies to drug screening. Slowly but steady, the knowledge about breast cancer will improve and it will be possible to achieve better treatment options for patients around the world, and eventually this worldwide burden won't have such a massive impact in today's lives.

References

[1] A. B. Rivard, L. Galarza-Paez, and D. C. Peterson, 'Anatomy, Thorax, Breast', in *StatPearls*, Treasure Island (FL): StatPearls Publishing, 2022. Accessed: Feb. 24, 2022. [Online]. Available: http://www.ncbi.nlm.nih.gov/books/NBK519575/

[2] P. J. Bazira, H. Ellis, and V. Mahadevan, 'Anatomy and physiology of the breast', *Surgery - Oxford International Edition*, vol. 40, no. 2, pp. 79–83, Dec. 2021, doi: 10.1016/j.mpsur.2021.11.015.

[3] C. Perry, 'What Are Montgomery's Tubercles?', *Parents*, Jan. 13, 2022. https://www.parents.com/pregnancy/my-body/pregnancy-health/montgomerys-tubercles/ (accessed Mar. 18, 2022).

[4] 'Mammary Glands and Anatomy of the Breast - Female Reproductive System', *BrainKart*, 2018. https://www.brainkart.com/article/Mammary-Glands-and-Anatomy-of-the-Breast---Female-Reproductive-System_21995/ (accessed Jun. 01, 2022).

[5] G. Zucca-Matthes, C. Urban, and A. Vallejo, 'Anatomy of the nipple and breast ducts', *Gland Surg*, vol. 5, no. 1, pp. 32–36, Feb. 2016, doi: 10.3978/j.issn.2227-684X.2015.05.10.

[6] F. Hassiotou and D. Geddes, 'Anatomy of the human mammary gland: Current status of knowledge', *Clin. Anat.*, vol. 26, no. 1, pp. 29–48, Jan. 2013, doi: 10.1002/ca.22165.

[7] S. Cieśla, M. Wichtowski, R. Poźniak-Balicka, and D. Murawa, 'The surgical anatomy of the mammary gland (part 1.). General structure, embryogenesis, histology, the nipple-areolar complex, the fascia of the glandular tissue and the chest wall', *Nowotwory. Journal of Oncology*, vol. 70, no. 5, Art. no. 5, 2020, doi: 10.5603/NJO.2020.0042.

[8] A. Aranda-Gutierrez and H. M. Diaz-Perez, 'Histology, Mammary Glands', in *StatPearls*, Treasure Island (FL): StatPearls Publishing, 2022. Accessed: Mar. 23, 2022. [Online]. Available: http://www.ncbi.nlm.nih.gov/books/NBK547732/

[9] N. T. Cacho and R. M. Lawrence, 'Innate Immunity and Breast Milk', *Frontiers in Immunology*, vol. 8, 2017, Accessed: Mar. 25, 2022. [Online]. Available: https://www.frontiersin.org/article/10.3389/fimmu.2017.00584

[10] U. F. O. Themes, 'Breast Surgery', *Basicmedical Key*, Dec. 10, 2016. https://basicmedicalkey.com/breast-surgery/ (accessed Jun. 01, 2022).

[11] S. Pacifici and C. Hacking, 'Lymphatic drainage of the breast', *Radiopaedia*, May 11, 2013. https://radiopaedia.org/articles/lymphatic-drainage-of-the-breast?lang=us (accessed Mar. 25, 2022).

[12] Y. S. Khan and H. Sajjad, 'Anatomy, Thorax, Mammary Gland', in *StatPearls*, Treasure Island (FL): StatPearls Publishing, 2021. Accessed: Mar. 25, 2022. [Online]. Available: http://www.ncbi.nlm.nih.gov/books/NBK547666/

[13] J. H. T. G. Fregnani and J. R. Macéa, 'Lymphatic Drainage of the Breast: from Theory to Surgical Practice', *Int. J. Morphol.*, vol. 27, no. 3, Sep. 2009, doi: 10.4067/S0717-95022009000300038.

[14] H. Sung *et al.*, 'Global Cancer Statistics 2020: GLOBOCAN Estimates of Incidence and Mortality Worldwide for 36 Cancers in 185 Countries', *CA: A Cancer Journal for Clinicians*, vol. 71, no. 3, pp. 209–249, 2021, doi: 10.3322/caac.21660.

[15] R. L. Siegel, K. D. Miller, H. E. Fuchs, and A. Jemal, 'Cancer Statistics, 2021', *CA: A Cancer Journal for Clinicians*, vol. 71, no. 1, pp. 7–33, 2021, doi: 10.3322/caac.21654.

[16] M. Akram, M. Iqbal, M. Daniyal, and A. U. Khan, 'Awareness and current knowledge of breast cancer', *Biol Res*, vol. 50, p. 33, Oct. 2017, doi: 10.1186/s40659-017-0140-9.

[17] G. N. Sharma, R. Dave, J. Sanadya, P. Sharma, and K. K. Sharma, 'VARIOUS TYPES AND MANAGEMENT OF BREAST CANCER: AN OVERVIEW', *J Adv Pharm Technol Res*, vol. 1, no. 2, pp. 109–126, 2010.

[18] W. Chen, A. D. Hoffmann, H. Liu, and X. Liu, 'Organotropism: new insights into molecular mechanisms of breast cancer metastasis', *npj Precision Onc*, vol. 2, no. 1, Art. no. 1, Feb. 2018, doi: 10.1038/s41698-018-0047-0.

[19] Z. Liu, X.-S. Zhang, and S. Zhang, 'Breast tumor subgroups reveal diverse clinical prognostic power', *Sci Rep*, vol. 4, no. 1, Art. no. 1, Feb. 2014, doi: 10.1038/srep04002.

[20] T. Sørlie, 'Molecular portraits of breast cancer: tumour subtypes as distinct disease entities', *European Journal of Cancer*, vol. 40, no. 18, pp. 2667–2675, Dec. 2004, doi: 10.1016/j.ejca.2004.08.021.

[21] L. J. van 't Veer *et al.*, 'Gene expression profiling predicts clinical outcome of breast cancer', *Nature*, vol. 415, no. 6871, Art. no. 6871, Jan. 2002, doi: 10.1038/415530a.

[22] I. Januškevičienė and V. Petrikaitė, 'Heterogeneity of breast cancer: The importance of interaction between different tumor cell populations', *Life Sciences*, vol. 239, p. 117009, Dec. 2019, doi: 10.1016/j.lfs.2019.117009.

[23] D. Fitzpatrick-Lewis, N. Hodgson, D. Ciliska, L. Peirson, M. Gauld, and Y. Yun Liu, 'Breast Cancer Screening', McMaster University, Hamilton, Ontario, Canada, 2011. Accessed: Mar. 11, 2022. [Online]. Available:

https://portaldeboaspraticas.iff.fiocruz.br/wp-content/uploads/2019/02/2011-breast-cancer-systematic-review-en.pdf

[24] L. Wang, 'Early Diagnosis of Breast Cancer', *Sensors*, vol. 17, no. 7, Art. no. 7, Jul. 2017, doi: 10.3390/s17071572.

[25] E. S. McDonald, A. S. Clark, J. Tchou, P. Zhang, and G. M. Freedman, 'Clinical Diagnosis and Management of Breast Cancer', *J Nucl Med*, vol. 57 Suppl 1, pp. 9S-16S, Feb. 2016, doi: 10.2967/jnumed.115.157834.

[26] M. Zubair, S. Wang, and N. Ali, 'Advanced Approaches to Breast Cancer Classification and Diagnosis', *Frontiers in Pharmacology*, vol. 11, 2021, Accessed: Mar. 29, 2022. [Online]. Available: https://www.frontiersin.org/article/10.3389/fphar.2020.632079

[27] R. Colomer *et al.*, 'Biomarkers in breast cancer: A consensus statement by the Spanish Society of Medical Oncology and the Spanish Society of Pathology', *Clin Transl Oncol*, vol. 20, no. 7, pp. 815–826, Jul. 2018, doi: 10.1007/s12094-017-1800-5.

[28] A. Mehrgou and M. Akouchekian, 'The importance of BRCA1 and BRCA2 genes mutations in breast cancer development', *Med J Islam Repub Iran*, vol. 30, p. 369, May 2016.

[29] M. F. Walsh, K. L. Nathanson, F. J. Couch, and K. Offit, 'Genomic Biomarkers for Breast Cancer Risk', *Adv Exp Med Biol*, vol. 882, pp. 1–32, 2016, doi: 10.1007/978-3-319-22909-6_1.

[30] B. Weigelt, J. L. Peterse, and L. J. van't Veer, 'Breast cancer metastasis: markers and models', *Nat Rev Cancer*, vol. 5, no. 8, pp. 591–602, Aug. 2005, doi: 10.1038/nrc1670.

[31] J. Lu *et al.*, 'Breast Cancer Metastasis: Challenges and Opportunities', *Cancer Research*, vol. 69, no. 12, pp. 4951–4953, Jun. 2009, doi: 10.1158/0008-5472.CAN-09-0099.

[32] O. J. Scully, B.-H. Bay, G. Yip, and Y. Yu, 'Breast cancer metastasis', *Cancer Genomics Proteomics*, vol. 9, no. 5, pp. 311–320, Oct. 2012.

[33] R. Derynck and R. A. Weinberg, 'EMT and Cancer: More Than Meets the Eye', *Developmental Cell*, vol. 49, no. 3, pp. 313–316, May 2019, doi: 10.1016/j.devcel.2019.04.026.

[34] L. Wang, S. Zhang, and X. Wang, 'The Metabolic Mechanisms of Breast Cancer Metastasis', *Frontiers in Oncology*, vol. 10, 2021, Accessed: Mar. 28, 2022. [Online]. Available: https://www.frontiersin.org/article/10.3389/fonc.2020.602416

[35] Y. Shamay *et al.*, 'P-selectin is a nanotherapeutic delivery target in the tumor microenvironment', *Sci Transl Med*, vol. 8, no. 345, p. 345ra87, Jun. 2016, doi: 10.1126/scitranslmed.aaf7374.

[36] S. P. H. Chiang, R. M. Cabrera, and J. E. Segall, 'Tumor cell intravasation', *American Journal of Physiology-Cell Physiology*, vol. 311, no. 1, pp. C1–C14, Jul. 2016, doi: 10.1152/ajpcell.00238.2015.

[37] D. R. Caswell and C. Swanton, 'The role of tumour heterogeneity and clonal cooperativity in metastasis, immune evasion and clinical outcome', *BMC Medicine*, vol. 15, no. 1, p. 133, Jul. 2017, doi: 10.1186/s12916-017-0900-y.

[38] Q. Wu *et al.*, 'Breast cancer subtypes predict the preferential site of distant metastases: a SEER based study', *Oncotarget*, vol. 8, no. 17, pp. 27990–27996, Mar. 2017, doi: 10.18632/oncotarget.15856.

[39] N. Nishida, H. Yano, T. Nishida, T. Kamura, and M. Kojiro, 'Angiogenesis in Cancer', *Vasc Health Risk Manag*, vol. 2, no. 3, pp. 213–219, Sep. 2006.

[40] P. Carmeliet and R. K. Jain, 'Angiogenesis in cancer and other diseases', *Nature*, vol. 407, no. 6801, Art. no. 6801, Sep. 2000, doi: 10.1038/35025220.

[41] D. Hanahan and J. Folkman, 'Patterns and Emerging Mechanisms of the Angiogenic Switch during Tumorigenesis', *Cell*, vol. 86, no. 3, pp. 353–364, Aug. 1996, doi: 10.1016/S0092-8674(00)80108-7.

[42] I. Zuazo-Gaztelu and O. Casanovas, 'Unraveling the Role of Angiogenesis in Cancer Ecosystems', *Frontiers in Oncology*, vol. 8, 2018, Accessed: Mar. 05, 2022. [Online]. Available: https://www.frontiersin.org/article/10.3389/fonc.2018.00248

[43] R. Lugano, M. Ramachandran, and A. Dimberg, 'Tumor angiogenesis: causes, consequences, challenges and opportunities', *Cell Mol Life Sci*, vol. 77, no. 9, pp. 1745–1770, 2020, doi: 10.1007/s00018-019-03351-7.

[44] K. Shirakawa *et al.*, 'Induction of vasculogenesis in breast cancer models', *Br J Cancer*, vol. 87, no. 12, pp. 1454–1461, Dec. 2002, doi: 10.1038/sj.bjc.6600610.

[45] Ş. Comşa, F. Ciuculescu, and M. Raica, 'Mesenchymal stem cell-tumor cell cooperation in breast cancer vasculogenesis', *Molecular Medicine Reports*, vol. 5, no. 5, pp. 1175–1180, May 2012, doi: 10.3892/mmr.2012.796.

[46] Y. Mao *et al.*, 'Stem-like tumor cells involved in heterogeneous vasculogenesis in breast cancer', *Endocrine-Related Cancer*, vol. 27, no. 1, pp. 23–39, Jan. 2020, doi: 10.1530/ERC-19-0054.

[47] C. Unger, N. Kramer, A. Walzl, M. Scherzer, M. Hengstschläger, and H. Dolznig, 'Modeling human carcinomas: physiologically relevant 3D models to improve anti-cancer drug development', *Adv Drug Deliv Rev*, vol. 79–80, pp. 50–67, Dec. 2014, doi: 10.1016/j.addr.2014.10.015.

[48] J. T. Emerman, S. J. Burwen, and D. R. Pitelka, 'Substrate properties influencing ultrastructural differentiation of mammary epithelial cells in culture', *Tissue and Cell*, vol. 11, no. 1, pp. 109–119, Jan. 1979, doi: 10.1016/0040-8166(79)90011-9.

[49] N. de Souza, 'Organoids', *Nat Methods*, vol. 15, no. 1, pp. 23–23, Jan. 2018, doi: 10.1038/nmeth.4576.

[50] A. O. Sasmita and Y. P. Wong, 'Organoids as Reliable Breast Cancer Study Models: An Update', *Int J Oncol Res*, vol. 1, no. 2, Dec. 2018, doi: 10.23937/ijor-2017/1710008.

[51] L. L. Bischel, D. J. Beebe, and K. E. Sung, 'Microfluidic model of ductal carcinoma in situ with 3D, organotypic structure', *BMC Cancer*, vol. 15, no. 1, p. 12, Jan. 2015, doi: 10.1186/s12885-015-1007-5.

[52] J. F. Dekkers *et al.*, 'Modeling Breast Cancer Using CRISPR-Cas9–Mediated Engineering of Human Breast Organoids', *JNCI: Journal of the National Cancer Institute*, vol. 112, no. 5, pp. 540–544, May 2020, doi: 10.1093/jnci/djz196.

[53] K. Yanagisawa *et al.*, 'A Four-Dimensional Organoid System to Visualize Cancer Cell Vascular Invasion', *Biology (Basel)*, vol. 9, no. 11, p. 361, Oct. 2020, doi: 10.3390/biology9110361.

[54] R. Fernández-Periáñez *et al.*, 'Basement Membrane-Rich Organoids with Functional Human Blood Vessels Are Permissive Niches for Human Breast Cancer Metastasis', *PLOS ONE*, vol. 8, no. 8, p. e72957, Aug. 2013, doi: 10.1371/journal.pone.0072957.

[55] J. M. Rosenbluth *et al.*, 'Organoid cultures from normal and cancer-prone human breast tissues preserve complex epithelial lineages', *Nat Commun*, vol. 11, no. 1, Art. no. 1, Apr. 2020, doi: 10.1038/s41467-020-15548-7.

[56] A. J. Walsh *et al.*, 'Quantitative optical imaging of primary tumor organoid metabolism predicts drug response in breast cancer', *Cancer Res*, vol. 74, no. 18, pp. 5184–5194, Sep. 2014, doi: 10.1158/0008-5472.CAN-14-0663.

[57] M. T. Kozlowski, C. J. Crook, and H. T. Ku, 'Towards organoid culture without Matrigel', *Commun Biol*, vol. 4, no. 1, Art. no. 1, Dec. 2021, doi: 10.1038/s42003-021-02910-8.

[58] K. Białkowska, P. Komorowski, M. Bryszewska, and K. Miłowska, 'Spheroids as a Type of Three-Dimensional Cell Cultures – Examples of Methods of Preparation and the Most Important Application', *IJMS*, vol. 21, no. 17, p. 6225, Aug. 2020, doi: 10.3390/ijms21176225.

[59] M. Huerta-Reyes and A. Aguilar-Rojas, 'Three-dimensional models to study breast cancer (Review)', *International Journal of Oncology*, vol. 58, no. 3, pp. 331–343, Mar. 2021, doi: 10.3892/ijo.2021.5176.

[60] X. Cui, Y. Hartanto, and H. Zhang, ‘Advances in multicellular spheroids formation’, *Journal of The Royal Society Interface*, vol. 14, no. 127, p. 20160877, Feb. 2017, doi: 10.1098/rsif.2016.0877.

[61] O. Yilmaz and S. Sakarya, ‘Is 'Hanging Drop’ a Useful Method to Form Spheroids of Jimt, Mcf-7, T-47d, Bt-474 That are Breast Cancer Cell Lines’, vol. 07, Jan. 2018, doi: 10.4172/2168-9431.1000170.

[62] L. A. Kunz-Schughart, M. Kreutz, and R. Knuechel, ‘Multicellular spheroids: a three-dimensional in vitro culture system to study tumour biology’, *Int J Exp Pathol*, vol. 79, no. 1, pp. 1–23, Feb. 1998, doi: 10.1046/j.1365-2613.1998.00051.x.

[63] X. Gong *et al.*, ‘Generation of Multicellular Tumor Spheroids with Microwell-Based Agarose Scaffolds for Drug Testing’, *PLoS One*, vol. 10, no. 6, p. e0130348, Jun. 2015, doi: 10.1371/journal.pone.0130348.

[64] S. J. Han, S. Kwon, and K. S. Kim, ‘Challenges of applying multicellular tumor spheroids in preclinical phase’, *Cancer Cell Int*, vol. 21, no. 1, p. 152, Dec. 2021, doi: 10.1186/s12935-021-01853-8.

[65] I. Yakavets, A. Francois, A. Benoit, J.-L. Merlin, L. Bezdetnaya, and G. Vogin, ‘Advanced co-culture 3D breast cancer model for investigation of fibrosis induced by external stimuli: optimization study’, *Sci Rep*, vol. 10, no. 1, p. 21273, Dec. 2020, doi: 10.1038/s41598-020-78087-7.

[66] S. Singh, S. Tran, J. Putman, and H. Tavana, ‘Three-dimensional models of breast cancer–fibroblasts interactions’, *Exp Biol Med (Maywood)*, vol. 245, no. 10, pp. 879–888, May 2020, doi: 10.1177/1535370220917366.

[67] M. Upreti *et al.*, ‘Tumor-Endothelial Cell Three-dimensional Spheroids: New Aspects to Enhance Radiation and Drug Therapeutics’, *Translational Oncology*, vol. 4, no. 6, pp. 365-IN3, Dec. 2011, doi: 10.1593/tlo.11187.

[68] H. Shoval *et al.*, ‘Tumor cells and their crosstalk with endothelial cells in 3D spheroids’, *Sci Rep*, vol. 7, no. 1, p. 10428, Dec. 2017, doi: 10.1038/s41598-017-10699-y.

[69] G. Valcz *et al.*, ‘Extracellular Vesicle-Based Communication May Contribute to the Co-Evolution of Cancer Stem Cells and Cancer-Associated Fibroblasts in Anti-Cancer Therapy’, *Cancers*, vol. 12, no. 8, Art. no. 8, Aug. 2020, doi: 10.3390/cancers12082324.

[70] Y. Mao, E. T. Keller, D. H. Garfield, K. Shen, and J. Wang, ‘Stromal cells in tumor microenvironment and breast cancer’, *Cancer Metastasis Rev*, vol. 32, no. 1, pp. 303–315, Jun. 2013, doi: 10.1007/s10555-012-9415-3.

[71] S. L. Ham *et al.*, ‘Three-dimensional tumor model mimics stromal – breast cancer cells signaling’, *Oncotarget*, vol. 9, no. 1, pp. 249–267, Dec. 2017, doi: 10.18632/oncotarget.22922.

[72] J. Mei *et al.*, 'Development of a model for fibroblast-led collective migration from breast cancer cell spheroids to study radiation effects on invasiveness', *Radiat Oncol*, vol. 16, no. 1, p. 159, Dec. 2021, doi: 10.1186/s13014-021-01883-6.

[73] C. Moccia and K. Haase, 'Engineering Breast Cancer On-chip – Moving Toward Subtype Specific Models', *Frontiers in Bioengineering and Biotechnology*, vol. 9, 2021, Accessed: Apr. 17, 2022. [Online]. Available: https://www.frontiersin.org/article/10.3389/fbioe.2021.694218

[74] P. K. Chaudhuri, M. Ebrahimi Warkiani, T. Jing, K. Kenry, and C. T. Lim, 'Microfluidics for research and applications in oncology', *Analyst*, vol. 141, no. 2, pp. 504–524, 2016, doi: 10.1039/C5AN00382B.

[75] G. S. Fiorini and D. T. Chiu, 'Disposable microfluidic devices: fabrication, function, and application', *BioTechniques*, vol. 38, no. 3, pp. 429–446, Mar. 2005, doi: 10.2144/05383RV02.

[76] Y. Nashimoto *et al.*, 'Vascularized cancer on a chip: The effect of perfusion on growth and drug delivery of tumor spheroid', *Biomaterials*, vol. 229, p. 119547, Jan. 2020, doi: 10.1016/j.biomaterials.2019.119547.

[77] M. Humayun *et al.*, 'Elucidating cancer-vascular paracrine signaling using a human organotypic breast cancer cell extravasation model', *Biomaterials*, vol. 270, p. 120640, Mar. 2021, doi: 10.1016/j.biomaterials.2020.120640.

[78] S. Halldorsson, E. Lucumi, R. Gómez-Sjöberg, and R. M. T. Fleming, 'Advantages and challenges of microfluidic cell culture in polydimethylsiloxane devices', *Biosensors and Bioelectronics*, vol. 63, pp. 218–231, Jan. 2015, doi: 10.1016/j.bios.2014.07.029.

[79] Y. Li and E. Kumacheva, 'Hydrogel microenvironments for cancer spheroid growth and drug screening', *Science Advances*, vol. 4, no. 4, p. eaas8998, Apr. 2018, doi: 10.1126/sciadv.aas8998.

[80] M. Bahram, N. Mohseni, and M. Moghtader, *An Introduction to Hydrogels and Some Recent Applications*. IntechOpen, 2016. doi: 10.5772/64301.

[81] K. M. Tevis, Y. L. Colson, and M. W. Grinstaff, 'Embedded Spheroids as Models of the Cancer Microenvironment', *Adv Biosyst*, vol. 1, no. 10, p. 1700083, Oct. 2017, doi: 10.1002/adbi.201700083.

[82] A. Quarta *et al.*, 'Agarose-collagen I hydrogels: impact of the matrix stiffness on the growth of breast cancer cell lines spheroids and on drug penetration', Preprints, preprint, Mar. 2021. doi: 10.22541/au.161513073.39724919/v1.

[83] M. Plaster, S. Singh, and H. Tavana, 'Fibroblasts Promote Proliferation and Matrix Invasion of Breast Cancer Cells in Co-Culture Models', *Advanced Therapeutics*, vol. 2, no. 11, p. 1900121, 2019, doi: 10.1002/adtp.201900121.

[84] P. Correa de Sampaio *et al.*, 'A Heterogeneous In Vitro Three Dimensional Model of Tumour-Stroma Interactions Regulating Sprouting Angiogenesis', *PLoS One*, vol. 7, no. 2, p. e30753, Feb. 2012, doi: 10.1371/journal.pone.0030753.

[85] X. Wang and C. Liu, 'Fibrin Hydrogels for Endothelialized Liver Tissue Engineering with a Predesigned Vascular Network', *Polymers (Basel)*, vol. 10, no. 10, p. 1048, Sep. 2018, doi: 10.3390/polym10101048.

[86] S. M. Ehsan, K. M. Welch-Reardon, M. L. Waterman, C. C. W. Hughes, and S. C. George, 'A three-dimensional in vitro model of tumor cell intravasation', *Integr Biol (Camb)*, vol. 6, no. 6, pp. 603–610, Jun. 2014, doi: 10.1039/c3ib40170g.

[87] V. M. Weaver *et al.*, 'Reversion of the Malignant Phenotype of Human Breast Cells in Three-Dimensional Culture and In Vivo by Integrin Blocking Antibodies', *J Cell Biol*, vol. 137, no. 1, pp. 231–245, Apr. 1997.

[88] G. Y. Lee, P. A. Kenny, E. H. Lee, and M. J. Bissell, 'Three-dimensional culture models of normal and malignant breast epithelial cells', *Nat Methods*, vol. 4, no. 4, pp. 359–365, Apr. 2007, doi: 10.1038/nmeth1015.

[89] E. A. Aisenbrey and W. L. Murphy, 'Synthetic alternatives to Matrigel', *Nat Rev Mater*, vol. 5, no. 7, pp. 539–551, Jul. 2020, doi: 10.1038/s41578-020-0199-8.

[90] C. Fischbach, H. J. Kong, S. X. Hsiong, M. B. Evangelista, W. Yuen, and D. J. Mooney, 'Cancer cell angiogenic capability is regulated by 3D culture and integrin engagement', *Proceedings of the National Academy of Sciences*, vol. 106, no. 2, pp. 399–404, Jan. 2009, doi: 10.1073/pnas.0808932106.

[91] S. J. Bidarra, P. Oliveira, S. Rocha, D. P. Saraiva, C. Oliveira, and C. C. Barrias, 'A 3D in vitro model to explore the inter-conversion between epithelial and mesenchymal states during EMT and its reversion', *Sci Rep*, vol. 6, p. 27072, Jun. 2016, doi: 10.1038/srep27072.

[92] F. C. Teixeira, S. Chaves, A. L. Torres, C. C. Barrias, and S. J. Bidarra, 'Engineering a Vascularized 3D Hybrid System to Model Tumor-Stroma Interactions in Breast Cancer', *Frontiers in Bioengineering and Biotechnology*, vol. 9, 2021, Accessed: Apr. 28, 2022. [Online]. Available: https://www.frontiersin.org/article/10.3389/fbioe.2021.647031

[93] R. J. Narayan, 'The next generation of biomaterial development', *Philosophical Transactions of the Royal Society A: Mathematical, Physical and Engineering Sciences*, vol. 368, no. 1917, pp. 1831–1837, Apr. 2010, doi: 10.1098/rsta.2010.0001.

[94] L. L. Hench and I. Thompson, 'Twenty-first century challenges for biomaterials', *J R Soc Interface*, vol. 7, no. Suppl 4, pp. S379–S391, Aug. 2010, doi: 10.1098/rsif.2010.0151.focus.

[95] K. Y. Lee and D. J. Mooney, 'Alginate: properties and biomedical applications', *Prog Polym Sci*, vol. 37, no. 1, pp. 106–126, Jan. 2012, doi: 10.1016/j.progpolymsci.2011.06.003.

[96] S. G. Reddy, *Alginates - A Seaweed Product: Its Properties and Applications*. IntechOpen, 2021. doi: 10.5772/intechopen.98831.

[97] L. Cao, W. Lu, A. Mata, K. Nishinari, and Y. Fang, 'Egg-box model-based gelation of alginate and pectin: A review', *Carbohydrate Polymers*, vol. 242, p. 116389, Aug. 2020, doi: 10.1016/j.carbpol.2020.116389.

[98] S. J. Bidarra, C. C. Barrias, K. B. Fonseca, M. A. Barbosa, R. A. Soares, and P. L. Granja, 'Injectable in situ crosslinkable RGD-modified alginate matrix for endothelial cells delivery', *Biomaterials*, vol. 32, no. 31, pp. 7897–7904, Nov. 2011, doi: 10.1016/j.biomaterials.2011.07.013.

[99] L. W. Chan, H. Y. Lee, and P. W. S. Heng, 'Mechanisms of external and internal gelation and their impact on the functions of alginate as a coat and delivery system', *Carbohydrate Polymers*, vol. 63, no. 2, pp. 176–187, Feb. 2006, doi: 10.1016/j.carbpol.2005.07.033.

[100] S. J. Bidarra, C. C. Barrias, and P. L. Granja, 'Injectable alginate hydrogels for cell delivery in tissue engineering', 2014. Accessed: Apr. 30, 2022. [Online]. Available: https://www.sciencedirect.com/science/article/pii/S1742706113006028

[101] L. He, Z. Shang, H. Liu, and Z. Yuan, 'Alginate-Based Platforms for Cancer-Targeted Drug Delivery', *Biomed Res Int*, vol. 2020, p. 1487259, Oct. 2020, doi: 10.1155/2020/1487259.

[102] P. Barros da Silva, M. Coelho, S. J. Bidarra, S. C. Neves, and C. C. Barrias, 'Reshaping in vitro Models of Breast Tissue: Integration of Stromal and Parenchymal Compartments in 3D Printed Hydrogels', *Frontiers in Bioengineering and Biotechnology*, vol. 8, 2020, Accessed: Apr. 30, 2022. [Online]. Available: https://www.frontiersin.org/article/10.3389/fbioe.2020.00494

[103] M. Cavo, M. Caria, I. Pulsoni, F. Beltrame, M. Fato, and S. Scaglione, 'A new cell-laden 3D Alginate-Matrigel hydrogel resembles human breast cancer cell malignant morphology, spread and invasion capability observed "in vivo"', *Sci Rep*, vol. 8, no. 1, Art. no. 1, Mar. 2018, doi: 10.1038/s41598-018-23250-4.

[104] M. V. de Magalhães, 'Bioengineering a 3D Breast Tumor Angiogenesis Model', Faculty of Engineering of University of Porto, Porto, Portugal, 2021.

[105] M. I. Neves, L. Moroni, and C. C. Barrias, 'Modulating Alginate Hydrogels for Improved Biological Performance as Cellular 3D Microenvironments', *Frontiers in Bioengineering and Biotechnology*, vol. 8, 2020, Accessed: Apr. 29, 2022. [Online]. Available: https://www.frontiersin.org/article/10.3389/fbioe.2020.00665

[106] A. L. Torres, S. J. Bidarra, M. T. Pinto, P. C. Aguiar, E. A. Silva, and C. C. Barrias, 'Guiding morphogenesis in cell-instructive microgels for therapeutic angiogenesis', *Biomaterials*, vol. 154, pp. 34–47, Feb. 2018, doi: 10.1016/j.biomaterials.2017.10.051.

[107] A. Peirsman *et al.*, 'MISpheroID: a knowledgebase and transparency tool for minimum information in spheroid identity', *Nat Methods*, vol. 18, no. 11, Art. no. 11, Nov. 2021, doi: 10.1038/s41592-021-01291-4.

[108] Ş. Comşa, A. M. Cîmpean, and M. Raica, 'The Story of MCF-7 Breast Cancer Cell Line: 40 years of Experience in Research', *ANTICANCER RESEARCH*, p. 8, 2015.

[109] S. Raghavan, P. Mehta, E. N. Horst, M. R. Ward, K. R. Rowley, and G. Mehta, 'Comparative analysis of tumor spheroid generation techniques for differential in vitro drug toxicity', *Oncotarget*, vol. 7, no. 13, pp. 16948–16961, Feb. 2016, doi: 10.18632/oncotarget.7659.

[110] L. Pulze *et al.*, 'MCF7 Spheroid Development: New Insight about Spatio/Temporal Arrangements of TNTs, Amyloid Fibrils, Cell Connections, and Cellular Bridges', *Int J Mol Sci*, vol. 21, no. 15, p. 5400, Jul. 2020, doi: 10.3390/ijms21155400.

[111] A. S. Sogomonyan, V. O. Shipunova, V. D. Soloviev, V. I. Larionov, P. A. Kotelnikova, and S. M. Deyev, '3D Models of Cellular Spheroids As a Universal Tool for Studying the Cytotoxic Properties of Anticancer Compounds In Vitro', *Acta Naturae*, vol. 14, no. 1, pp. 92–100, 2022, doi: 10.32607/actanaturae.11603.

[112] G. Gunaydin, S. A. Kesikli, and D. Guc, 'Cancer associated fibroblasts have phenotypic and functional characteristics similar to the fibrocytes that represent a novel MDSC subset', *Oncoimmunology*, vol. 4, no. 9, p. e1034918, May 2015, doi: 10.1080/2162402X.2015.1034918.

[113] Q. Ping *et al.*, 'Cancer-associated fibroblasts: overview, progress, challenges, and directions', *Cancer Gene Ther*, vol. 28, no. 9, Art. no. 9, Sep. 2021, doi: 10.1038/s41417-021-00318-4.

[114] A. Santi, F. G. Kugeratski, and S. Zanivan, 'Cancer Associated Fibroblasts: The Architects of Stroma Remodeling', *PROTEOMICS*, vol. 18, no. 5–6, p. 1700167, 2018, doi: 10.1002/pmic.201700167.

[115] J. Barbazán and D. Matic Vignjevic, 'Cancer associated fibroblasts: is the force the path to the dark side?', *Current Opinion in Cell Biology*, vol. 56, pp. 71–79, Feb. 2019, doi: 10.1016/j.ceb.2018.09.002.

[116] J. Winkler, A. Abisoye-Ogunniyan, K. J. Metcalf, and Z. Werb, 'Concepts of extracellular matrix remodelling in tumour progression and metastasis', *Nat Commun*, vol. 11, no. 1, Art. no. 1, Oct. 2020, doi: 10.1038/s41467-020-18794-x.

[117] M. Bauer, G. Su, C. Casper, R. He, W. Rehrauer, and A. Friedl, 'Heterogeneity of gene expression in stromal fibroblasts of human breast carcinomas and normal breast', *Oncogene*, vol. 29, no. 12, Art. no. 12, Mar. 2010, doi: 10.1038/onc.2009.463.

[118] I. Jang and K. A. Beningo, 'Integrins, CAFs and Mechanical Forces in the Progression of Cancer', *Cancers (Basel)*, vol. 11, no. 5, p. 721, May 2019, doi: 10.3390/cancers11050721.

[119] X. Wang *et al.*, 'Vimentin plays an important role in the promotion of breast cancer cell migration and invasion by leucine aminopeptidase 3', *Cytotechnology*, vol. 72, no. 5, pp. 639–647, Oct. 2020, doi: 10.1007/s10616-020-00402-x.

[120] D. T. O. Carvalho, T. Feijão, M. I. Neves, R. M. P. da Silva, and C. C. Barrias, 'Directed self-assembly of spheroids into modular vascular beds for engineering large tissue constructs', *Biofabrication*, vol. 13, no. 3, p. 035008, Apr. 2021, doi: 10.1088/1758-5090/abc790.

[121] M. Nurmik, P. Ullmann, F. Rodriguez, S. Haan, and E. Letellier, 'In search of definitions: Cancer-associated fibroblasts and their markers', *International Journal of Cancer*, vol. 146, no. 4, pp. 895–905, 2020, doi: 10.1002/ijc.32193.

[122] Z. Wang *et al.*, 'Clinical implications of β-catenin protein expression in breast cancer', *Int J Clin Exp Pathol*, vol. 8, no. 11, pp. 14989–14994, Nov. 2015.

[123] B. Erdogan *et al.*, 'Cancer-associated fibroblasts promote directional cancer cell migration by aligning fibronectin', *J Cell Biol*, vol. 216, no. 11, pp. 3799–3816, Nov. 2017, doi: 10.1083/jcb.201704053.

[124] A. Malakpour-Permlid, I. Buzzi, C. Hegardt, F. Johansson, and S. Oredsson, 'Identification of extracellular matrix proteins secreted by human dermal fibroblasts cultured in 3D electrospun scaffolds', *Sci Rep*, vol. 11, no. 1, Art. no. 1, Mar. 2021, doi: 10.1038/s41598-021-85742-0.

[125] G. Fang, H. Lu, A. Law, D. Gallego-Ortega, D. Jin, and G. Lin, 'Gradient-sized control of tumor spheroids on a single chip', *Lab Chip*, vol. 19, no. 24, pp. 4093–4103, Dec. 2019, doi: 10.1039/C9LC00872A.

[126] M. V. Monteiro, V. M. Gaspar, L. Mendes, I. F. Duarte, and J. F. Mano, 'Stratified 3D Microtumors as Organotypic Testing Platforms for Screening Pancreatic Cancer Therapies', *Small Methods*, vol. 5, no. 5, p. 2001207, 2021, doi: 10.1002/smtd.202001207.

[127] E. Elwakeel and A. Weigert, 'Breast Cancer CAFs: Spectrum of Phenotypes and Promising Targeting Avenues', *Int J Mol Sci*, vol. 22, no. 21, p. 11636, Oct. 2021, doi: 10.3390/ijms222111636.

[128] K. Louault *et al.*, 'Interactions between cancer-associated fibroblasts and tumor cells promote MCL-1 dependency in estrogen receptor-positive breast cancers', *Oncogene*, vol. 38, no. 17, Art. no. 17, Apr. 2019, doi: 10.1038/s41388-018-0635-z.

[129] Y. Attieh *et al.*, 'Cancer-associated fibroblasts lead tumor invasion through integrin-β3–dependent fibronectin assembly', *J Cell Biol*, vol. 216, no. 11, pp. 3509–3520, Nov. 2017, doi: 10.1083/jcb.201702033.

[130] F. Calvo *et al.*, 'Mechano-transduction and YAP-dependent matrix remodelling is required for the generation and maintenance of cancer associated fibroblasts', *Nat Cell Biol*, vol. 15, no. 6, p. 10.1038/ncb2756, Jun. 2013, doi: 10.1038/ncb2756.

[131] K. Froehlich *et al.*, 'Generation of Multicellular Breast Cancer Tumor Spheroids: Comparison of Different Protocols', *J Mammary Gland Biol Neoplasia*, vol. 21, no. 3–4, pp. 89–98, Dec. 2016, doi: 10.1007/s10911-016-9359-2.

[132] X. Jiang, C. Wang, S. Fitch, and F. Yang, 'Targeting Tumor Hypoxia Using Nanoparticle-engineered CXCR4-overexpressing Adipose-derived Stem Cells', *Theranostics*, vol. 8, no. 5, pp. 1350–1360, 2018, doi: 10.7150/thno.22736.

[133] B. Zhao *et al.*, 'Hypoxia drives the transition of human dermal fibroblasts to a myofibroblast-like phenotype via the TGF-β1/Smad3 pathway Corrigendum in /10.3892/ijmm.2019.4403', *International Journal of Molecular Medicine*, vol. 39, no. 1, pp. 153–159, Jan. 2017, doi: 10.3892/ijmm.2016.2816.

[134] S. Fuchs, E. Dohle, M. Kolbe, and C. J. Kirkpatrick, 'Outgrowth Endothelial Cells: Sources, Characteristics and Potential Applications in Tissue Engineering and Regenerative Medicine', in *Bioreactor Systems for Tissue Engineering II: Strategies for the Expansion and Directed Differentiation of Stem Cells*, C. Kasper, M. van Griensven, and R. Pörtner, Eds. Berlin, Heidelberg: Springer, 2010, pp. 201–217. doi: 10.1007/10_2009_65.

[135] T. Feijão *et al.*, 'Engineering injectable vascularized tissues from the bottom-up: Dynamics of in-gel extra-spheroid dermal tissue assembly', *Biomaterials*, vol. 279, p. 121222, Dec. 2021, doi: 10.1016/j.biomaterials.2021.121222.

[136] A. L. Torres *et al.*, 'Microvascular engineering: Dynamic changes in microgel-entrapped vascular cells correlates with higher vasculogenic/angiogenic potential', *Biomaterials*, vol. 228, p. 119554, Jan. 2020, doi: 10.1016/j.biomaterials.2019.119554.

[137] V. Vanchinathan, N. Mizramani, R. Kantipudi, E. J. Schwartz, and U. N. Sundram, 'The Vascular Marker CD31 Also Highlights Histiocytes and Histiocyte-Like Cells Within Cutaneous Tumors', *American Journal of Clinical Pathology*, vol. 143, no. 2, pp. 177–185, Feb. 2015, doi: 10.1309/AJCPRHM8CZH5EMFD.

[138] B. Horvath *et al.*, 'Measurement of von Willebrand factor as the marker of endothelial dysfunction in vascular diseases', *Exp Clin Cardiol*, vol. 9, no. 1, pp. 31–34, 2004.

[139] T. Gonzalez-Fernandez, A. J. Tenorio, A. M. Saiz Jr, and J. K. Leach, 'Engineered Cell-Secreted Extracellular Matrix Modulates Cell Spheroid Mechanosensing and Amplifies Their Response to Inductive Cues for the Formation of Mineralized Tissues', *Advanced Healthcare Materials*, vol. 11, no. 10, p. 2102337, 2022, doi: 10.1002/adhm.202102337.

[140] E. Bauman, T. Feijão, D. T. O. Carvalho, P. L. Granja, and C. C. Barrias, 'Xeno-free pre-vascularized spheroids for therapeutic applications', *Sci Rep*, vol. 8, no. 1, Art. no. 1, Jan. 2018, doi: 10.1038/s41598-017-18431-6.

[141] A. Golunova *et al.*, 'Direct and Indirect Biomimetic Peptide Modification of Alginate: Efficiency, Side Reactions, and Cell Response', *Int J Mol Sci*, vol. 22, no. 11, p. 5731, May 2021, doi: 10.3390/ijms22115731.

[142] M. D'Este, D. Eglin, and M. Alini, 'A systematic analysis of DMTMM vs EDC/NHS for ligation of amines to hyaluronan in water', *Carbohydr Polym*, vol. 108, pp. 239–246, Aug. 2014, doi: 10.1016/j.carbpol.2014.02.070.

[143] L. E. Jansen, L. J. Negrón-Piñeiro, S. Galarza, and S. R. Peyton, 'Control of Thiol-Maleimide Reaction Kinetics in PEG Hydrogel Networks', *Acta Biomater*, vol. 70, pp. 120–128, Apr. 2018, doi: 10.1016/j.actbio.2018.01.043.

[144] S. M. Hashemnejad and S. Kundu, 'Rheological properties and failure of alginate hydrogels with ionic and covalent crosslinks', *Soft Matter*, vol. 15, no. 39, pp. 7852–7862, 2019, doi: 10.1039/C9SM01039D.

[145] R. F. Pereira, C. C. Barrias, P. J. Bártolo, and P. L. Granja, 'Cell-instructive pectin hydrogels crosslinked via thiol-norbornene photo-click chemistry for skin tissue engineering', *Acta Biomater*, vol. 66, pp. 282–293, Jan. 2018, doi: 10.1016/j.actbio.2017.11.016.

[146] S. Ishihara and H. Haga, 'Matrix Stiffness Contributes to Cancer Progression by Regulating Transcription Factors', *Cancers*, vol. 14, no. 4, Art. no. 4, Jan. 2022, doi: 10.3390/cancers14041049.